DEEPWATER INTERNAL WAVE STUDY AND APPLICATIION

A Thesis

by

LEI JIANG

Submitted to the Office of Graduate and Professional Studies of
Texas A&M University
in partial fulfillment of the requirements for the degree of

MASTER OF SCIENCE

Chair of Committee,	Moo-Hyun Kim
Committee Members,	Alejandro H. Orsi
	Robert E. Randall
Head of Department,	Robin Authenrieth

December 2013

Major Subject: Ocean Engineering

ABSTRACT

Internal waves near the ocean surface have been observed in many parts of the world including the Andaman Sea, Sulu Sea and South China Sea. The factors that cause and propagate these large-amplitude waves include bathymetry, density stratification and ocean currents. Although their effects on floating drilling platforms and their riser systems have not been extensively studied, in the past these waves have seriously disrupted offshore exploration and drilling operations. In particular, a drill pipe was ripped from the Blow-Out Preventer (BOP) and lost during drilling operations in the Andaman Sea. Drilling riser damages were also reported from the South China Sea and other places.

The motivations of this study were to find a valid numerical model conforming to the physics of internal waves and to study the effects on offshore drilling semisubmersibles, different types of offshore hull forms and riser systems, including the large diameter cold water pipe of floating Ocean Thermal Energy Conversion (OTEC) systems.

The influence of internal waves on offshore systems was studied through nonlinear fully coupled time-domain analysis. The numerical model was implemented in a coupled analysis program where the hull, moorings and riser were considered an integrated system. The program HARP was modified and then utilized to study the effects of the internal wave on the platform global motions and riser system integrity. The study could be useful as future guidance for offshore exploration and operations in areas where the internal wave phenomenon is prominent.

ACKNOWLEDGEMENTS

I would like to thank my committee chair, Dr. Kim, and my committee members, Dr. Orsi and Dr. Randall, for their guidance and support throughout the course of this research.

Thanks also go to my friends and colleagues and the department faculty and staff for making my time at Texas A&M University a great experience. I also want to extend my gratitude to Dr. Shan Shi, Dr. John Halkyard, and Nishu V Kurup, who worked with me in the study.

Finally, thanks to my mother and father for their encouragement and to my family for their patience and love.

NOMENCLATURE

OTEC	Ocean Thermal Energy Conversion
CWP	Cold Water Pipe
FEA	Finite Element Analysis
CPC	Chain-Polyester-Chain
VIV	Vortex Induced Vibrations

TABLE OF CONTENTS

Page

LIST OF FIGURES

Page

LIST OF TABLES

Page

1. INTRODUCTION AND LITERATURE REVIEW

1.1. Introduction

In 1970's the internal wave still a huge but little know subsurface disturbance. We now know that internal waves occur quite frequently in many oceans of the world. As shown in Figure 1.1 and Figure 1.2 below, internal waves occur in subsurface layers of ocean water that differ in temperature and salinity.

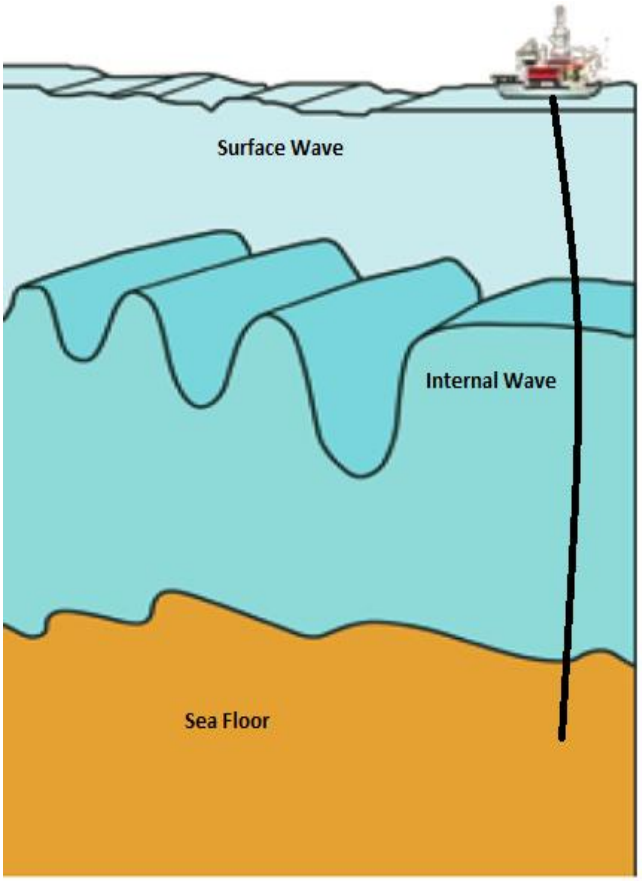

Figure 1.1 Internal wave sketch from 'Waves beneath the sea' by Lawrence Locke

Figure below shows the path of water movement within an internal wave resulting in the surface rips presented in paper ‘Waves beneath the sea’ by Lawrence Locke. A peculiarity of most observed internal waves travel upside down, crests pointing to the seafloor.

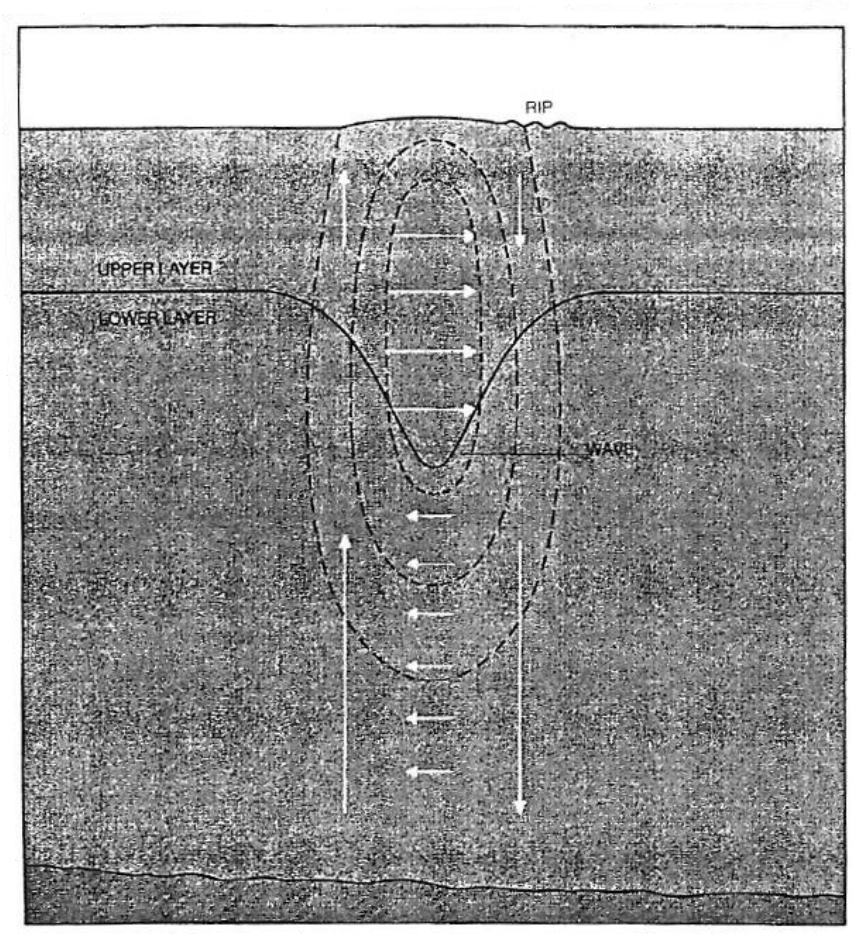

Figure 1.2 Internal wave water particle movement

The pertinent differential equation that captures the physics of internal wave is the Korteweg-de Vries (KdV) equation which has a general solution involving Jacobian elliptical functions. The solution of the Taylor Goldstein equation captures the effects of

the pycnocline. Internal wave packets with decayed oscillations as observed from satellite pictures are specifically modeled. The nonlinear internal waves are characterized by wave amplitudes that can exceed 50 ms and the present of shearing currents near the layer of pycnocline. The offshore systems such as drilling semisubmersibles and other floating platforms are exposed to these current shears and the associated movements of large volumes of water.

Ocean Thermal Energy Conversion (OTEC) systems utilize the temperature difference between the surface water and deep ocean water to generate electrical energy. Floating OTEC system usually consist a up to 1000m long large diameter cold water pipe (CWP). In addition to ocean surface waves, wind and current, the presence of strong internal waves may become a concern in floating OTEC system design. It is important to study the dependence of the CWP hydrodynamic drag on relative velocity of the flow around the pipe, the effect of drag amplification due to vortex induced vibrations and the influence of internal waves on the floating semi and the cold water pipe integrated OTEC system.

The effect of internal waves on offshore systems is studied through nonlinear fully coupled time domain analysis. The numerical model is implemented in a coupled analysis program where the hull, moorings and riser are considered as an integrated system. The program is then utilized to study the effects of the internal wave on the platform global motions and riser system integrity. The study could be useful for future guidance on offshore exploration and operations in areas where the internal wave phenomenon is prominent.

1.2. Literature Review

In 1838 John Scott Russell reported isolated surface solitary waves in a shallow unstratified Scottish canal. Recent satellite observations of internal wave in South China Sea are shown in Figure 1.3 and Figure 1.4 below:

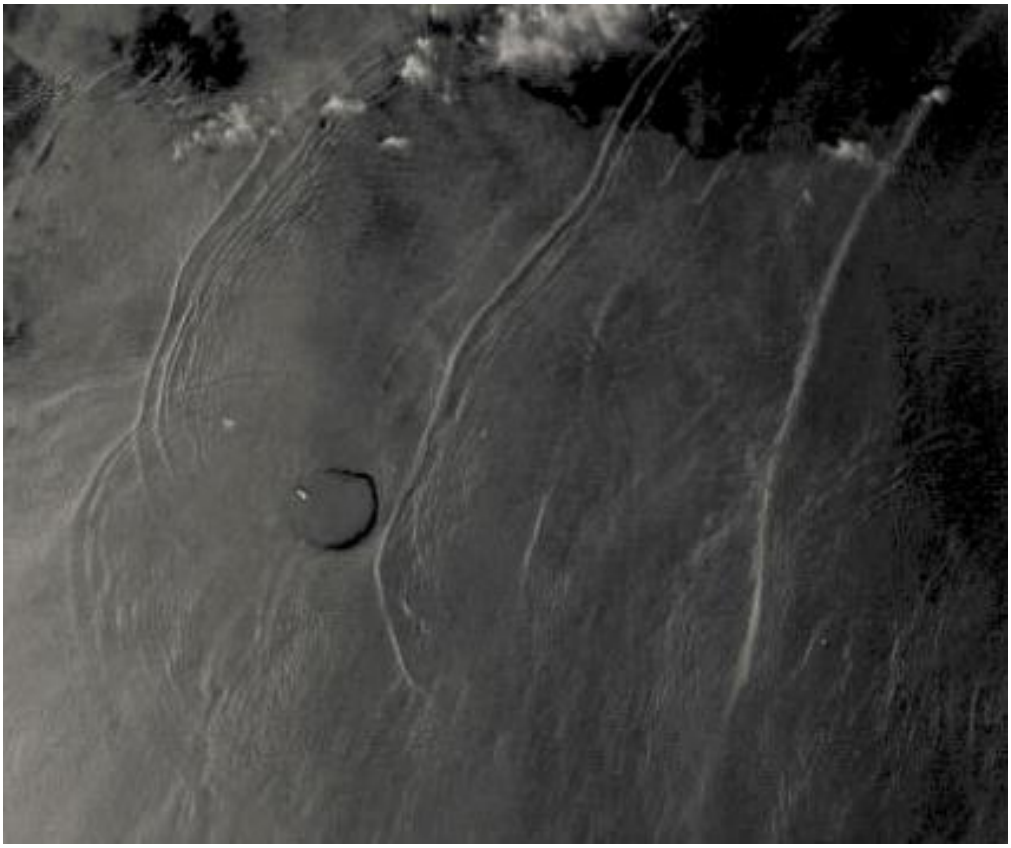

Figure 1.3 Satellite observations of internal wave in South China (1)

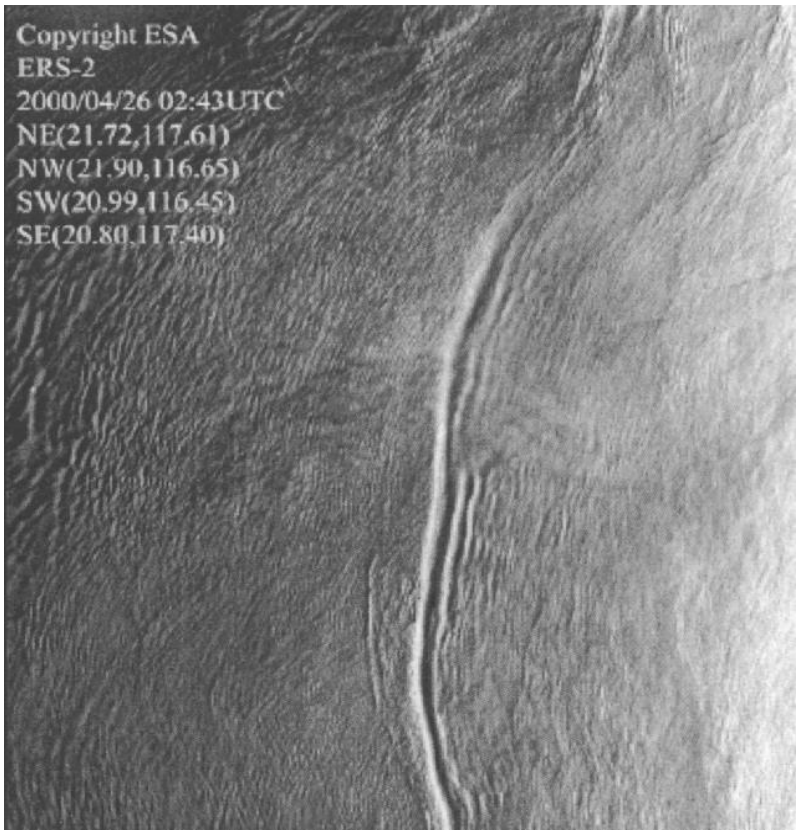

Figure 1.4 Satellite observations of internal wave in South China (2)

Some valuable observations are summarized in below:

- Internal waves come with groups
- At each group, the wave period is about 5 to 20 minutes
- The maximum internal wave speed observed is 2.9 m/sec.
- The surface wave height could be as large as 170m
- The internal wave depth could be up to -2000m
- Internal waves may come with many groups

The theoretical description of the waves was presented by Korteweg and de Vries (Korteweg and de Vries 1895) in 1895. This theoretical formulation can also be used for describing internal solitary waves in the ocean. Surface manifestations of these waves have long been known to sailors as “deadwater phenomenon” or “tidal rips”. These waves can be weakly nonlinear or highly nonlinear in nature. It should be noted that this phenomenon is also ubiquitous to the atmosphere where it manifests in the form of lee waves. Internal waves in oceans have been extensively studied and there is diverse literature on the theoretical and experimental aspects of this phenomenon (Duda and Farmer 1999; Halpern 1971; Ostrovsky and Stepanyants 1989). The effect of internal waves on deep water drilling vessels has also been studied and it was found that increase in mooring line tensions, drill pipe damage, vessel offset and change in heading had occurred under the influence of internal waves (Goff et al. ; Osbourne et al.). The following sections details an internal wave model due to Apel (2003), the numerical solution of the model in a coupled analysis framework and the effects of the model on a drilling semisubmersible.

1.2.1. Canonical Description of Internal Waves

The physics of the internal wave is essentially a counterbalance between nonlinear and dispersive effects (Ablowitz and Segur 1981). The dispersive effects arise due to the differences in velocities of the different Fourier components of a simple wave. While the nonlinearity increases the velocity of such a wave towards a shock like condition the built up energy is dissipated through dispersive effects resulting in a

soliton or solitary wave. Internal waves have three different phases: generation, propagation and dissipation.

Generation

Although the generation phase is the least studied of the three, primarily due to the complexity, several papers in literature address this issue (Bains 1995; Hibiya 1988). The primary cause for this phase are the tidal cycles although ocean currents have also been found to be a contributing factor. It has been observed that the tidal flows over continental shelf breaks or sills are a source of energy for the formation of internal waves. The generation is principally due to the formation of a pycnocline on a side of the shelf break or sill. One theory of internal wave generation states that a sharp plunge in the pycnocline leads to the formation of a lee wave. Observations from echo sounders and CTD have lent credence to this theory (Armi and Farmer 1988). Alternative theories involving shear flow instabilities with bathymetric effects have also been proposed (Farmer and Armi 1999). Due to the strong tidal influence these waves are usually created in semi-diurnal cycles.

Propagation

The propagation phase is characterized by the addition of further oscillations at the rate of one per buoyancy cycle. This is the phase that is primarily considered in this paper. While solitons with a single oscillation has been observed solitary trains could have more than a dozen oscillations. It is also seen that the amplitude, phase speed and wavelength decreases from the front of the train to the trailing edge.

Dissipation

The dissipative phase usually depends on the generating topography. Internal waves due to sills are virtually free of bottom interaction effects with the ocean and thus propagate for longer periods of time. Shelf break induced waves are highly affected by the interaction with the bottom topography. This causes the amplitude and velocity of such waves to reduce due to the dissipating effects of the ocean floor and the decreasing pycnocline depth.

The analytical model of internal wave are obtained from Apel (2003) and solution method are presented will be provided in the next chapter.

2. INTERNAL WAVE ANALYTICAL MODEL FOR COUPLED ANALYSIS

Although as mentioned before, internal waves have a certain structure due to the physics, in reality a complete comprehensive description is quite complicated. A full descriptive picture will involve solving the full Navier-Stokes equations. However considering the large spatial scale of the phenomenon this approach is often time consuming and computationally intensive. Thus analytical models are often used for the study of the phenomenon. It is seen that the term in the Navier Stokes equation responsible for the internal wave is the buoyancy term proportional to the vertical rate of change of density. Thus the Boussinesq approximation, which assumes that small density variations can the neglected in all terms except the buoyancy terms, can be applied to simplify the equations. In the following section the origin is taken at the at the sea surface, x is the horizontal distance from the source while z is the vertical distance from the sea level. The equations are derived in 2D but can be extended to 3D by a simple rotation of coordinate system.

2.1. Assumptions in Analytical Formulation

Since the purpose of this paper is to examine the generic effects of internal waves on offshore floating systems, the following approximations are adopted in formulating the theoretical model. The two dimensional quadratic Korteweg-de Vries equation for weakly nonlinear waves is adopted in the study. The ocean is assumed to consist of two layers. The wavelength is long when compared to the upper water depth.

The second order KdV theory also assumes that the ratio of the amplitude to the upper layer depth is small. If the terms are of comparable magnitude a higher order theory like the cubic KdV will be necessary although past laboratory results (Ko et al. 2008; Vandiver ; Varley et al.) show that the effects of such a theory on changing the velocities is insignificant. The quadratic KdV equation thus captures most of the characteristics of internal waves. However if finite depth or deep water assumptions hold true the pertinent physics is captured by other formulations (Barr and Johnson ; Paulling). Several studies where the above assumptions are relaxed are available in literature (Chou et al. ; Paulling 1980; Sarpkaya 2004) and while the effects of these theories on offshore structures will be interesting, for reasons of brevity this is deferred to later work.

2.2. Korteweg-de Vries Equation

It is seen that with suitable simplifications and approximations and rescaling the Boussinesq approximation can lead to the two dimensional quadratic Korteweg-de Vries equation (Ablowitz and Segur 1981; Korteweg and de Vries 1895).

$$\frac{\partial \eta}{\partial t} + c_0 \frac{\partial \eta}{\partial x} + c_0 \gamma \frac{\partial^3 \eta}{\partial x^3} + \alpha \eta c_0 \frac{\partial \eta}{\partial x} = 0 \qquad (2.1)$$

where η is the amplitude of the internal wave, c0 is the long wavelength phase speed and γ and α are environmental parameters describing the dispersion and nonlinearity respectively.

The KdV equation is characterized by the existence of multiple solutions.

2.2.1. Hyperbolic Secant Profile

The trivial solution is in the form of the following hyperbolic secant equation (Korteweg and de Vries 1895).

$$\eta(x,t) = 2\eta_0 sech^2\left\{\frac{x-Vt}{f(\eta,\alpha,\gamma)}\right\} \tag{2.2}$$

where V is the nonlinear phase speed. This is a single hump profile and while is interesting from the theoretical point of view does not capture solitary wave trains with multiple oscillations.

2.2.2. Cniodal Profile

A second solution in the form of Jacobi elliptic functions was derived by Korteweg and de Vries (Korteweg and de Vries 1895). These functions arise from inversion of elliptic integral of the first kind. The equation is a periodic solution of the form

$$\eta(x,t) = 2\eta_0 cn_s^2\left\{\frac{1}{2}k_0(x-Vt)\right\} \tag{2.3}$$

where k0 is a wave number and s is known as the elliptic modulus and varies from 0 to 1. A modification of equation (2.3) was utilized by Apel and Gonzalves (1983) to describe the internal wave physics. However it is seen that the model doe not fully replicate the characteristics of internal waves seen in the ocean, unless a Fourier analysis involving theta functions and Fourier-like integrals are used (Osborne 1995).

2.2.3. Dnoidal Profile

It was in the context of plasma physics that a new solution of the KdV equation was obtained (Gurevich and Pitaevskii 1973; Gurevich and Pitaevskii 1973). This

solution termed the dnoidal model was utilized by Apel (2003) to investigate the propagation of internal waves in the ocean. The authors have utilized this model in the current paper for our investigations and the notations in (Apel 2003; Gurevich and Pitaevskii 1973; Gurevich and Pitaevskii 1973) are kept for consistency. The reader is referred to (Gurevich and Pitaevskii 1973; Gurevich and Pitaevskii 1973) for the derivation of the solution by asymptotic methods. The dnoidal internal wave profile is of the form

$$\eta(x,t) = 2\eta_0 \left\{ dn_s^2 \left[\frac{1}{2} k_0 (x - Vt) \right] - 1 + s^2 \right\} \tag{2.4}$$

where s is the elliptic modulus and varies from 0 to 1. Using the properties of elliptic functions the equation can be rewritten as

$$\eta(x,t) = 2s^2\eta_0 \left\{ cn_s^2 \left[\frac{1}{2} k_0 (x - Vt) \right] \right\} \tag{2.5}$$

The parameters k0 and V are derived in terms of the KdV environment variables as follows

$$k_0 = 2\sqrt{\left(\frac{\alpha\eta_0}{6\gamma}\right)} \tag{2.6}$$

$$V = c_0 \left(1 + \frac{1+s^2}{3} \alpha\eta_0\right) \tag{2.7}$$

The variation of the elliptic parameter s was originally derived in terms of the space time ratio τ where

$$\tau = \frac{x - c_0 t}{\alpha\eta_0 c_0 t} \tag{2.8}$$

As τ varies from -1 to 2/3, s varies from 0 to 1. The original solution in terms of complete elliptic integrals is seen to be analytically noninvertible. However a simpler

formulation in terms of the error function can be utilized as long as the bounds and monotonicity of the elliptic modulus and space time ratio are kept.

$$s^2 = \frac{erf[\beta(\tau-\varphi)]+1}{2} \tag{2.9}$$

where β and φ are parameters that govern the distribution of wavelengths and number of oscillations over the wave packet under consideration. These values are obtained from observations of internal waves.

The wave number and time period are continuous functions of the elliptic modulus s and thus vary along the wave packet unlike that of a regular surface wave. These are found to be

$$k = \frac{\pi k_0}{2K(s)} \tag{2.10}$$

$$T = \frac{4K(s)}{k_0 V} \tag{2.11}$$

where K(s) is the complete elliptic integral of the first kind.

It is seen that the trailing edge of the internal wave observed in the ocean recovers to the equilibrium pycnocline. This property has to be captured via a recovery function given as

$$I(x,t) = 1 + tanh\left[\frac{2A(x-Vt-\chi)}{x_a}\right] \tag{2.12}$$

where A, χ and xa are parameters that control the shape of the recovery function. The recovery function can also capture the declining amplitude of the solitary train from the front to the trailing edge.

The effect of the pycnocline on the internal wave is captured by the well-known Taylor Goldstein equation.

$$\frac{d^2W(z)}{dz^2} + \left(\frac{N^2}{(U-c)^2} - \frac{U_{zz}}{(U-c)} - k^2\right)W(z) = 0 \tag{2.13}$$

where N is the buoyancy frequency given by

$$N(z) = \sqrt{\frac{-g}{\rho_0}\frac{d\rho}{dz}} \tag{2.14}$$

ρ_0 is the nominal density of the ocean, U is the background current velocity while c is the phase speed. As $k \to 0$, $c \to c_0$. The solution to this equation are in terms of normalized Eigen functions W(z) which form the vertical structure function of the wave profile. Rigid boundary conditions are applied to the top and bottom and the equation solved numerically. Shooting methods are commonly used to obtain the Eigen solution (Newsome and Banta 2003). However a matrix method is used here which guarantees that all the relevant modes will be found within the limits of resolution. It must be noted that in order for the shear flow to be stable the Richardson number must be above ¼.

Procedure of solving Taylor-Goldstein equation is given below:

Let $-\omega_n / ki = c$， $i = \sqrt{-1}$， Equation（2.13）becomes:

$$\begin{aligned} \frac{d^2W_n(z)}{dz^2} - k^2W_n(z) &= \frac{U_{zz}W_n(z)}{\left(U + \frac{\omega_n}{ik}\right)} - \frac{N^2(z)W_n(z)}{\left(U + \frac{\omega_n}{ik}\right)^2} \\ &= \frac{ikU_{zz}W_n(z)}{(\omega_n + ikU)} + \frac{k^2N^2(z)W_n(z)}{(\omega_n + ikU)^2} \end{aligned} \tag{2.15}$$

Further simplification of above gives，

$$(\omega_n + ikU)\left(\frac{d^2}{dz^2} - k^2\right)W_n(z) = ikU_{zz}W_n(z) + \frac{k^2N^2(z)W_n(z)}{(\omega_n + ikU)} \tag{2.16}$$

Separate $W_n(z)$ and ω_n from the above equation, get

$$b_n(z) = \frac{-N^2 W_n(z)}{\omega_n + ikU} \tag{2.17}$$

$$\omega_n b_n(z) = -N^2 W_n(z) - ikU b_n(z) \tag{2.18}$$

Combine (2.16) and (2.17) obtain

$$\omega_n \nabla^2 W_n(z) = -ikU\nabla^2 W_n(z) + ikU_{zz} W_n(z) - k^2 b_n(z) \tag{2.19}$$

where， $\nabla^2 = \frac{d^2}{dz^2} - k^2$ Rewrite (2.18) and (2.19) we can get，

$$\begin{aligned} \omega_n \nabla^2 W_n(z) &= \left(-ikU\nabla^2 + ikU_{zz}\right) W_n(z) - k^2 b_n(z) \\ \omega_n \; b(z) \quad &= \qquad -N^2 W_n(z) \qquad\quad -ikU b_n(z) \end{aligned} \tag{2.20}$$

In matrix form, it is，

$$\begin{bmatrix} \nabla^2 & 0 \\ 0 & 1 \end{bmatrix} \begin{Bmatrix} W_n \\ b_n \end{Bmatrix} = \frac{1}{\omega_n} \begin{bmatrix} -ikU\nabla^2 & -k^2 \\ -N^2 & -ikU \end{bmatrix} \begin{Bmatrix} W_n \\ b_n \end{Bmatrix} \tag{2.21}$$

This is a $2N \times 2N$ matrix equation, its Eigen value ω_n can be solved as below:

$$W_n = \begin{Bmatrix} W_1 \\ \vdots \\ W_N \end{Bmatrix}, \quad b_n = \begin{Bmatrix} b_1 \\ \vdots \\ b_N \end{Bmatrix} \tag{2.22}$$

For example a two layer model， the upper layer height $h_1 = 200m$， the lower layer height $h_2 = 1019.2m$, the structural function $W(z)$ can be solved as shown in Figure 2.1 below:

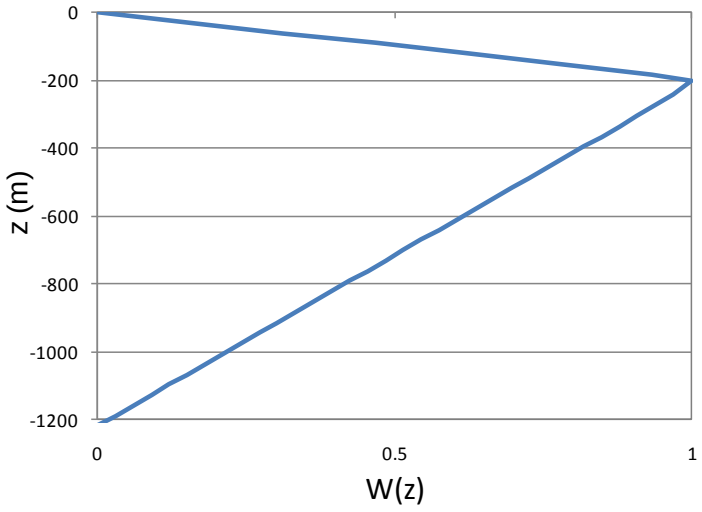

Figure 2.1 Solution of the structural function $W(z)$

The KdV environmental parameters can be obtained by coupling the Taylor Goldstein equation with the equations from the Boussinesq approximation. The expressions for a continuously stratified fluid are obtained in (Liu and Benny 1981). For the special case of a two layered fluid the following expressions are obtained.

$$c = \sqrt{\left[\frac{g(\rho_2-\rho_1)h_1h_2}{\rho_2h_1+\rho_1h_2}\right]} \tag{2.23}$$

$$\alpha = \frac{3c(\rho_2h_1^2-\rho_1h_2^2)}{2h_1h_2(\rho_2h_1+\rho_1h_2)} \tag{2.24}$$

$$\gamma = \frac{ch_1h_2(\rho_1h_1+\rho_2h_2)}{6(\rho_2h_1+\rho_1h_2)} \tag{2.25}$$

where h_1 and ρ_1 are the thickness and density of the upper layer while h_2 and ρ_2 are the thickness and density of the lower layer. In the analysis that follows we assume the ocean to be 2 layered for simplicity.

The final model with all the functions and components mentioned in the above section is presented below

$$\eta(x,z,t) = \eta_0 W(z) I(x,t) \left\{ 2dn_s^2 \left[\frac{1}{2} k_0 (x - Vt) \right] - 1 + s^2 \right\} \qquad (2.26)$$

The function presented above is for the first mode alone. The generalized form will have the sum of all the components due to the different modes. The first mode is considered in this paper as it is the most prevalent and has the highest velocities associated among all the modes. The velocities and accelerations can be obtained by utilizing the continuity equation and the nonlinear kinematic boundary condition (Apel 2003). The model is programmed in Fortran 90 and implemented in coupled analysis program HARP.

The fundamental theory background of coupled analysis and the program HARP are described in the next chapter.

3. DYNAMICS OF THE FLOATING SYSTEMS

In this chapter, the wave loads and dynamic responses of floating structures are discussed. First, linear and second-order wave theories are reviewed in the consideration of the free surface boundary value problem, and then the boundary element method is discussed as one of the solution schemes for the free surface boundary value problem, and Morison's equation and the wave drift damping are considered. Finally, the dynamic motion analysis of floating structures is described.

3.1. Formulation of Surface Wave

3.1.1. Boundary Value Problem (BVP) of Surface Wave

The fluid in the region surrounding the free surface boundary can be expressed as a boundary value problem in the domain. The surface wave theory is derived from the solution of the BVP with the free surface. The fluid motion can be expressed by the Laplace equation of a velocity potential with the assumption of irrotational motion and an incompressible fluid.

$$\nabla u = 0 \tag{3.1}$$

or

$$\nabla^2 \Phi = \frac{\partial^2 \Phi}{\partial x^2} + \frac{\partial^2 \Phi}{\partial y^2} + \frac{\partial^2 \Phi}{\partial z^2} = 0 \tag{3.2}$$

where u is the velocity in x, y or z direction of fluid, so it becomes $\frac{\partial \Phi}{\partial x}\mathrm{i} + \frac{\partial \Phi}{\partial y}\mathrm{j} + \frac{\partial \Phi}{\partial z}\mathrm{k}$.

ϕ is the velocity potential. In order to solve the equation (3.2), the boundary condition should be considered, specifically. The bottom boundary condition is to be considered.

In addition, there are two free surface conditions, which are the dynamic free surface condition and the kinematic free surface condition. The bottom boundary condition is given by the condition that the sea bed is impermeable:

$$\frac{\partial \Phi}{\partial z} = 0 \qquad \text{at} \quad z = -d \tag{3.3}$$

where d is the water depth. The kinematic condition is to represent that the fluid particle on the free surface at any instance retains at one position of the free surface. The equation of the kinematic free surface condition can be given by:

$$\frac{\partial \eta}{\partial t} + u\frac{\partial \eta}{\partial x} + v\frac{\partial \eta}{\partial y} - \frac{\partial \Phi}{\partial z} = 0 \quad \text{at} \quad z = -\eta \tag{3.4}$$

where $\eta(x, y, t)$ is the displacement on the plane of the free surface to be varied in space and time. The dynamic free surface condition defines that the pressure on the free surface is constant as the equal value to the atmospheric pressure and normally the atmospheric pressure is assumed to be zero. Thus, the condition can be described as follows:

$$\frac{\partial \Phi}{\partial t} + \frac{1}{2}(\nabla\Phi \cdot \nabla\Phi) + gz = 0 \quad \text{at} \quad z = -\eta \tag{3.5}$$

where g is the gravitational acceleration. The most popular approach to solve the equation (3.1) is known as the perturbation method under the assumption that the wave amplitude is very small, which can give the approximated solution to satisfy partially the free surface boundary conditions. In the method, the wave elevation (wave particle displacement) and the velocity potential are to be taken as the power series forms a very small non-dimensional perturbation parameter. The linear wave and the second order or

higher order wave can be derived from the perturbation formula of the wave equation, to be represented by the wave elevation and the velocity potential in terms of the perturbation parameter.

3.1.2. Wave Theory

The perturbation formulation of the BVP with the first- and second-order parameters can give the first-order solution and the second-order solution. The first-order solution leads the linear wave theory and the second-order solution leads the second order wave theory. The velocity potential is represented by the summation of all perturbation terms and the wave elevation by summation of the perturbative wave elevations. Finally, the total velocity potential and the wave elevation are written in the following forms:

$$\Phi = \sum \varepsilon^{(n)} \Phi^{(n)} \tag{3.6}$$

$$\eta = \sum \varepsilon^{(n)} \eta^{(n)} \tag{3.7}$$

The linear wave equations are obtained by solving the perturbation formulation formed with the velocity potential and that with the wave elevation are obtained by:

The first-order potential:

$$\Phi^{(1)} = \mathrm{Re}\left[\frac{-igA}{\omega} \frac{\cosh k(z+d)}{\cosh kd} e^{i(kx\cos\theta + ky\sin\theta - \omega t)} \right] \tag{3.8}$$

The first-order wave elevation:

$$\eta^{(1)} = A\cos(kx\cos\theta + ky\sin\theta - \omega t) \tag{3.9}$$

where k is the wave number expressed by $\frac{2\pi}{L}$ when L is the wave length, ω is the wave frequency, A is the wave amplitude, and θ is the incident wave angle. The second-order potential and the second-order wave elevation are obtained by solving the perturbation formulations formed with the second-order potential and the second-order wave elevation are obtained as follows:

The second-order potential:

$$\Phi^{(2)} = \mathrm{Re}\left[\frac{3}{8}\omega A^2 \frac{\cosh 2k(z+d)}{\sinh^4 kd} e^{i(2kx\cos\theta + 2ky\sin\theta - 2\omega t)}\right] \tag{3.10}$$

The second-order wave elevation:

$$\eta^{(2)} = A^2 k \frac{\cosh kd}{\sinh^3 kd}(2+\cosh 2kd)\cos(2kx\cos\theta + 2ky\sin\theta - 2\omega t) \tag{3.11}$$

In the real sea, the wave is irregular and random. A fully developed wave is normally modeled in terms of energy spectra combined with ensembles of wave trains generated by random phases. Well-known spectra in common usage, such as the Pierson- Moskowitz and the JONSWAP spectra, are established. The time series for a given input amplitude spectrum $S(\omega)$ is obtained by combining a reasonably large number N of linear wave components with random phases:

$$\eta(x,y,t) = \sum_{i=1}^{N} A_i \cos(k_i x\cos\theta + k_i y\sin\theta - \omega_i t + \varepsilon_i) = \mathrm{Re}\left[\sum_{i=1}^{N} A_i e^{i(k_i x\cos\theta + k_i y\sin\theta - \omega_i t + \varepsilon_i)}\right] \tag{3.12}$$

where $A_i = \sqrt{2S(\omega_i)\Delta\omega}$ is the wave amplitude of the i-th wave, $\Delta\omega$ is the interval of wave frequency, and ε_i is the random phase angle. To avoid the increase of wave

components and to increase the computational efficiency for a long time simulation, the following modified formula is used:

$$\eta(x,y,t) = \mathrm{Re}\left[\sum_{j=1}^{N} A_j e^{i(k_j x\cos\theta + k_j y\sin\theta - \omega_j' t + \varepsilon_j)}\right] \tag{3.13}$$

where $\omega_j' = \omega_j + \delta\omega_j$ and $\delta\omega_j$ is a random perturbation number uniformly determined between $-\frac{\Delta\omega}{2}$ and $\frac{\Delta\omega}{2}$. The total potential and the wave elevation are given by adding every solution of each order equation, including the diffraction and the radiation.

3.1.3. Diffraction and Radiation Theory

The total velocity potential is decomposed into the incident potential Φ_I, the diffraction potential Φ_D, and the radiation potential Φ_R. By applying the perturbation method, the total potential can be written by:

$$\Phi = \sum \varepsilon^{(n)} (\Phi_I^{(n)} + \Phi_D^{(n)} + \Phi_R^{(n)}) \tag{3.14}$$

The diffraction wave force and the radiation wave force have a significant effect on a floating platform in deep water. The diffraction wave represents the scattered term from the fixed body due to the presence of the incident wave. On the other hand, the radiation wave means the wave to be propagated by the oscillating body in calm water. The forces induced by them are evaluated by integration of the pressure around the surface of the floating structure using the diffraction and the radiation potential, which can be obtained by solving the BVPs of them.

First-Order Boundary Value Problem

By separation of variable for the first-order component, the first-order potential can be written by:

$$\begin{aligned}\Phi^{(1)} &= \varepsilon(\Phi_I^{(1)} + \Phi_D^{(1)} + \Phi_R^{(1)}) \\ &= \mathrm{Re}\left[\left\{\phi_I^{(1)}(x,y,z) + \phi_D^{(1)}(x,y,z) + \phi_R^{(1)}(x,y,z)\right\}\cdot e^{-i\omega t}\right]\end{aligned} \tag{3.15}$$

By referring to the equation (3.8), the solution of incident wave velocity potential is inferred as follows:

$$\phi_I^{(1)} = \mathrm{Re}\left[\frac{-igA}{\omega}\frac{\cosh k(z+d)}{\cosh kd}\right] \tag{3.16}$$

The BVPs for the first-order potential of diffraction and radiation are defined as the following formula:

$$\nabla^2\phi_{D,R}^{(1)} = 0 \qquad \text{in the fluid } (z<0) \tag{3.17}$$

$$\left(-\omega^2 + \frac{\partial}{\partial z}\right)\phi_{D,R}^{(1)} = 0 \qquad \text{on the free surface } (z=0) \tag{3.18}$$

$$\frac{\partial\phi_{D,R}^{(1)}}{\partial z} = 0 \qquad \text{on the bottom } (z=-d) \tag{3.19}$$

$$\left.\begin{aligned}\frac{\partial\phi_D^{(1)}}{\partial n} &= -\frac{\partial\phi_I^{(1)}}{\partial n} \\ \frac{\partial\phi_R^{(1)}}{\partial n} &= -i\omega\mathrm{n}\cdot(\xi^{(1)} + \alpha^{(1)}\times\mathrm{r})\end{aligned}\right\} \qquad \text{on the body surface} \tag{3.20}$$

$$\lim_{\zeta\to\infty}\sqrt{r}\left(\frac{\partial}{\partial\zeta} \pm ik\right)\phi_{D,R}^{(1)} = 0 \qquad \text{at far field} \tag{3.21}$$

where $\mathbf{r}$ is the position vector on the body surface, R is the radial distance from the origin ($r^2 = x^2 + y^2$), $\mathrm{n} = (n_x, n_y, n_z)$ is the outward unit normal vector on the body

surface, $\Xi^{(1)}$ is the first-order translational motion of the body, and $\mathrm{A}^{(1)}$ is the first-order rotational motion of body. The $\Xi^{(1)}$ and $\mathrm{A}^{(1)}$ can be expressed as follows:

$$\Xi^{(1)} = \mathrm{Re}\left[\xi^{(1)} e^{-i\omega t}\right], \qquad \Xi^{(1)} = (\xi_1^{(1)}, \xi_2^{(1)}, \xi_3^{(1)}) \tag{3.22}$$

$$\mathrm{A}^{(1)} = \mathrm{Re}\left[\alpha^{(1)} e^{-i\omega t}\right], \qquad \alpha^{(1)} = (\alpha_1^{(1)}, \alpha_2^{(1)}, \alpha_3^{(1)}) \tag{3.23}$$

where 1,2,3 means the x-, y-, z- axis, respectively. Thus, $\xi_1^{(1)}, \xi_2^{(1)}, \xi_3^{(1)}$ are defined as the amplitude of surge, sway and heave motion, while $\alpha_1^{(1)}, \alpha_2^{(1)}, \alpha_3^{(1)}$ are defined as the amplitude of roll, pitch and yaw motion. The six degrees of freedom of the first order motion are rewritten as:

$$\varsigma_j = \begin{cases} \xi_j^{(1)} & \text{for } j = 1,2,3 \\ \alpha_{j-3}^{(1)} & \text{for } j = 4,5,6 \end{cases} \tag{3.24}$$

The radiation potential can be decomposed as follows:

$$\phi_R^{(1)} = \sum_{j=1}^{6} \varsigma_j \phi_j^{(1)} \tag{3.25}$$

where $\phi_j^{(1)}$ represents the velocity potential of rigid body motion with unit amplitude in the j th mode when the incident wave does not exist. Equation (3.25) should satisfy the boundary conditions of equation (3.18) to (3.21). The body boundary condition of $\phi_j^{(1)}$ is written as:

$$\frac{\partial \phi_j^{(1)}}{\partial n} = -i\omega n_j \qquad \text{for } j = 1,2,3 \tag{3.26}$$

$$\frac{\partial \phi_j^{(1)}}{\partial n} = -i\omega (\mathrm{r} \times \mathrm{n})_{j-3} \qquad \text{for } j = 4,5,6 \tag{3.27}$$

These boundary conditions are valid on the body surface. The diffraction potential problem, equation (3.17), can be solved numerically in consideration of the boundary conditions (equation (3.18)-(3.21)).

Second-Order Boundary Value Problem

The second-order boundary value problem is made by considering the interaction of bichromatic incident waves of frequency ω_m and ω_n with a floating body. The Volterra series method will be applied to solve the second-order BVP. If the second-order terms are taken from the perturbation formulation (3.14) and the separation of variable is applied, the second-order potential is derived by:

$$\begin{aligned}\Phi^{(2)}(x,y,z,t) &= \varepsilon^2(\Phi_I^{(2)} + \Phi_D^{(2)} + \Phi_R^{(2)}) \\ &= \mathrm{Re}\Big[\{\phi_I^-(x,y,z) + \phi_D^-(x,y,z) + \phi_R^-(x,y,z)\}\cdot e^{-i\omega^- t} \\ &\quad + \{\phi_I^+(x,y,z) + \phi_D^+(x,y,z) + \phi_R^+(x,y,z)\}\cdot e^{-i\omega^+ t}\Big]\end{aligned} \tag{3.28}$$

where $\omega^- = \omega_m - \omega_n$ is the difference-frequency, $\omega^+ = \omega_m + \omega_n$ is the sum frequency, ϕ^- is the difference-frequency potential, and ϕ^+ is the sum-frequency potential. The difference-potential and sum-frequency potential can be solved independently. The governing equation (3.1) or (3.2) can be solved for each potential component of equation (3.28) considering the boundary conditions, equation (3.3) to (3.5) as follows:

$$\phi_I^+ = \frac{1}{2}\left(\gamma_{mn}^+ + \gamma_{nm}^+\right)\frac{\cosh k^+(z+d)}{\cosh k^+ d}e^{ik^+ x} \tag{3.29}$$

$$\phi_I^- = \frac{1}{2}\left(\gamma_{mn}^- + \gamma_{nm}^{-*}\right)\frac{\cosh k^-(z+d)}{\cosh k^- d}e^{ik^- x} \tag{3.30}$$

where

$$\gamma_{mn}^{+} = -\frac{igA_m A_n}{2\omega_m} \frac{k_m^2\left(1-\tanh^2 k_m d\right)+2k_m k_n\left(1-\tanh k_m d \tanh k_n d\right)}{\nu^{+}-k^{+}\tanh k^{+} d} \tag{3.31}$$

and

$$\gamma_{mn}^{-*} = -\frac{igA_m A_n^{*}}{2\omega_m} \frac{k_m^2\left(1-\tanh^2 k_m d\right)-2k_m k_n\left(1+\tanh k_m d \tanh k_n d\right)}{\nu^{-}-k^{-}\tanh k^{-} d} \tag{3.32}$$

and the asterisk represents a complex conjugate, and $\nu^{\pm}$ and $k^{\pm}$ are defined respectively by:

$$\nu^{\pm} = \frac{(\omega^{\pm})^2}{g}, \qquad k^{\pm} = k_m \pm k_n \tag{3.33}$$

The second-order diffraction and radiation potential, $\phi_{D,R}^{(2)}$, deal with the second interaction of plane bichromatic incident waves. The second-order diffraction potential, $\phi_D^{(2)}$, contains the contributions of the second-order incident potential and the first-order potential. The governing equation of the second-order radiation potential is only expressed by the outgoing waves propagated by the second-order body motion. Thus, the governing equation of the second-order diffraction potential is defined by:

$$\nabla^2\phi_D^{\pm} = 0 \qquad \text{in the quiescent fluid volume } (z<0) \tag{3.34}$$

$$\left[-\left(\omega^{\pm}\right)^2 + g\frac{\partial}{\partial z}\right]\phi_D^{\pm} = Q^{\pm} \qquad \text{on the free surface } (z=0) \tag{3.35}$$

$$\frac{\partial\phi_D^{\pm}}{\partial z} = 0 \qquad \text{on the bottom } (z=-d) \tag{3.36}$$

$$\frac{\partial\phi_D^{\pm}}{\partial n} = -\frac{\partial\phi_I^{\pm}}{\partial n} + B^{\pm} \qquad \text{on the body surface} \tag{3.37}$$

$$Q^{\pm} \qquad \text{Boundary condition at far field} \tag{3.38}$$

where $Q^{\pm}$ are the sum and difference frequency components of the free surface force and $B^{\pm}$ are the sum and difference frequency components of the body surface force. The $Q^{\pm}$ are symmetric and expressed as follows:

$$Q^{+} = \frac{1}{2}\left(q_{mn}^{+} + q_{nm}^{+}\right), \qquad Q^{-} = \frac{1}{2}\left(q_{mn}^{-} + q_{nm}^{-*}\right) \tag{3.39}$$

and,

$$q_{mn}^{+} = -\frac{i\omega_m}{g}\phi_n^{(1)}\left(-\omega^2\frac{\partial\phi_m^{(1)}}{\partial z} + g\frac{\partial^2\phi_m^{(1)}}{\partial z^2}\right) + i\omega_n\nabla\phi_m^{(1)}\nabla\phi_n^{(1)} - q_{II}^{+} \tag{3.40}$$

$$q_{mn}^{-} = -\frac{i\omega_m}{g}\phi_n^{(1)*}\left(-\omega^2\frac{\partial\phi_m^{(1)}}{\partial z} + g\frac{\partial^2\phi_m^{(1)}}{\partial z^2}\right) + i\omega_n\nabla\phi_m^{(1)}\nabla\phi_n^{(1)*} - q_{II}^{-} \tag{3.41}$$

The $B^{\pm}$ are also symmetric and expressed as follows:

$$B^{+} = \frac{1}{2}\left(b_{mn}^{+} + b_{nm}^{+}\right), \qquad B^{-} = \frac{1}{2}\left(b_{mn}^{-} + b_{nm}^{-*}\right) \tag{3.42}$$

and,

$$b_{mn}^{+} = -\frac{1}{2}\mathrm{n}\cdot\left(\varsigma_n^{(1)}\cdot\nabla\right)\nabla\phi_m^{(1)} \tag{3.43}$$

$$b_{mn}^{-} = -\frac{1}{2}\mathrm{n}\cdot\left(\varsigma_n^{(1)*}\cdot\nabla\right)\nabla\phi_m^{(1)} \tag{3.44}$$

The boundary condition (3.37) for the second-order diffraction potential needs to be applied to the decomposed diffraction potential into a homogenous term and a particular solution term due to the complication. The homogeneous term of the second-order diffraction potential has the far-field propagating behavior, while the free surface force $Q^{\pm}$ are dominant in the particular equation term.

The governing equation and boundary conditions for the second-order radiation potential $\phi_R^{\pm}$ are defined as the first-order radiation BVP, since the boundary conditions for the radiation potential do not contain any other potentials:

$$\nabla^2\phi_R^{\pm} = 0 \qquad \text{in the fluid } (z<0) \tag{3.45}$$

$$\left(-\omega^2 + \frac{\partial}{\partial z}\right)\phi_R^{\pm} = 0 \qquad \text{on the free surface } (z=0) \tag{3.46}$$

$$\frac{\partial\phi_R^{\pm}}{\partial z} = 0 \qquad \text{on the bottom } (z=-d) \tag{3.47}$$

$$\frac{\partial\phi_R^{\pm}}{\partial n} = -i\omega\mathbf{n}\cdot(\xi^{\pm} + \alpha^{\pm}\times\mathrm{r}) \qquad \text{on the body surface} \tag{3.48}$$

$$\lim_{R\to\infty}\sqrt{R}\left(\frac{\partial}{\partial R} \pm ik\right)\phi_R^{\pm} = 0 \qquad \text{at far field} \tag{3.49}$$

where $\xi^{\pm}$ and $\alpha^{\pm}$ are the second order translations and rotational motions of the body at the sum and difference frequencies. Therefore, the second-order radiation potential has the same formula as the first-order radiation potential.

3.2. Hydrodynamic Forces

3.2.1. First-order Hydrodynamic Forces and Moments

If all of the potentials are solved, the first-order force and moment can be obtained from the integration over the whole surface pressure on the body. The pressure on the body surface ($\partial\Omega_B$) is obtained from the potential as follows:

$$P^{(1)} = -\rho\left(\frac{\partial\Phi^{(1)}}{\partial t} + gz\right) \tag{3.50}$$

where ρ is the fluid density. The six components of forces and moments are calculated as follows:

$$F_j^{(1)}(t) = -\rho g \iint_{\partial\Omega_B} z n_j dS - \rho \,\mathrm{Re}\left[i\omega \varsigma_j e^{-i\omega t} \iint_{\partial\Omega_B} \phi_j n_j dS \right] - \rho \,\mathrm{Re}\left[i\omega A e^{-i\omega t} \iint_{\partial\Omega_B} (\phi_I + \phi_D) n_j dS \right], \quad j = 1...6 \quad (3.51)$$

where,

$$\mathrm{n} = \begin{cases} (n_1, n_2, n_3) & \text{for} \quad j = 1,2,3 \\ (n4, n5, n6) = \mathrm{r} \times \mathrm{n} & \text{for} \quad j = 4,5,6 \end{cases} \quad (3.52)$$

In the above equation (3.51), the three terms represent the different contributions to the body forces and moments. The first term ($\mathrm{F}_S^{(1)}$) is the hydrostatic restoring force, the second term ($\mathrm{F}_R^{(1)}$) is the force term due to the radiation potential, and the last term ($\mathrm{F}_E^{(1)}$) is the exciting forces generated by the incident and the diffraction potentials. The hydrostatic restoring forces are defined as the multiplication of the restoring stiffness and the motion responses, and the components of restoring stiffness are defined as the following surface-integral form over the wetted body surface at mean position ($\partial\Omega_B$):

$$\mathrm{F}_S^{(1)} = -[\mathrm{K}]\{\varsigma^{(1)}\} \quad (3.53)$$

where

$$
\begin{aligned}
K_{33} &= \rho g \iint_{\partial\Omega_B} n_3 dS = \rho g A_{wp} \\
K_{34} &= \rho g \iint_{\partial\Omega_B} y n_3 dS = \rho g A_{wp} y_f \\
K_{35} &= -\rho g \iint_{\partial\Omega_B} x n_3 dS = \rho g A_{wp} x_f \\
K_{44} &= \rho g \iint_{\partial\Omega_B} y^2 n_3 dS + \rho g \forall z_b - mgz_{cg} \\
K_{45} &= -\rho g \iint_{\partial\Omega_B} xy n_3 dS \\
K_{46} &= -\rho g \forall x_b + mgx_{cg} \\
K_{55} &= \rho g \iint_{\partial\Omega_B} x^2 n_3 dS + \rho g \forall z_b - mgz_{cg} \\
K_{56} &= -\rho g \forall y_b + mgy_{cg}
\end{aligned}
\tag{3.54}
$$

where $K_{mn} = K_{nm}$ for all m and n, A_{wp} is the water plane area, x_f and y_f are the distances from the center of the water plane area to the center of gravity in x-direction and in y-direction, respectively, $\forall$ is the buoyancy of the body, (x_{cg}, y_{cg}, z_{cg}) is the center of gravity, and (x_b, y_b, z_b) is the center of buoyancy of the body.

The hydrostatic restoring stiffness will be used for the motion analysis of the floating body. The radiation potential forces and moments corresponding to the second term of the equation (3.51) can be rewritten as the form:

$$
\begin{aligned}
\mathrm{F}_R^{(1)} &= -\rho \,\mathrm{Re}\left[\varsigma_j e^{-i\omega t} \iint_{\partial\Omega_B} \frac{\partial \phi_j}{\partial n} \phi_j dS \right] \\
&= \mathrm{Re}\left(\mathrm{M}^a \ddot{\varsigma}^{(1)} + \mathrm{C} \dot{\varsigma}^{(1)} \right) = \mathrm{Re}\left[\left(-\omega^2 \mathrm{M}^a - i\omega \mathrm{C} \right) \varsigma_j e^{-i\omega t} \right]
\end{aligned}
\tag{3.55}
$$

where M^a is the added mass coefficients, C is the radiation damping coefficients, and $\varsigma = \varsigma e^{-i\omega t}$ are the body motions of six degrees of freedom. They can be represented as follows:

$$\mathrm{M}^a = \rho \mathrm{Re}\left[\iint_{\partial\Omega_B} \frac{\partial \phi_j}{\partial n} \phi_j dS \right] \tag{3.56}$$

$$\mathrm{C} = \rho \mathrm{Im}\left[\iint_{\partial\Omega_B} \frac{\partial \phi_j}{\partial n} \phi_j dS \right] \tag{3.57}$$

They are symmetric and dependent on the frequency of the body motion.

The last term of the equation (3.51) corresponds to the linear wave exciting force, and it can be rewritten as the form:

$$\mathrm{F}_E^{(1)} = -\rho \mathrm{Re}\left[A e^{-i\omega t} \iint_{\partial\Omega_B} (\phi_I + \phi_D) \frac{\partial \phi_j}{\partial n} dS \right] \tag{3.58}$$

Therefore, the equation of motion is formed as:

$$\mathrm{M}\ddot{\varsigma}^{(1)} = \mathrm{F}_S^{(1)} + \mathrm{F}_R^{(1)} + \mathrm{F}_E^{(1)} = -\mathrm{K}\varsigma - \left(\mathrm{M}^a \ddot{\varsigma} + \mathrm{C}\dot{\varsigma}\right) + \mathrm{F}_E^{(1)} \tag{3.59}$$

where M is the mass matrix of the body, which is described as:

$$\mathrm{M} = \begin{bmatrix} m & 0 & 0 & 0 & mz_{cg} & -my_{cg} \\ 0 & m & 0 & -mz_{cg} & 0 & mx_{cg} \\ 0 & 0 & m & my_{cg} & -mx_{cg} & 0 \\ 0 & -mz_{cg} & my_{cg} & I_{11} & I_{12} & I_{13} \\ mz_{cg} & 0 & -mx_{cg} & I_{21} & I_{22} & I_{23} \\ -my_{cg} & mx_{cg} & 0 & I_{31} & I_{32} & I_{33} \end{bmatrix} \tag{3.60}$$

where V represents the body volume, $m = \iiint_{\forall} \rho_B dV$ is the body mass, $I_{mn} = \iiint_{\forall} \rho_B \left(\mathrm{x} \cdot \mathrm{x} \delta_{mn} - x_m x_n \right) dV$ is the moment of inertia, ρ_B is the density of the body, and δ_{mn} is the Kronecker delta function.

3.2.2. Second-order Hydrodynamic Forces and Moments

The second-order wave forces and moments on the body can be obtained by direct integration of the hydrodynamic pressure over the wetted surface of the body at the instantaneous time step. The second-order pressure is defined as:

$$P^{(2)} = -\rho \frac{\partial \Phi^{(2)}}{\partial t} - \frac{1}{2} \rho \left(\nabla \Phi^{(1)} \right)^2 \tag{3.61}$$

In consideration of the bichromatic wave, the second-order pressure is modified as:

$$P^{(2)} = \mathrm{Re} \sum_{m=1}^{2} \sum_{n=1}^{2} \left[A_m A_n p_{mn}^{+} e^{-i\omega^{+} t} + A_m A_n^{*} p_{mn}^{-} e^{-i\omega^{-} t} \right] \tag{3.62}$$

where $p_{mn}^{\pm}$ are defined as the sum and difference frequency quadratic transfer functions for the second-order pressure. The second-order forces and moments are defined as:

$$\mathrm{F}^{(2)} = \mathrm{F}_S^{(2)} + \mathrm{F}_R^{(2)} + \mathrm{F}_E^{(2)} \tag{3.63}$$

where $\mathrm{F}_S^{(2)}$ represents the second-order hydrostatic force, $\mathrm{F}_E^{(2)} = \mathrm{F}_p^{(2)} + \mathrm{F}_q^{(2)}$ is the second-order wave exciting force, and , $\mathrm{F}_R^{(2)}$ is the radiation potential force. The components of $\mathrm{F}_E^{(2)}$ are defined as $\mathrm{F}_p^{(2)} = \mathrm{F}_I^{(2)} + \mathrm{F}_D^{(2)}$, which denotes the incident and diffraction potential forces, and $\mathrm{F}_q^{(2)}$ denotes the quadratic product of the first-order forces. The component forces are derived in the integration forms of potentials as follows:

$$\mathrm{F}_S^{(2)} = \rho g A_{wp}\left(\xi_z^{(2)} + y_f \alpha_x^{(2)} - x_f \alpha_y^{(2)}\right)k \tag{3.64}$$

$$\mathrm{F}_R^{(2)} = \rho \iint_{\partial\Omega_B} \frac{\partial \Phi_R^{(2)}}{\partial t} n dS \tag{3.65}$$

$$\mathrm{F}_{I,D}^{(2)} = \rho \iint_{\partial\Omega_B} \frac{\partial \Phi_{I,D}^{(2)}}{\partial t} n dS \tag{3.66}$$

$$\mathrm{F}_E^{(2)} = \mathrm{Re}\sum_{m=1}^{2}\sum_{n=1}^{2}\left[A_m A_n f_{mn}^{+} e^{-i\omega^{+}t} + A_m A_n^{*} f_{mn}^{-} e^{-i\omega^{-}t}\right] \tag{3.67}$$

where $f_{mn}^{\pm}$ denote the quadratic transfer function (QTF) of the sum and difference frequency exciting force. QTF is obtained by the addition of $h_{mn}^{\pm}$ and $g_{mn}^{\pm}$, where $h_{mn}^{\pm}$ are the contribution of first-order quadratic transfer function and $g_{mn}^{\pm}$ are the summation of the quadratic transfer function of the sum and difference frequency exciting force due to the incident potential and the diffraction potential. Each component of the QTF is defined as:

$$f_{mn}^{\pm} = h_{mn}^{\pm} + g_{mn}^{\pm} \tag{3.68}$$

$$h_{mn}^{+} = \left[-\frac{\rho}{4}\iint_{\partial\Omega_B}\left(\nabla\phi_m^{(1)} \cdot \nabla\phi_n^{(1)}\right)\mathrm{n} dS - \frac{\rho\omega_m\omega_n}{4g}\int_{L_w}\phi_m^{(1)}\phi_n^{(1)}\mathrm{N} dL\right] / A_m A_n \tag{3.69}$$

$$h_{mn}^{-} = \left[-\frac{\rho}{4}\iint_{\partial\Omega_B}\left(\nabla\phi_m^{(1)} \cdot \nabla\phi_n^{(1)*}\right)\mathrm{n} dS - \frac{\rho\omega_m\omega_n}{4g}\int_{L_w}\phi_m^{(1)}\phi_n^{(1)*}\mathrm{N} dL\right] / A_m A_n^{*} \tag{3.70}$$

$$g_{mn}^{\pm} = \left[\rho i\omega^{\pm}\iint_{\partial\Omega_B}\left(\phi_I^{\pm} + \phi_D^{\pm}\right)\mathrm{n} dS\right] / \left(A_m A_n, A_m A_n^{*}\right) \tag{3.71}$$

where $\mathrm{N} = \mathrm{n}/\sqrt{\left(1 - n_z^2\right)}$, and k is the unit vector in the *z*-direction.

3.3. Boundary Element Method

The boundary element method is proper for solving the boundary value problem of the fluid potential around the floating body since there is no analytic solution except for some special geometric bodies. BEM is generally called the inverse formulation, since the solution to satisfy all of the boundary conditions, except the body boundary condition for the first-order potential and the body boundary condition and the free surface condition for the second-order potential, is used as a weighting function. It is also based on Green-Lagrange's Identity given by:

$$\iiint_{\Omega}\left(G\nabla^2\phi-\phi\nabla^2 G\right)d\Omega=\iint_{\partial\Omega}\left(G\frac{\partial\phi}{\partial n}-\phi\frac{\partial G}{\partial n}\right)dS \tag{3.72}$$

where G is the Green function to satisfy all of the boundary conditions, Ω denotes the fluid domain, and $\partial\Omega$ denotes the boundary of the domain. ϕ is the exact solution of potential and G satisfies the following equation:

$$\nabla^2 G=\delta(\mathbf{x}) \tag{3.73}$$

where δ is Dirac delta function, and $\mathbf{x}$ means the position coordinates. Since ϕ and G satisfy all of the boundary conditions except the body or the free surface, the right hand side of the equation (3.72) becomes:

$$c(\mathrm{x})\phi(\mathrm{x})=\iint_{\partial\Omega_B}\left(G\frac{\partial\phi}{\partial n}-\phi\frac{\partial G}{\partial n}\right)dS+\iint_{\partial\Omega_F}\left(G\frac{\partial\phi}{\partial n}-\phi\frac{\partial G}{\partial n}\right)dS \tag{3.74}$$

where $c(\mathrm{x})$ means a shape factor depending on the body geometry, $\partial\Omega_B$ represents the body boundary, and $\partial\Omega_F$ is the free surface boundary. If the body geometry has a

smooth surface, $c(\mathrm{x})$ becomes 2π . The equation (3.74) is a fundamental equation called the Inverse Formulation.

If the formulation is applied to the first-order diffraction potential problem for the smooth surface of body, the equation (3.74) becomes a second kind of Fredholm integral equation such as:

$$2\pi\phi_D^{(1)}(\mathrm{x}) + \iint_{\partial\Omega_B} \phi_D^{(1)}(\xi)\frac{\partial G(\xi;\mathrm{x})}{\partial n}dS(\xi) = \iint_{\partial\Omega_B} G(\xi;\mathrm{x})\left(-\frac{\partial\phi_I^{(1)}(\xi)}{\partial n}\right)dS(\xi) \tag{3.75}$$

where ξ denotes the source point coordinates. If it is applied to the first-order radiation potential problem, it becomes as:

$$2\pi\phi_R^{(1)}(\mathrm{x}) + \iint_{\partial\Omega_B} \phi_R^{(1)}(\xi)\frac{\partial G(\xi;\mathrm{x})}{\partial n}dS(\xi) = \begin{cases} \iint_{\partial\Omega_B} G(\xi;\mathrm{x})n_k dS(\xi) & \text{for } k=1,2,3 \\ \iint_{\partial\Omega_B} G(\xi;\mathrm{x})(\mathrm{r}\times\mathrm{n})_{k-3} dS(\xi) & \text{for } k=4,5,6 \end{cases} \tag{3.76}$$

If the formulation is applied to the second-order diffraction potential problem for the flat surface of body, it becomes as:

$$2\pi\phi_D^{\pm} + \iint_{\partial\Omega_B} \phi_D^{\pm}\frac{\partial G^{\pm}}{\partial n}dS = \iint_{\partial\Omega_B} G^{\pm}\left(B^{\pm} - \frac{\partial\phi_I^{\pm}}{\partial n}\right)dS + \frac{1}{g}\iint_{\partial\Omega_F} Q^{\pm}G^{\pm}dS \tag{3.77}$$

If it is applied to the second-order radiation potential problem for a far field, it becomes as:

$$2\pi\phi_R^{\pm} + \iint_{\partial\Omega_B} \phi_R^{\pm}\frac{\partial G^{\pm}}{\partial n}dS = \begin{cases} \iint_{\partial\Omega_B} G^{\pm}n_k dS + \iint_{\partial\Omega_F}\left(\omega^2 G^{\pm}\phi_R^{\pm} \mp \lim_{R\to\infty} ik\sqrt{R}\phi_R^{\pm}\right)dS & \text{for } k=1,2,3 \\ \iint_{\partial\Omega_B} G^{\pm}(\mathrm{r}\times\mathrm{n})_{k-3} dS + \iint_{\partial\Omega_F}\left(\omega^2 G^{\pm}\phi_R^{\pm} \mp \lim_{R\to\infty} ik\sqrt{R}\phi_R^{\pm}\right)dS & \text{for } k=4,5,6 \end{cases} \tag{3.78}$$

In this formulation, it is noted that the integration term for the free surface remains. If the Constant Panel Method (CPM) of BEM is taken, the simplest form is shown as:

$$2\pi\phi(\mathrm{x}) + \iint_{\partial\Omega_B} \phi(\xi)\frac{\partial G(\xi,\mathrm{x})}{\partial n(\xi)}dS(\xi) = \iint_{\partial\Omega_B} G(\xi,\mathrm{x})\frac{\partial \phi(\xi)}{\partial n(\xi)}dS(\xi) \tag{3.79}$$

If the equation is applied for the discretized model, it is modified as:

$$\phi(\xi) = \sum_{j=1}^{L} N_j(x_1, x_2)\phi_j \ , \quad L = 1,2,...,(\text{No. of Interpolaton points}) \tag{3.80}$$

$$\sum_{j=1}^{M} H_{ij}\phi_j = \sum_{j=1}^{M} G_{ij}\left(\frac{\partial\phi}{\partial n}\right)_j \ , \quad M = 1,2,...,(\text{No of pannels}) \tag{3.81}$$

where N_j is the shape function, (x_1, x_2) is the local coordinate, and H_{ij} and G_{ij} are as follows:

$$H_{ij} = \frac{1}{2}\delta_{ij} + \frac{1}{4\pi}\iint_{\partial\Omega_B, j\neq i} \frac{\partial G(\xi,\mathrm{x})}{\partial n(\xi)}dS(\xi) \tag{3.82}$$

$$G_{ij} = \frac{1}{4\pi}\iint_{\partial\Omega_B, j\neq i} G(\xi,\mathrm{x})dS(\xi) \tag{3.83}$$

In the equations of (3.81) and (3.83), $\frac{\partial\phi}{\partial n}$ is given by the equation (3.20) and $G(\xi,\mathrm{x}), \frac{\partial G(\xi,\mathrm{x})}{\partial n(\xi)}$ are known as the exact forms. Thus, the equation (3.81) can be solved for the whole panels.

For the BEM program, the WAMIT (Lee et al, 1991) of CPM is well known in this field. the WAMIT can be applied to the first-order and second-order

diffraction/radiation potential problem. In this study, the WAMIT will be taken for solving the fluid interaction problem of the multiple-body system.

3.4. Motions of the Floating Platform

3.4.1. Wave Loads

The linear wave forces are calculated in the frequency domain, and the second-order sum and difference frequency wave loads are computed by considering the bichromatic wave interactions. The real sea is made of random waves, so that it is essential to make the random waves for applying the external wave loads to the floating body.

The linear and the second-order hydrodynamic forces can be rewritten as the form of a two-term Volterra series in time domain:

$$F^{(1)}(t) + F^{(2)}(t) = \int_{-\infty}^{\infty} h_1(\tau)\eta(t-\tau)d\tau + \int_{-\infty}^{\infty}\int_{-\infty}^{\infty} h_2(\tau_1,\tau_2)\eta(t-\tau_1)\eta(t-\tau_2)d\tau_1 d\tau_2 \quad (3.84)$$

where $h_1(\tau)$ is the linear impulse response function, and $h_2(\tau_1,\tau_2)$ is the quadratic impulse response function, i.e., the second-order exciting force at time t for the two different unit amplitude inputs at time τ_1 and τ_2. $\eta(t)$ is the ambient wave free surface elevation at a reference position. Since $\eta(t)$, $h_1(\tau)$ and $h_2(\tau_1,\tau_2)$ can be expressed in the functions of frequency, the unidirectional wave exciting forces induced by the incident potential and the diffraction potential to have the similar form of the equation (3.84) can be rewritten in the form of the summation of the frequency components as follows:

$$F_I^{(1)}(t) = \mathrm{Re}\left[\sum_{j=1}^{N} A_j q_L(\omega_j) e^{i\omega t}\right] \tag{3.85}$$

$$F_I^{(2)}(t) = \mathrm{Re}\left[\sum_{j=1}^{N}\sum_{k=1}^{N} A_j A_k^* q_D(\omega_j, -\omega_k) e^{i\omega^- t} + \sum_{j=1}^{N}\sum_{k=1}^{N} A_j A_k q_S(\omega_j, \omega_k) e^{i\omega^+ t}\right] \tag{3.86}$$

where $q_L(\omega_j)$ represents the linear force transfer function (LTF), and $q_D(\omega_j, -\omega_k)$ and $q_S(\omega_j, \omega_k)$ are the difference and the sum frequency quadratic transfer functions (QTF), respectively. Using the Fourier transform, the equation (3.85) and (3.86) can be easily changed into the energy spectra given by:

$$S_F^{(1)}(\omega) = S_\eta(\omega)\left|q_L(\omega)\right|^2 \tag{3.87}$$

$$S_F^-(\omega) = 8\int_0^\infty \left|q_D(\mu, \omega-\mu)\right|^2 S_\eta(\mu) S_\eta(\omega-\mu) dS_\eta(\mu) \tag{3.88}$$

$$S_F^+(\omega) = 8\int_0^{\omega/2} \left|q_S\left(\frac{\omega}{2}+\mu, \frac{\omega}{2}-\mu\right)\right|^2 S_\eta\left(\frac{\omega}{2}+\mu\right) S_\eta\left(\frac{\omega}{2}-\mu\right) dS_\eta(\mu) \tag{3.89}$$

where $S_\eta(\omega)$ is the wave spectrum, $S_F^{(1)}(\omega)$ is the linear wave force spectrum, and $S_F^-(\omega)$ and $S_F^+(\omega)$ are the second-order sum- and difference-frequency wave force spectrum, respectively.

The first- and second-order radiation potential forces are calculated by the following formula:

$$F_R(t) = \left(M^a(\omega) - \int_0^\infty R(t)\cos\omega t dt\right)\ddot{\varsigma}(t) - \int_{-\infty}^{t} R(t-\tau)\dot{\varsigma}(\tau) d\tau \tag{3.90}$$

where $M^a(\omega)$ is the added mass coefficient as defined in the equation (3.55) at frequency ω, and $R(t)$ is called a retardation function as defined below:

$$R(t) = \frac{2}{\pi}\int_0^\infty C(\omega)\frac{\sin \omega t}{\omega}\, d\omega \tag{3.91}$$

where $C(\omega)$ is the radiation damping coefficient in the equation (3.56) at frequency ω. The total wave forces and moments can be obtained by summation of the equation (3.85), (3.86) and (3.90) as the same form as the summation of the equation (3.59) and (3.63) as follows:

$$F_T = F_I + F_c + \tilde{F}_R \tag{3.92}$$

where $F_T = F^{(1)} + F^{(2)}$ is the total wave exciting force, $F_I = F_I^{(1)} + F_I^{(2)}$ is the sum of the equation (3.85) and (3.86), F_c is the last term of the right hand side of the equation (3.90), and $\tilde{F}_R$ is the first term of the equation (3.90).

3.4.2. Morison's Equation

For the slender cylindrical floating structure, the inertia and added mass effect and the damping effect of the drag force on the slow drift motion can be evaluated by using Morison's equation. Morison et al. (1950) proposed that the total force is the sum of drag force and inertia force as follows:

$$F_m = C_m \rho V \dot{u}_n - C_a \rho V \ddot{\varsigma}_n + \frac{1}{2}\rho C_D D_S (u_n - \dot{\varsigma}_n)|u_n - \dot{\varsigma}_n| \tag{3.93}$$

where F_m denotes Morison's force, $V = \frac{\pi D^2}{4}$ is the volume per unit length of the structure, D is the diameter of the slender body, $C_m = 1 + C_a$ is the inertia coefficient,

C_a is the added mass coefficient, C_D is the drag coefficient, D_S is the breadth or diameter of the structure, $\dot{u}_n$ and u_n are the acceleration and the velocity of the fluid normal to the body, respectively, and $\ddot{\varsigma}_n$ and $\dot{\varsigma}_n$ are the acceleration and the velocity of the body, respectively. In the above equation, the first term is called Froude-Krylov force, the second term the added mass effect, and the last term the drag force. The drag force on the floating structure cannot be neglected, because the slenderness ratio of the structure (the ratio of breadth or diameter to the length of the structure) is small compared to the wavelength so that the viscous effect cannot be negligible. The derived force by the equation (3.93) is added to the wave forces of the equation (3.92) to get the total force.

3.4.3. Body Motion

The equilibrium equation using Newton's second law called the momentum equation for the floating structure can be given as:

$$\mathbf{M}\frac{d^2\mathrm{x}_{cg}}{dt^2} = \mathbf{f} \tag{3.94}$$

$$\mathbf{I}\frac{d\varphi}{dt} + \varphi \times (\mathbf{I}\varphi) = \mathbf{m} \tag{3.95}$$

where M is the mass of the floating structure, $\mathbf{x}_{cg}$ is the coordinates of the center of gravity of the floating body, $\mathbf{I}$ is the moment of inertia, and φ is the angular velocity, $\mathbf{f}$ and $\mathbf{m}$ are the external force and moment. The second term of the left-hand side of the equation (3.93) and the relative angular motion of the body to the wave motion are

nonlinear. If the rotation is assumed to be small, the equation (3.95) becomes a linear equation as follows:

$$\mathbf{M}\ddot{\boldsymbol{\varsigma}} = \mathbf{F}(t) \tag{3.96}$$

where $\ddot{\boldsymbol{\varsigma}}$ is the normal acceleration of body motion, $\mathbf{M}$ is the 6×6 body mass matrix to be the same as equation (3.59) and $\mathbf{F}(t)$ is the external force vector. In the time domain, the above equation is expanded as:

$$\left[\mathrm{M} + \mathbf{M}^a(\infty)\right]\ddot{\boldsymbol{\varsigma}} + \mathrm{K}\boldsymbol{\varsigma} = \mathbf{F}_I(t) + \mathbf{F}_c(\dot{\boldsymbol{\varsigma}}, t) + \mathbf{F}_m(\dot{\boldsymbol{\varsigma}}, t) \tag{3.97}$$

where $\mathbf{M}^a(\infty)$ is a constant, equivalent added mass of the body at the infinite frequency and can be expressed by :

$$\mathbf{M}^a(\infty) = \mathrm{M}^a(\omega) - \int_0^\infty R(t)\cos\omega t dt \tag{3.98}$$

where $\mathbf{M}^a(\omega)$ is the same as defined in the equation (3.56). $\mathbf{F}_c$ is the same as the second term of the equation (3.92) and defined as:

$$\mathbf{F}_c(\dot{\boldsymbol{\varsigma}}, t) = -\int_{-\infty}^{t} \mathrm{R}(t-\tau)\dot{\boldsymbol{\varsigma}} d\tau \tag{3.99}$$

$\mathbf{F}_I$ is the same as the equation (3.85) and (3.86), and $\mathbf{F}_m$ is the force by Morison's equation such as the equation (3.93). $\dot{\boldsymbol{\varsigma}}$ is the normal velocity of the body.

3.4.4. Time Domain Solution of the Platform Motions

Since the system contains the nonlinear effect, the numerical scheme of the iterative procedure in the time domain is commonly used. The equation of motion in time domain for a single-body system and/or a two-body system is expressed as the

equation (3.97) with the equation (3.98) and (3.99). For the numerical integration in the time domain, there are several kinds of implicit methods developed, such as the Newmark-Beta method, Runge-Kuta method and the Adams-Moulton method (or mid-point method). The last is used for the purpose of the guarantee of the second-order accuracy. Another reason to use it is that the method has the merit to solve together the coupled equations of the platform motion and mooring line motions at each time step. Furthermore, the Adams-Bashforth method is also used for the time integration of the nonlinear force.

In the first step, the equation (3.97) is de-rated to the first order differential equation:

$$\tilde{\mathbf{M}}\dot{\eta} = \mathbf{F}_I(t) + \mathbf{F}_c(t,\varsigma) + \mathbf{F}_m(t,\varsigma) - \mathbf{K}\varsigma \tag{3.100}$$

$$\eta = \dot{\varsigma} \tag{3.101}$$

where $\tilde{\mathbf{M}} = \mathbf{M} + \mathbf{M}^{\mathbf{a}}(\infty)$ denotes the virtual mass matrix. If the integration from time step $t^{(n)}$ to $t^{(n+1)}$ is performed, the following equation is obtained:

$$\tilde{\mathbf{M}}\eta^{(n+1)} = \tilde{\mathbf{M}}\eta^{(n)} + \int_{t^{(n)}}^{t^{(n+1)}} (\mathbf{F}_I + \mathbf{F}_c + \mathbf{F}_m)dt - \int_{t^{(n)}}^{t^{(n+1)}} \mathbf{K}\varsigma dt \tag{3.102}$$

$$\varsigma^{(n+1)} = \varsigma^{(n)} + \int_{t^{(n)}}^{t^{(n+1)}} \eta dt \tag{3.103}$$

If the Adam-Moulton method is applied to the equation (3.102) and (3.103), the ollowing equation is obtained after the resultant equation re-arranged:

$$\tilde{\mathbf{M}}\eta^{(n+1)} = \tilde{\mathbf{M}}\eta^{(n)} + \frac{\Delta t}{2}(\mathbf{F}_I{}^{(n+1)} + \mathbf{F}_c{}^{(n+1)} + \mathbf{F}_m{}^{(n+1)} + \mathbf{F}_I{}^{(n)} + \mathbf{F}_c{}^{(n)} + \mathbf{F}_m{}^{(n)}) - \frac{\Delta t}{2}\mathbf{K}(\varsigma^{(n+1)} + \varsigma^{(n)}) \tag{3.104}$$

$$\eta^{(n+1)} = \frac{2}{\Delta t}(\varsigma^{(n+1)} - \varsigma^{(n)}) - \eta^{(n)} \tag{3.105}$$

The equations (3.104) and (3.105) are the combination of two linear algebraic equations with the unknowns of $\eta^{(n+1)}$ and $\varsigma^{(n+1)}$. To solve the above equations, the assumption of the first terms is needed. It means that the time integration may have an error term due to the arbitrary adoption of the first term. For the evaluation of the first terms of time varying unknowns to avoid the above-mentioned problem, the Adams-Bashforth scheme is used. Thus, the time integration of the nonlinear term of radiation damping force is as follows:

$$\int_{t^{(n)}}^{t^{(n+1)}} \mathbf{F}_c dt = \frac{\Delta t}{2}(3\mathbf{F}_c{}^{(n)} - \mathbf{F}_c{}^{(n-1)}) \tag{3.106}$$

$$\int_{t^{(n)}}^{t^{(n+1)}} \mathbf{F}_c dt = \Delta t \mathbf{F}_c^{(0)} \qquad \text{for } n = 0 \tag{3.107}$$

In the same sense, the time integration of the nonlinear term of drag force in Morison's formulation is as follows:

$$\int_{t^{(n)}}^{t^{(n+1)}} \mathbf{F}_m dt = \frac{\Delta t}{2}(3\mathbf{F}_m{}^{(n)} - \mathbf{F}_m{}^{(n-1)}) \tag{3.108}$$

$$\int_{t^{(n)}}^{t^{(n+1)}} \mathbf{F}_m dt = \Delta t \mathbf{F}_m^{(0)} \qquad \text{for } n = 0 \tag{3.109}$$

Eventually, the equation (3.100) and (3.101) are derived as follows:

$$\begin{aligned}\left[\frac{4}{\Delta t^2}\tilde{\mathbf{M}} + \mathbf{K}\right]\Delta\varsigma = \frac{4}{\Delta t}\tilde{\mathbf{M}}\eta^{(n)} + (\mathbf{F}_I{}^{(n+1)} + \mathbf{F}_I{}^{(n)}) + (3\mathbf{F}_c{}^{(n)} - \mathbf{F}_c{}^{(n-1)}) \\ + (3\mathbf{F}_m{}^{(n)} - \mathbf{F}_m{}^{(n-1)}) - 2\mathbf{K}\varsigma^{(n)} + 2\mathbf{F}_0\end{aligned} \tag{3.110}$$

$$\Delta\varsigma = \varsigma^{(n+1)} - \varsigma^{(n)} \tag{3.111}$$

where $\mathbf{F}_0$ represents the net buoyancy force for balancing the system. Firstly, the equation (3.110) is solved for the unknown of $\Delta\varsigma$. Then, $\eta^{(n+1)}$ and $\varsigma^{(n+1)}$ can be obtained from the equation (3.105) and (3.111). To obtain the stability and the accuracy of the solution, the time interval of Δt may be small enough to solve the mooring line dynamics, since the mooring line shows a stronger nonlinear behavior than the platform movement.

3.5. Coupled Analysis Program HARP

Coupled hull hydrodynamics, mooring and riser program HARP is modified to perform time domain global analysis with the developed internal wave. The program applies the sea wave radiation/diffraction forces calculated by program WAMIT, and the internal wave forces on the platform and moorings/risers by using Morison equation. The program performs nonlinear dynamic finite element analysis to evaluate the offshore floating platform motions and strength of flexible risers and moorings.

Calculation flow chart of the program is shown in Figure 3.1 below:

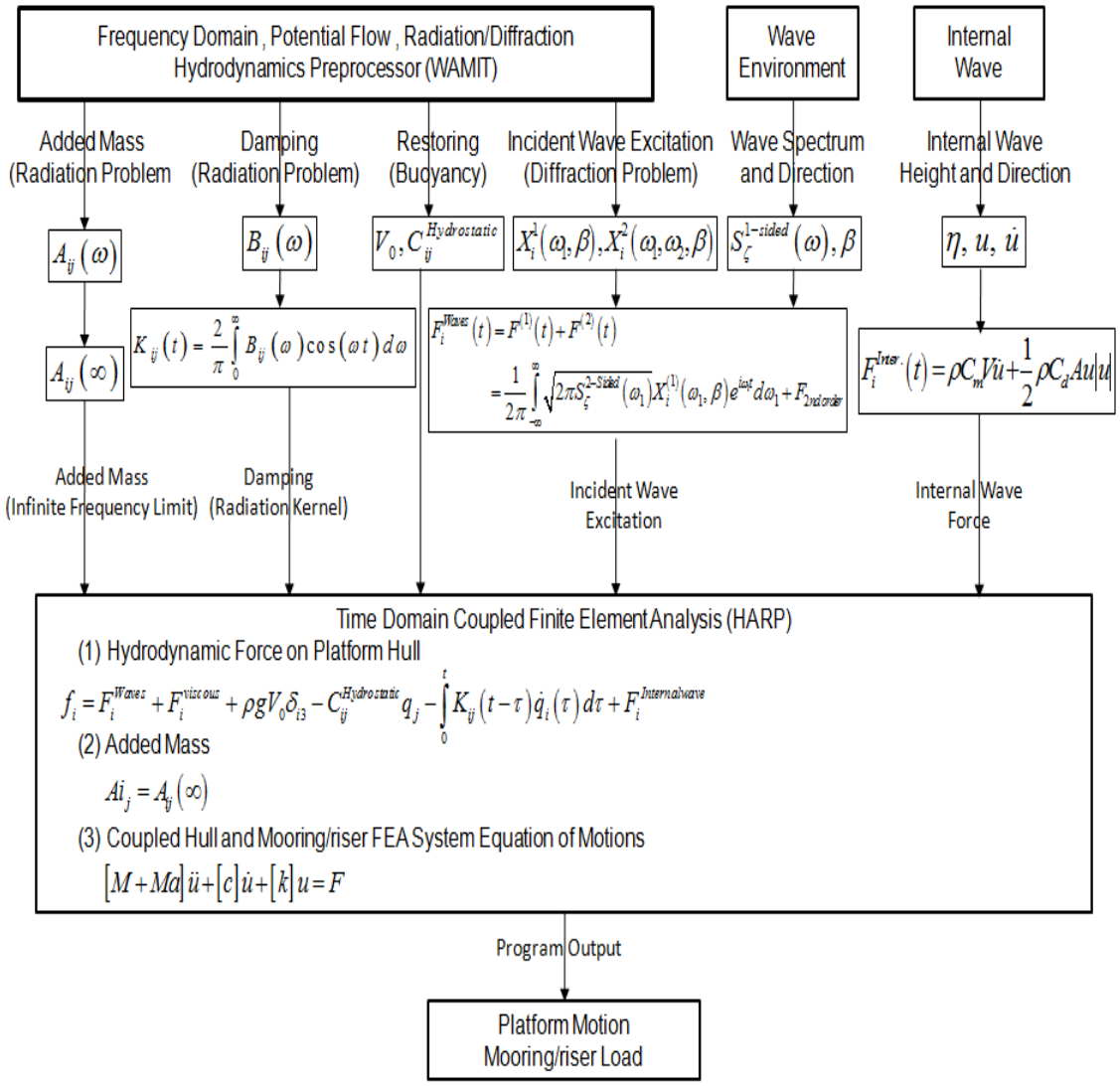

Figure 3.1 Summary of program HARP Calculations

4. APPLICATION I: NONLINEAR INTERNAL WAVE IMPACT ON OFFSHORE DRILLING UNITS

4.1. Internal Solitons in South China Sea

Large amplitude internal waves have been observed in the South China Sea (Duda and Farmer 1999; Ko et al. 2008; Vandiver and Li 2005; Vandiver et al. 2005). The source of the generation is the Luzon Strait. The East Ridge in the middle of the strait and the northern part of the west ridge are the two major topographical sources for the waves. It is seen that ocean tides are converted by the ridge into internal tides which due to nonlinear effects are transformed into undular bores. These bores lead to the formation of a internal wave train that propagates towards the west towards Dong Sha Island (Figure 4.1). In addition to the barotropic tide, the Kuroshio current is an additional source for the solitons. It is however seen that the semidiurnal tide is the most effective source of the soliton train. Internal waves upto 200 m in amplitude have been reported from satellite pictures and Multi-Channel Sea Surface Temperature (MCSST) data.

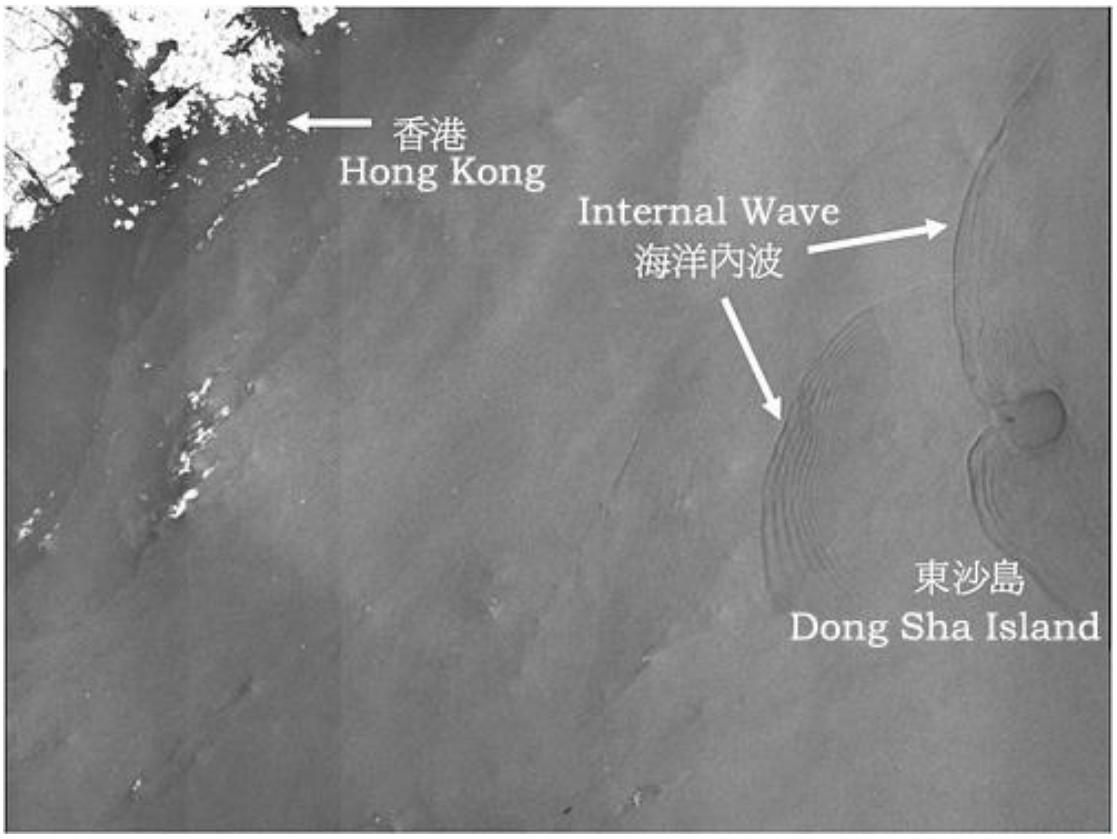

Figure 4.1 Waves near Dong Sha Island in the South China Sea. (© Hong Kong Chinese University Satellite Observation, Nov, 2006)

4.2. Environmental Parameters

The environment considered in this study is based on drilling semi-submersible design operative conditions and internal waves observed in South China Sea.

4.2.1. Field Description

A generic South China Sea field with an assumed water depth of 700 m is selected for this study. It is also assumed that the pycnocline is at 200 m below the surface.

4.2.2. Surface Wave, Wind and Current

The maximum operative and survival design environmental conditions including wave spectral parameters along with the associated wind and current, listed in Table 4.1 below are applied in the analysis. These correspond to waves with return period of 1-year and 10-year respectively.

Table 4.1 Summary of Environmental Conditions

Items	South China Sea Water Depth = 700m			
	1		2	
	1-Year Return Period Criteria		10-Year Return Period Criteria	
	Operating Condition		Survival Condition	
Wave	Jonswap		Jonswap	
Gamma	1		1	
Wave Direction (deg)	180		180	
Significant (Hs) (m)	6		10.87	
Spectral Peak Period (Tp)(s)	11.2		13.4f	
Wind	API		API	
1 Hour Avg. Wind (m/s)	21.97		38.27	
Wind Direction (deg)	180		180	
Current Profile	Normal		Normal	
	Depth (m)	Vel (m/s)	Depth (m)	Vel (m/s)
	0	1.02	0	1.43
	-10	0.83	-10	1.21
	-20	0.35	-20	0.77
	-50	0.31	-50	0.48
	-100	0.27	-100	0.39
	-150	0.26	-150	0.34
	-200	0.17	-200	0.27
	-300	0.14	-300	0.21
	-500	0.13	-500	0.19
	-700	0.13	-700	0.19
Current Direction (deg)	150		150	

4.2.3. Internal Wave

The internal wave model shown in Figure 4.2 (left) is created based on a satellite picture (Figure 4.2 right) taken on April 26, 2000 (Vandiver and Li 2005). It has a representative shape and basic characteristics of internal waves observed in South China Sea. Two sets of internal waves with wave heights of 90m and 170m are generated for the drilling semi analysis. The 90 m wave is considered to an intermediate internal wave in the south China sea while the 170 m wave corresponds to an extreme wave.

It is assumed that the internal wave may occur during the maximum operating wave condition for the drilling semi design and analysis consideration. Internal wave is not applied during the survival environmental condition, and it is analyzed for comparison purpose only.

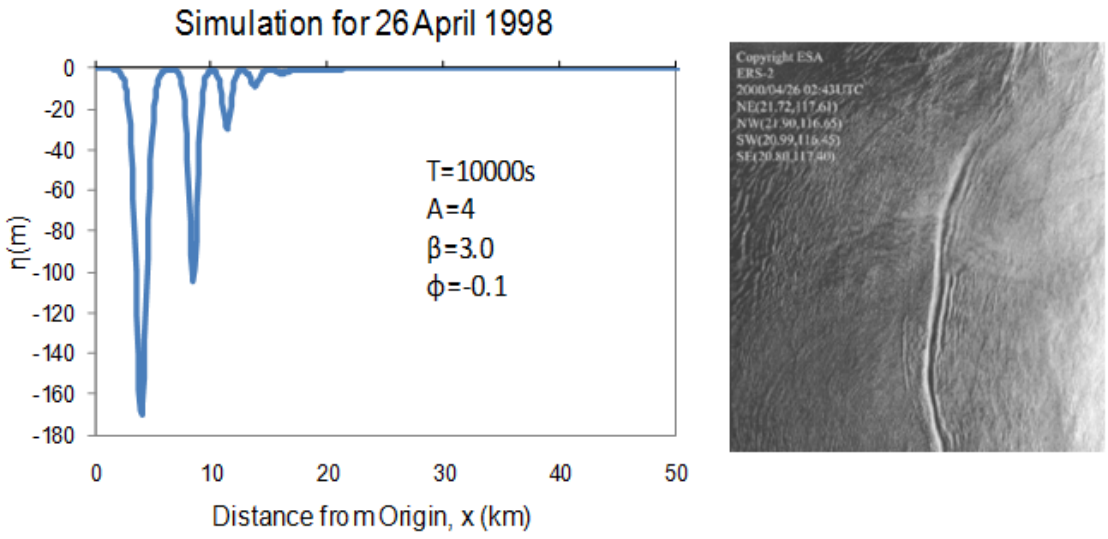

Figure 4.2 Internal Wave Model and Corresponding Satellite Picture (© ESA, April 26, 2000)

The duration between the 1st peak and 2nd peak is 26.5 minutes for the 170 m wave while it is 16.7 minutes for the 90 m wave. The duration between the 2nd peak and 3rd peak is 18.3 minutes and 11.8 minutes for the 170m and the 90m internal waves respectively. The internal wave developing time (T0) before the start of the coupled analysis is 30,000 seconds and 10,000 seconds for the 90m and the 170m internal wave. This time is selected to form a desired geometry of the internal wave based on observable data for coupled analysis. The internal group speed and the maximum velocity obtained at the sea water surface are summarized in Tables 4.2 and 4.3.

Table 4.2 Internal Wave Input Parameters

Parameters	Unit	Case 1	Case 2
Internal Wave Height	m	90	170
Upper Layer Depth	m	200	200
Upper Layer Fluid Density	kg/m^3	1020	1020
Lower Layer Depth	m	1019.2	1019.2
Lower Layer Fluid Density	kg/m^3	1028	1028
Internal Wave Pre-existing Time T_0	sec	30000	10000
Recovery Function Power (A)	-	4	4
Error Function β	-	3.0	3.0
Error Function ϕ	-	-0.1	-0.1

Table 4.3 Group Speed and Maximum Horizontal Velocity

Wave Height (m)	Group Speed (m/s)	Max. Hori. Velocity (m/s)
90	3.58	1.31
170	3.58	2.21

The time history of the internal wave height, scaled velocities, and scaled acceleration distributions are presented in Figures 4.2-4.7. It is seen that the horizontal velocity is positive above the pycnocline while it is negative below the pycnocline. The horizontal velocity is directly proportional to the vertical rate of change of the structure function (Apel 2003) which causes this shearing effect near the pycnocline. The internal wave velocities have much higher magnitude compared to the accelerations and thus have a much more significant contribution to the impact on the drilling semi system.

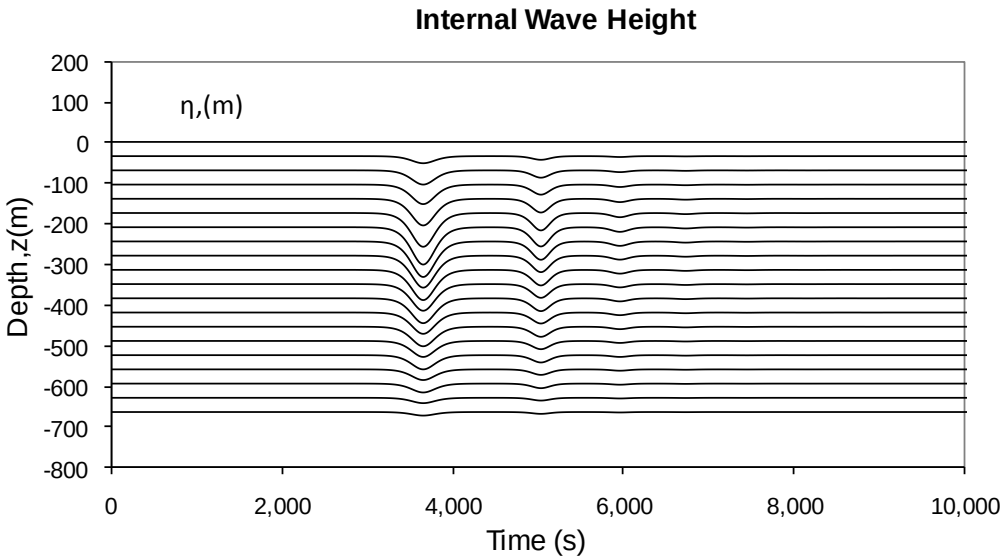

Figure 4.3 Internal Wave Height Distribution with Depth (η=90m)

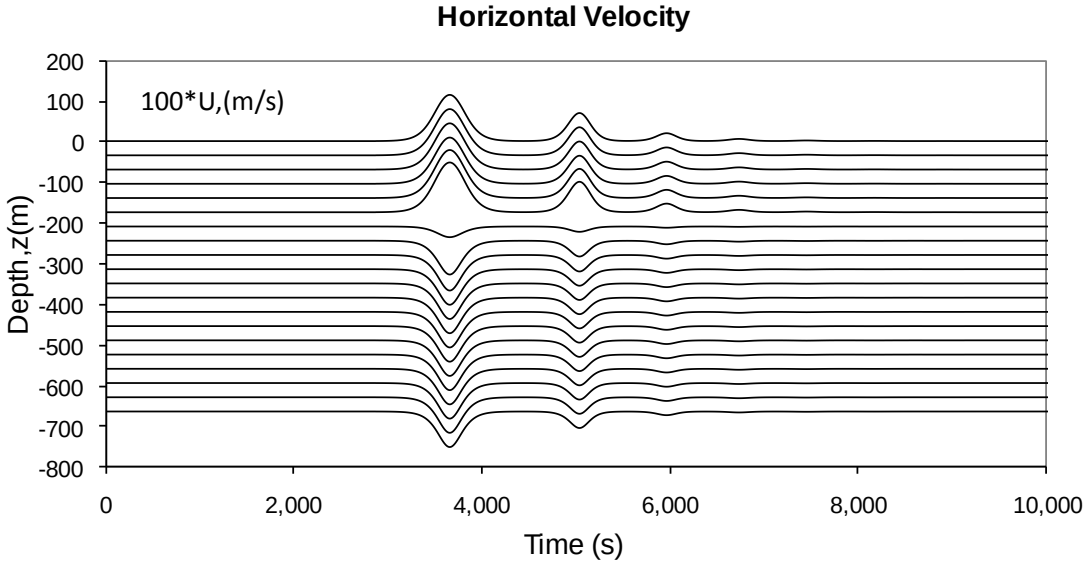

Figure 4.4 Horizontal Velocity Distribution with Depth (η=90m)

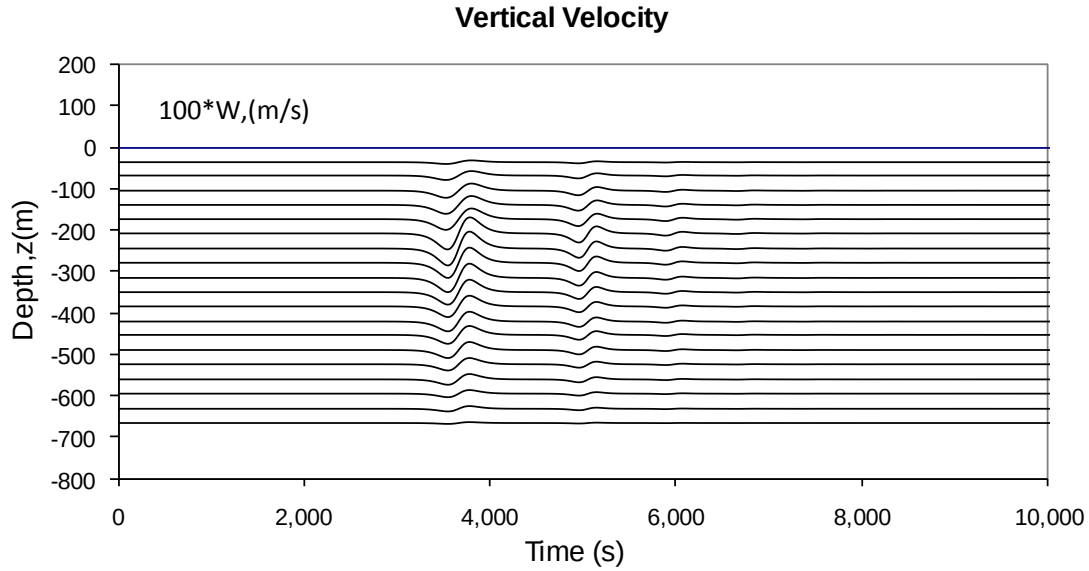

Figure 4.5 Vertical Velocity Distribution with Depth (η=90m)

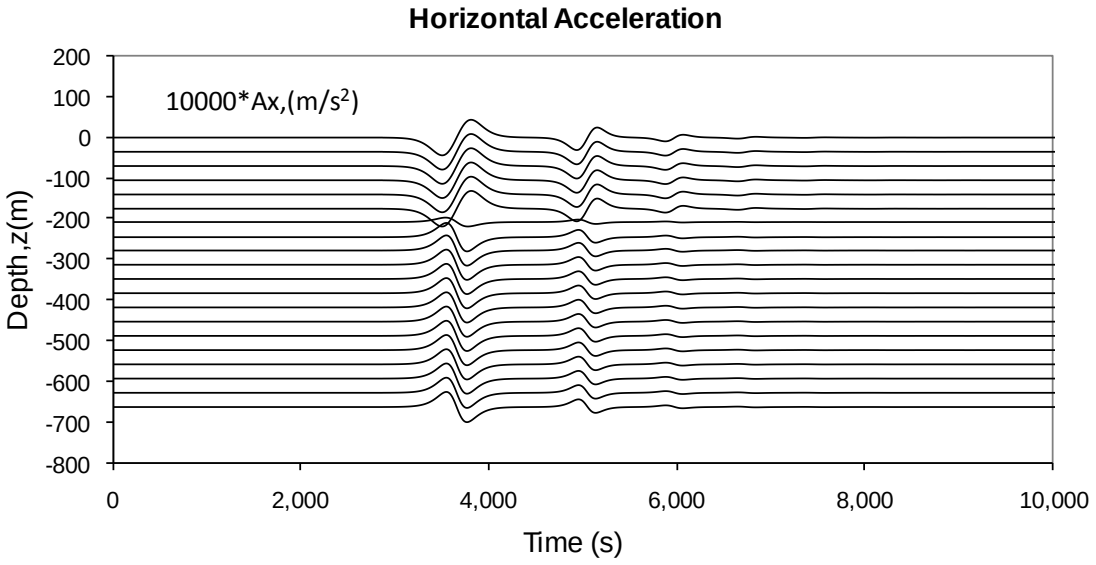

Figure 4.6 Horizontal Acceleration Distribution with Depth (η=90m)

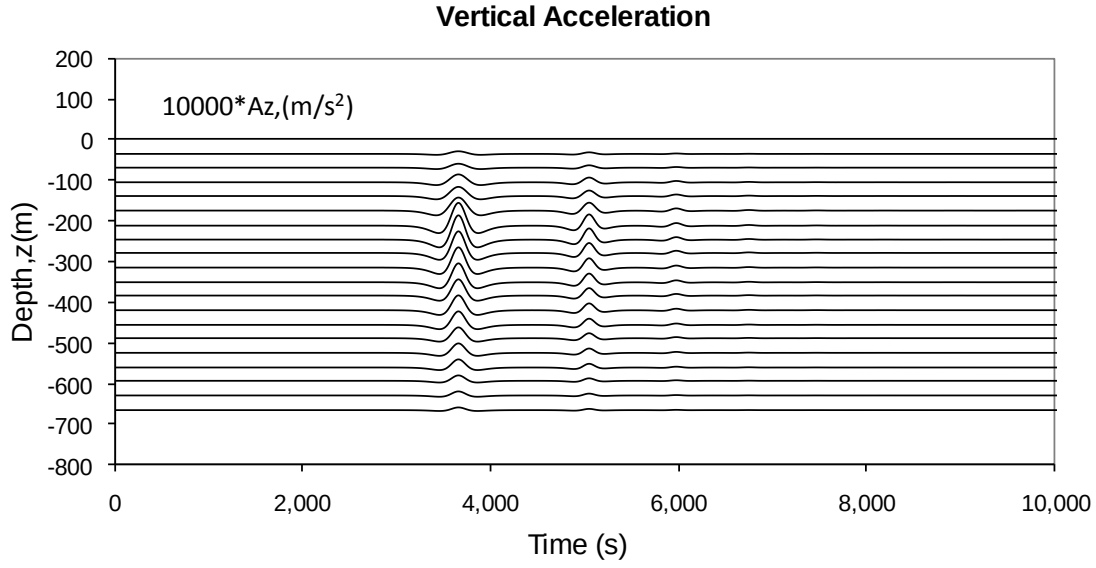

Figure 4.7 Vertical Acceleration Distribution with Depth (η=90m)

4.3. Description of Semisubmersible Drilling System

The CNOOC HaiYangShiYou 981, a 6th generation DP3 deepwater drilling semisubmersible rig is used in this study. This semi is CNOOC's most recently completed deepwater drilling semi and is designed to be used for the South China Sea development. It's length, breadth, and depth are 114.07m, 78.68m, and 112.30m respectively. This drilling unit is capable of drilling up to 10,000 meters in water depths of up to 3050 meters.

HaiYangShiYou 981 has four (4) groups of chain-polyester-chain mooring lines. Figure 4.8 shows the mooring system configuration at an operating depth of 700m. The properties of its moorings and drilling riser for this study are summarized in Tables 4.3 and 4.4. The drilling riser top tensioner stiffness is 438.09 KN/m.

Table 4.4 Drilling Semi Mooring Line Properties

Mooring Line Properties	Diameter (mm)	EA (t)	Breaking Strength (t)	Wet Weight (kg/m)	Length (m)
Chain	84	620340	815.2	134	300
Polyester	160	156800	828.0	4.2	1250
Chain	90	711480	815.2	156.2	1000

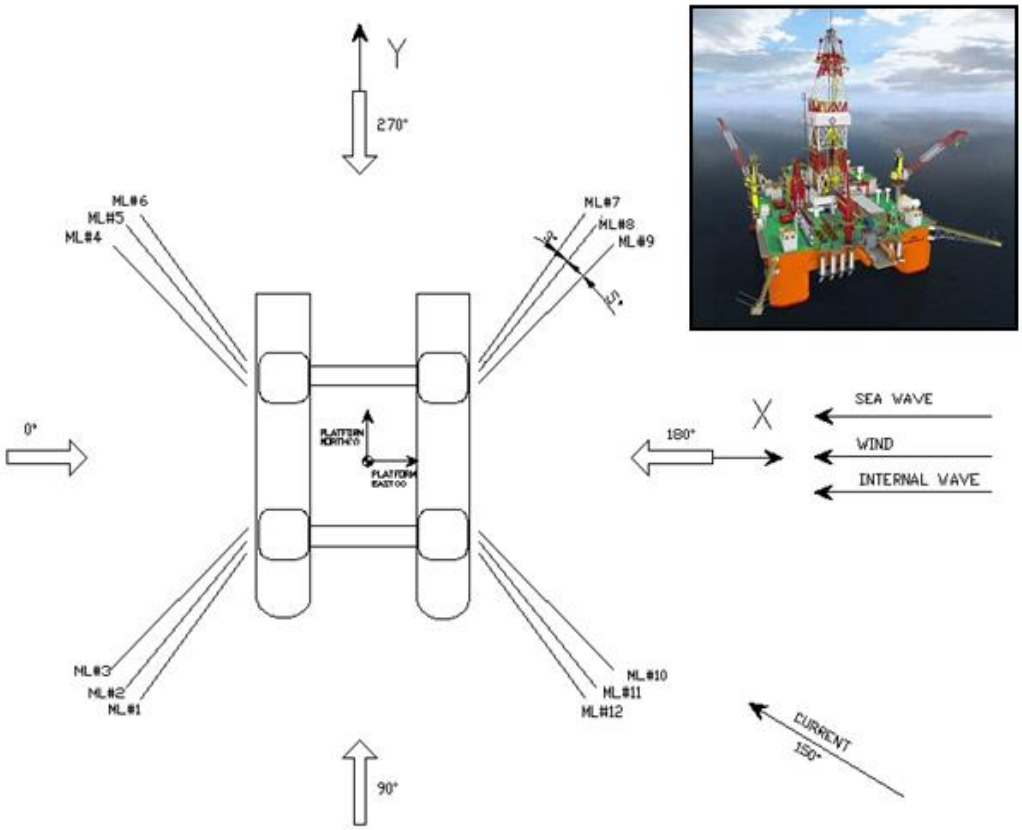

Figure 4.8 Hai Yang Shi You 981 Configuration and Mooring Layout

Table 4.5 Drilling Riser Properties

Drilling Riser Properties	Diameter (mm)	EA (KN)	EI (KN-m^2)	Dry Weight (kg/m)	Wet Weight (kg/m)	Length (m)
Bare Riser	533.4	7382000	241600	784.44	559.17	510
Riser with Buoyancy Module	1379	7382000	241600	1086.35	25.86	200

4.4. Coupled Analysis Modeling

Coupled hull hydrodynamics, mooring and riser program HARP is modified for this analysis. The hydrodynamic panel model used by the wave diffraction and radiation program WAMIT is presented in Figure 4.9.

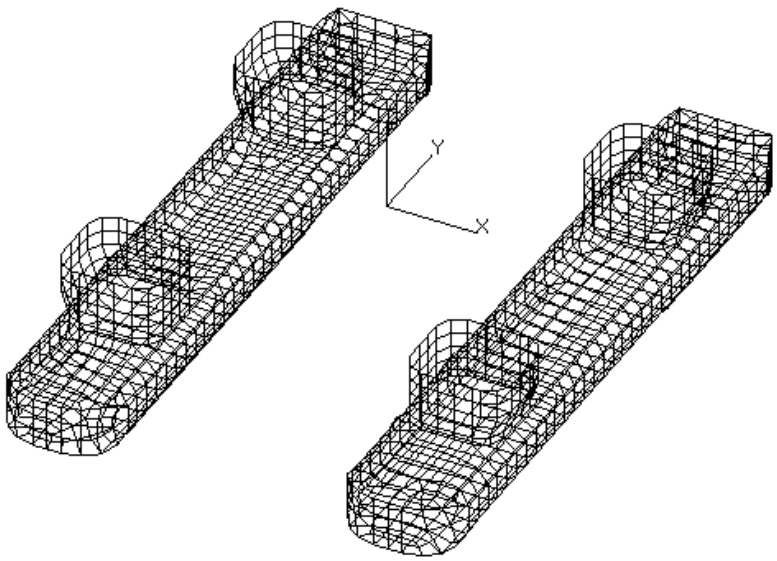

Figure 4.9 Hai Yang Shi You 981 Drilling Semi Hydrodynamics Panel Model

The coupled analysis model including the drilling semi hull, mooring lines and a drilling riser is shown in Figure 4.10. The drilling riser is connected to the semi hull using springs to represent the riser tensioners with corresponding stiffness. The portions of the mooring chain on the seabed are modeled with contact springs to simulate the soil stiffness and drag.

The internal wave forces are applied to the platform hull and mooring lines and risers using Morison Equations based on the water particle velocities and accelerations

obtained from equation (18) utilizing the continuity equation and the nonlinear kinematic boundary conditions. This approach is adequate due to the long period nature of the internal wave. The Morison members of the Semi hull are shown in Figure 4.10.

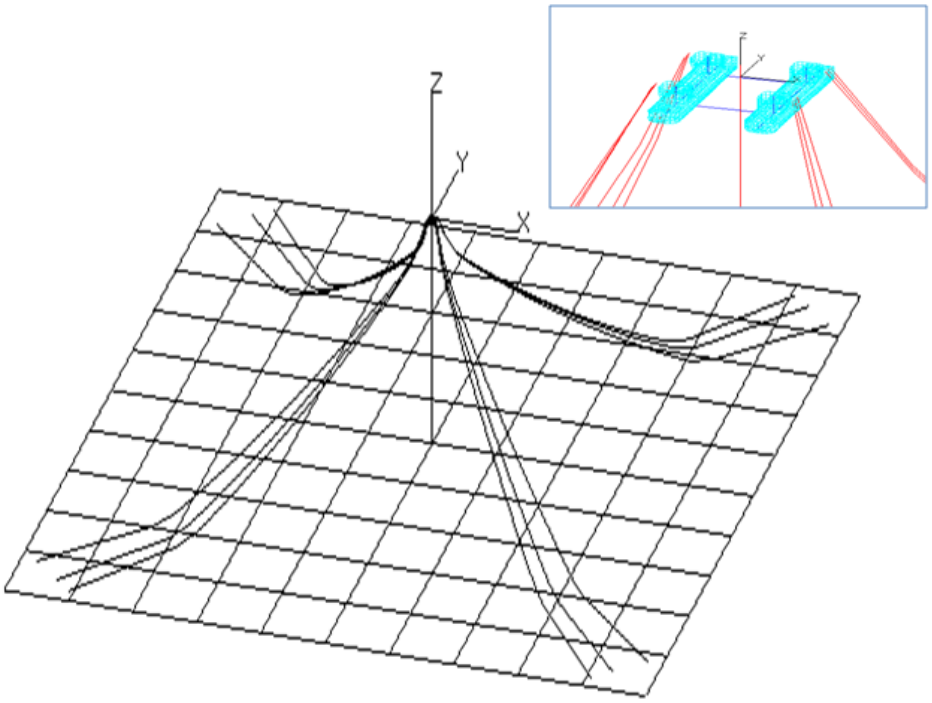

Figure 4.10 Coupled Analysis Model with Program HARP

Figure 4.11 shows the internal wave initial setup relative the drilling semi coupled model. The front of the internal wave at the beginning of simulation is 1000m away from the platform origin. The structure function (W(z)) which represents the distribution of the internal wave along the water depth is also shown in the same figure.

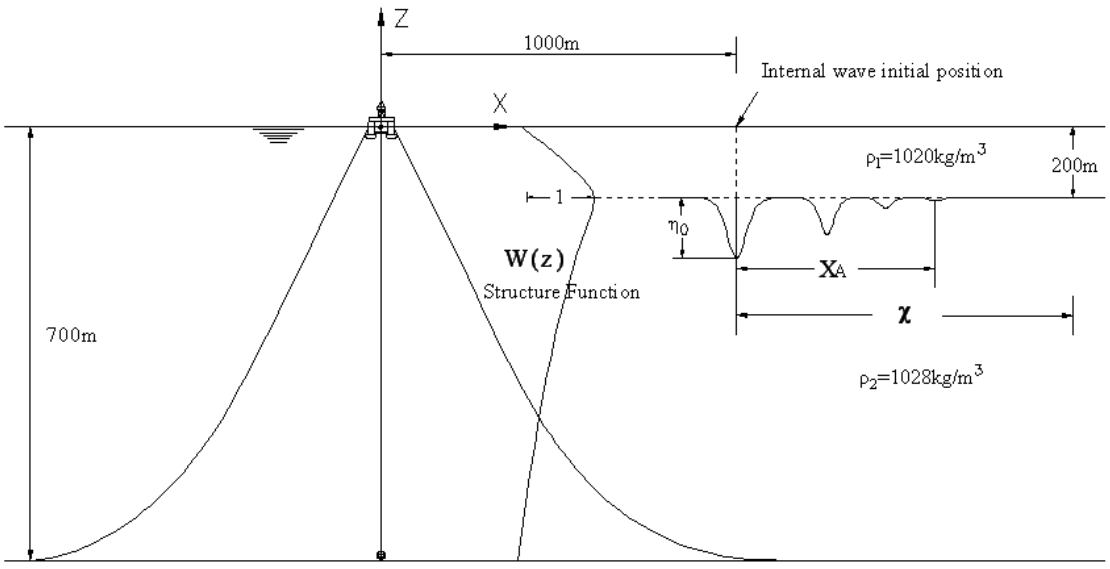

Figure 4.11 Drilling Semi and Internal Wave Setup at Beginning of Simulation

4.5. Analysis Results

Three-hour time domain dynamic analyses are performed for both internal wave heights of 90m and 170m. The operating and survival conditions are also analyzed without the presence of internal waves for comparison. Drilling semi motions and the top tension time histories of the mooring line (#10) subject to the highest loads for the 90m height internal wave are shown in Figures 4.12 to 4.16. The motion statistics and the maximum mooring line tension with corresponding utilization ratios are summarized in Table 4.5 and 4.6 respectively.

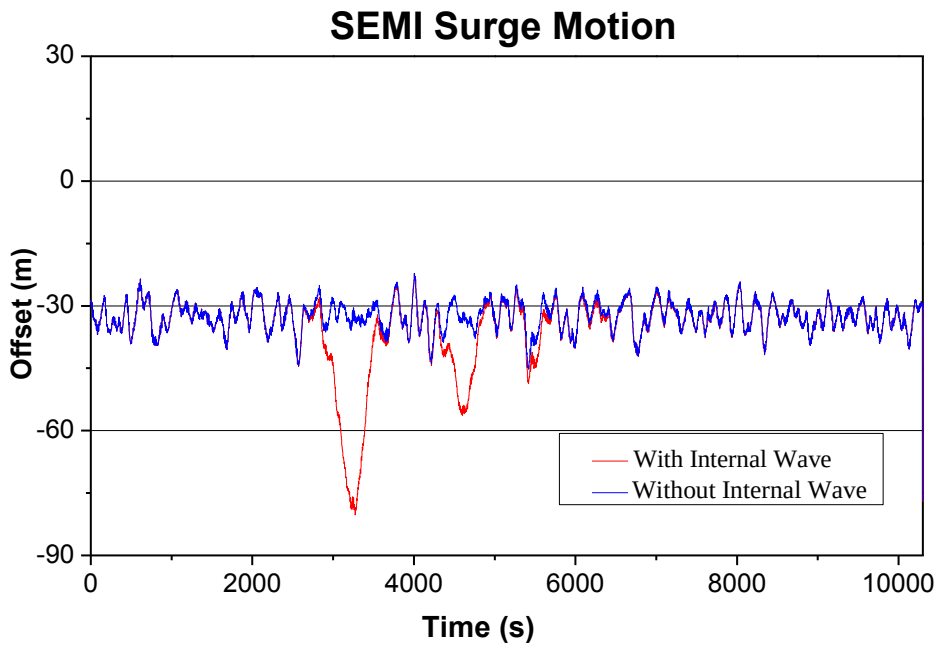

Figure 4.12 Drilling Semi Surge Motion Time History (η=90m)

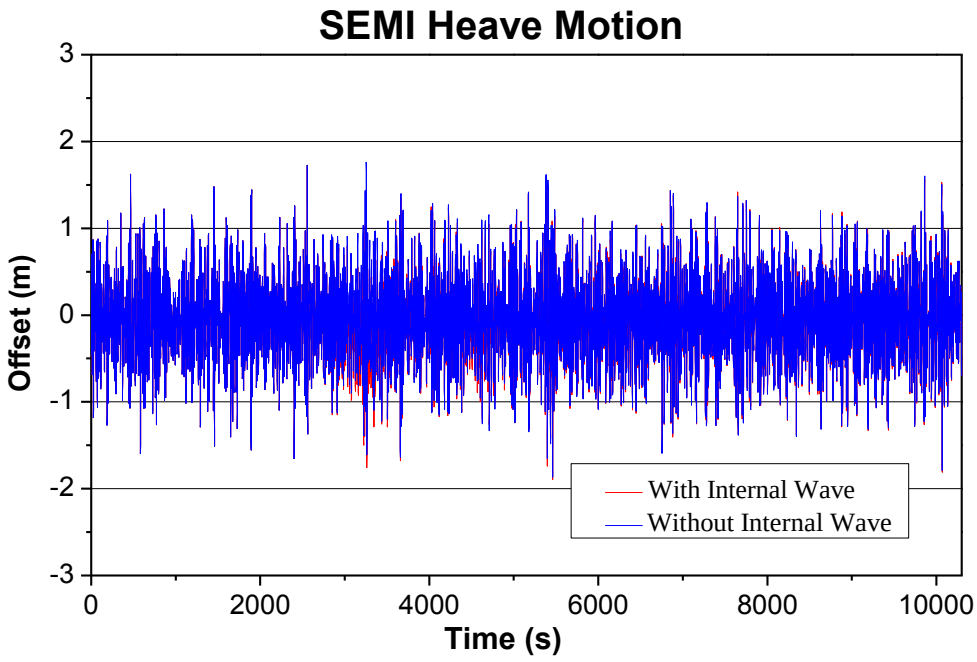

Figure 4.13 Drilling Semi Heave Motion Time History (η=90m)

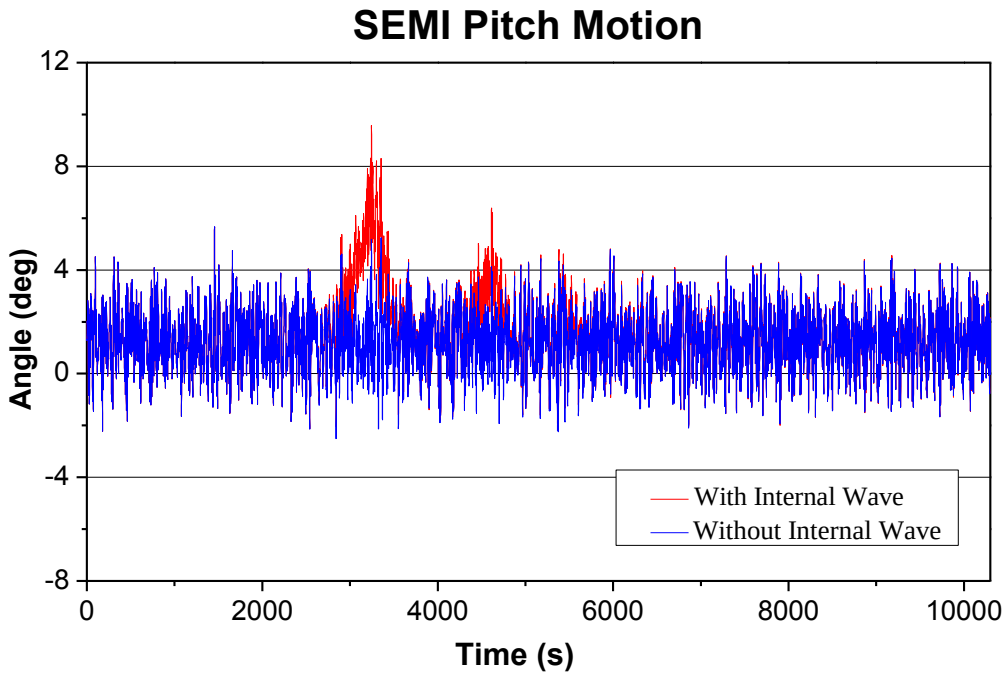

Figure 4.14 Drilling Semi Pitch Motion Time History (η=90m)

Table 4.6 Drilling Semi Motion Statistics

Condition			Operation	Operation	Operation	Survival
Internal Wave Height			N/A	90m	170m	N/A
Offset	MAX	m	-22.23	-22.31	-22.55	-61.86
	MIN	m	-44.98	-79.84	-109.77	-103.2
	MEAN	m	-32.38	-34.93	-36.19	-80.26
Heave	MAX	m	1.76	1.72	1.83	4.37
	MIN	m	-1.87	-1.89	-1.92	-4.73
	MEAN	m	-0.04	-0.06	-0.07	-0.29
Pitch	MAX	deg	5.66	9.57	11.86	12.63
	MIN	deg	-2.51	-2.22	-2.26	-5.13
	MEAN	deg	1.26	1.55	1.67	2.89

From Table 4.5 it is seen that the mean offset during the operation condition with no internal wave applied is 32.38 m. Subtracting this from the maximum absolute offset

(79.84 m) for the operating condition with 90 m internal wave we can gauge that an offset of 47.46m is caused solely by the effect of the internal wave. Similarly it is seen that the internal wave of 170 m causes an offset of 77.39 m. The offset from the 170m internal wave is close to the offset observed by the Liuhua project drilling semi in South China Sea.

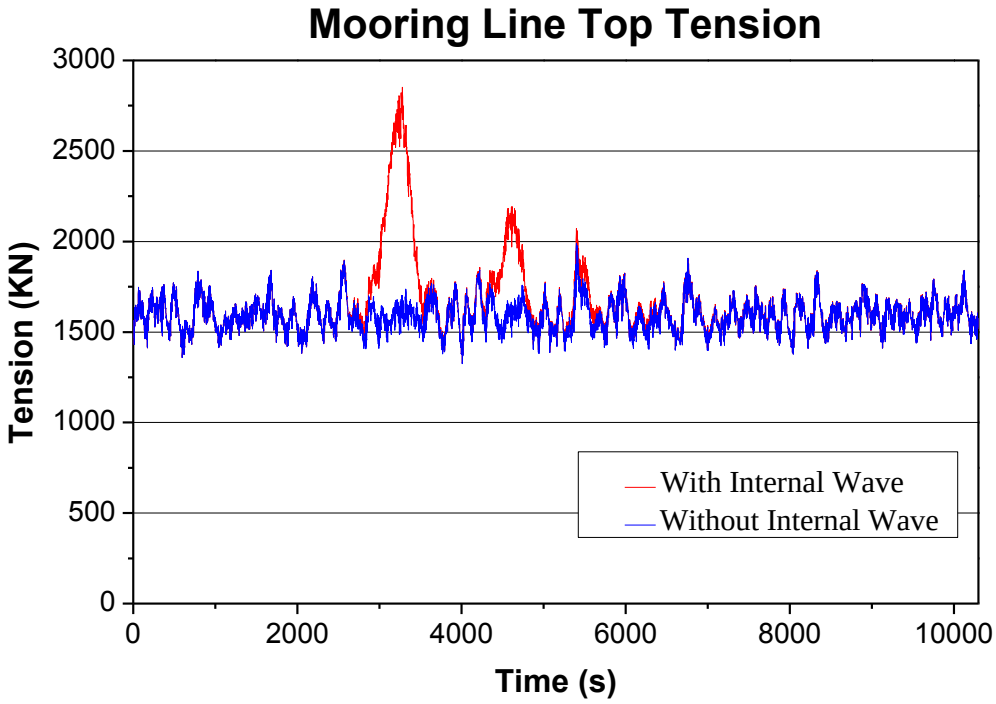

Figure 4.15 Drilling Semi Mooring Line #10 Top Tension Time History (η=90m)

Table 4.7 Mooring Line Max Tension and Utilization Ratio

Condition		Operation	Operation	Operation	Survival
Internal Wave Height		N/A	90m	170m	N/A
Line Max tension	KN	1.99E+03	2.85E+03	3.68E+03	3.88E+03
Utilization Ratio	N/A	0.24	0.34	0.44	0.47

The maximum mooring line tension and utilization satisfy the API mooring design code requirement for all four conditions.

The drilling riser tension and bending moment at the location above the bottom BOP (Blow-Out Preventer) stack are calculated. The time history of the bottom tension and moment for the 90m internal wave height are shown in Figure 4.17. Tables 4.7 and Table 4.8 summarize the maximum and mean values for four different conditions. The calculation of the survival condition is for the comparison purpose. It is recommended that the drill riser be disconnected in a real situation unless it is special designed to be connected in survival condition. Drilling riser bending moments are shown in Table 4.9.

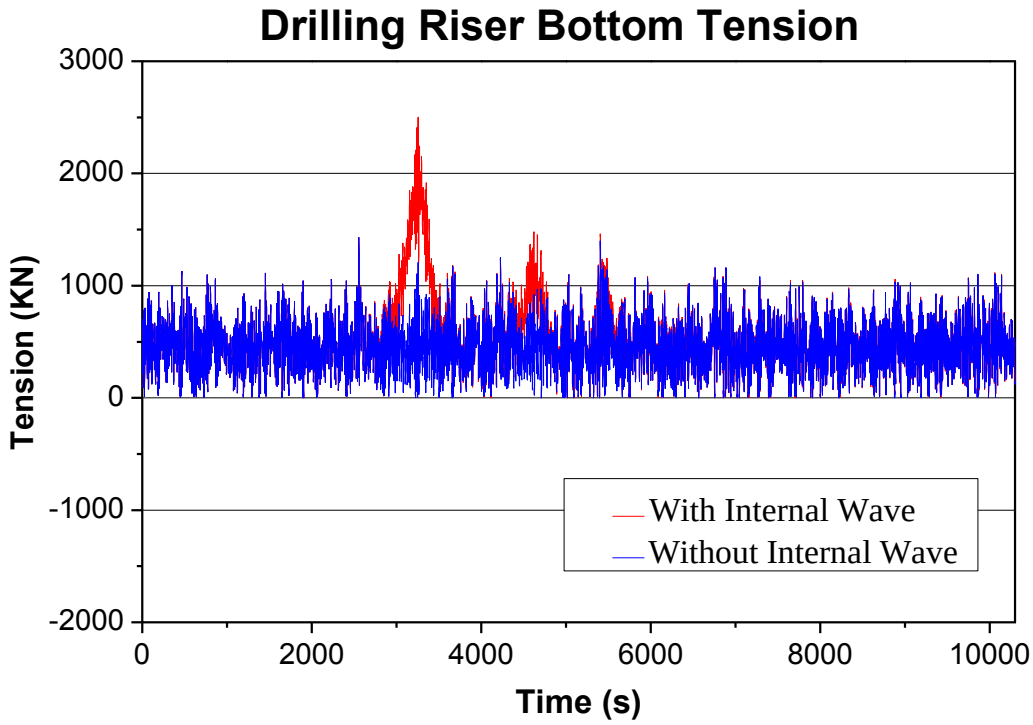

Figure 4.16 Drilling Riser Bottom Tension Time History (η=90m)

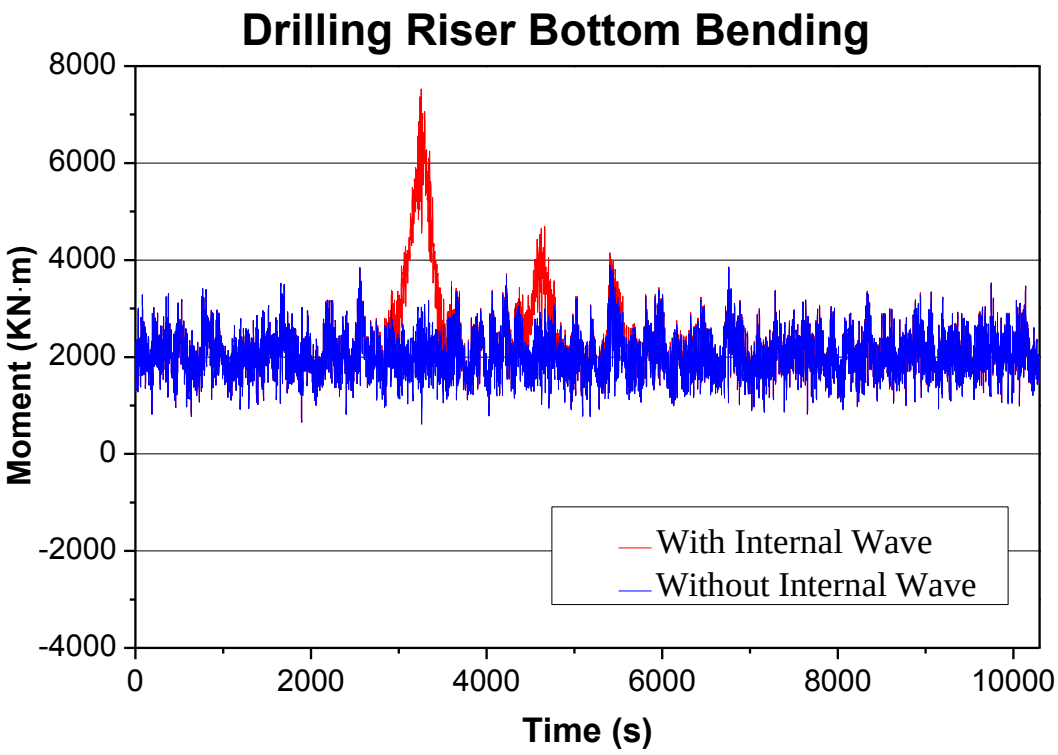

Figure 4.17 Drilling Riser Bottom Bending Moment Time History (η=90m)

Table 4.8 Drilling Riser Tension at Bottom BOP

Condition		Operation	Operation	Operation	Survival
Internal Wave Height		N/A	90m	170m	N/A
MAX	KN	1.39E+03	2.46E+03	3.61E+03	4.33E+03
MEAN	KN	4.06E+02	4.68E+02	5.16E+02	1.95E+03

Table 4.9 Drilling Riser Bending Moment at Bottom BOP

Condition		Operation	Operation	Operation	Survival
Internal Wave Height		N/A	90m	170m	N/A
MAX	KN·m	3.91E+03	7.54E+03	1.14E+04	1.38E+04
MEAN	KN·m	2.02E+03	2.21E+03	2.30E+03	6.85E+03

Significant bending moments and relative large tensions caused by internal waves are observed. These could directly result drilling riser failure at the bottom connection above BOP, when the internal wave is combined with the 1-year design wave condition.

4.6. Summary

The internal wave model presented in this study could provide relatively realistic representation of shallow internal waves observed in South China Sea. The analysis method is feasible for modeling internal wave in offshore engineering project applications. The methodology can be extended to finite depth and deep water formulations with varying pycnocline (Barr and Johnson ; Chou et al. ; Paulling ; Paulling 1980; Sarpkaya 2004) for a more accurate assessment of the effects of internal waves on offshore platforms and a future paper will address these concerns.

Analysis results are similar to offshore observations. The internal wave impact on platform motions and mooring/riser strength can be analyzed separately and

superimposed to the wind wave analysis results. This is clearly due to the long period nature of internal waves.

It is seen that internal waves have a considerable impact on deep water drilling risers where overstress or even failure may result at the bottom connection to BOP due to the large bending caused by the platform offset.

It is recommended that the drilling riser mooring system designed for survival environmental conditions should have compatible strength for internal waves.

5. APPLICATION II: NONLINEAR INTERNAL WAVES IMPACT ON DIFFERENT TYPE OF FLOATING PRODUCTION SYSTEMS IN SOUTH CHINA SEA

5.1. Environmental Parameters

The environment considered in this study is based on a realistic floating platform design operation/survival conditions and internal waves observed in South China Sea.

5.1.1. Field Description

The South China Sea Liwan 3-1 field, a large gas reservoir with potential reserves of 6Tcf was discovered in 2006. The field is situated on Block 29/26 approximately 350 km SE of Hong Kong and spans 979,773 acres (3,965 square kilometers). In this study, it is assumed that the site water depth is 1219m (4000ft) and the pycnocline is at 200 m below the surface.

5.1.2. Surface Wave, Wind and Current

The summary of regular environmental conditions applied in the analysis is presented in Table 5.1. These correspond to waves with return period of 100-year and 1-year respectively.

Table 5.1 Summary of Environmental Conditions

Items	South China Sea Water Depth = 1219.2 m					
	1		2		3	
	100-Year Typhoon				1-Year Return Period Criteria	
	Wave Dominant		Wind Dominant			
	Design Extreme		Design Extreme		Normal Operating	
Wave	Jonswap		Jonswap		Jonswap	
Gamma	2.4		2.4		1	
Wave Direction(deg)	180		180		180	
Significant (Hs)(m)	15.24		14		6	
Spectral Peak Period (Tp)(s)	15.6		15.1		11.2	
Wind	API		API		API	
1-Hour Avg. Wind (m/s)	42.98		45		21.97	
Wind Direction (deg)	180		180		180	
Current Profile	Normal		Normal		Normal	
	Depth	Vel	Depth	Vel	Depth	Vel
	(m)	(m/s)	(m)	(m/s)	(m)	(m/s)
	0	1.91	0	2	0	1.02
	-36.88	1.4	-36.88	1.47	-50	0.77
	-75	0.19	-75	0.19	-100	0.27
	-1219.2	0.19	-1219.2	0.19	-1219.2	0.13
Current Direction (deg)	180		180		180	

5.1.3. Internal Wave

The same internal wave model presented in the previous chapter is also applied in this chapter's analysis. Two sets of internal waves, summarized in Table 5.2, are generated for the analysis. The 90 m wave is considered to an intermediate internal wave in the South China Sea while the 170 m wave corresponds to an extreme wave.

Table 5.2 Internal Wave Input Parameters

Parameters	Unit	Case 1	Case 2
Internal Wave Height	m	90	170
Upper Layer Depth	m	200	200
Upper Layer Fluid Density	kg/m^3	1020	1020
Lower Layer Depth	m	1019.2	1019.2
Lower Layer Fluid Density	kg/m^3	1028	1028
Internal Wave Pre-existing Time T_0	sec	30000	10000
Recovery Function Power (A)	-	4	4
Error Function β	-	3.0	3.0
Error Function φ	-	-0.1	-0.1

5.2. Coupled Analysis and Modeling

Three sets of production platforms including a Spar, Semi and TLP designed for the same field with compatible process capability are used in the study. The coupled analysis model includes the platform hull, mooring lines and risers. The moorings and risers are connected to the Spar hull using springs with corresponding stiffness. The portions of the mooring chain and SCR on the seabed are modeled with contact springs to simulate the soil stiffness and drag. Figure 5.1 demonstrates the internal wave initial setup relative to the platforms coupled analysis model. The front of the internal wave at the beginning of simulation is 1000m away from the platform origin. The structure function W(z) which represents the distribution of the internal wave along the water depth is also shown in the same figure.

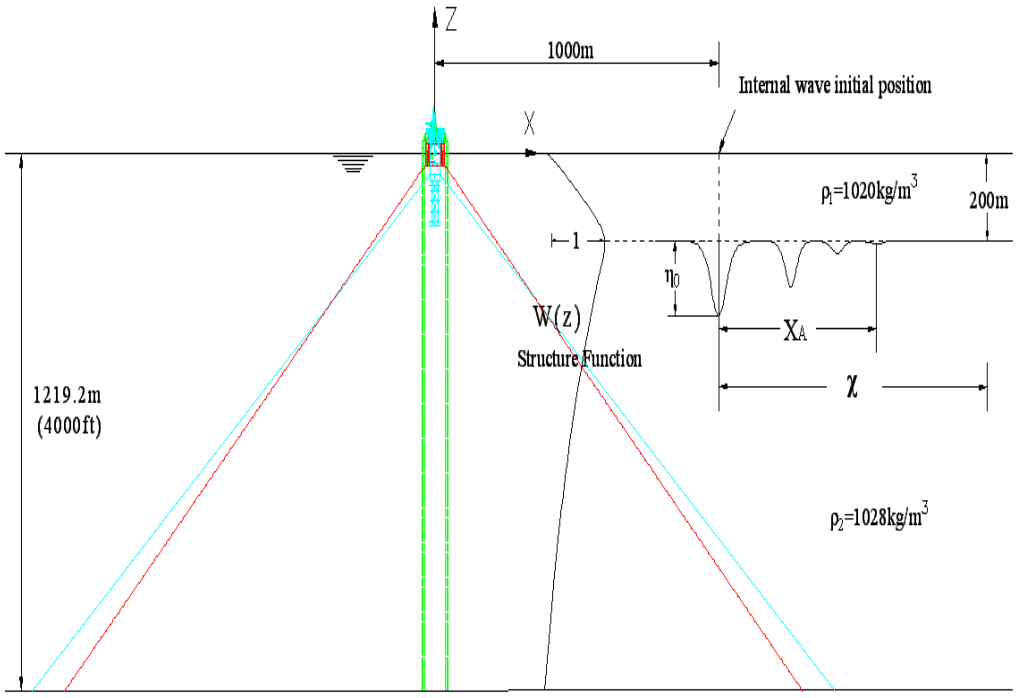

Figure 5.1 Spar, Semi, and TLP Coupled Analysis Models and Internal Wave Initial Setup

5.3. Spar Production System

5.3.1. Spar Description

The production Spar key figures are summarized in Table 5.3 below:

Table 5.3 Spar Key Figures

Draft	m	164.59
Displacement (including entrapped water)	N	8.69×10^{8}
Total Weight (including entrapped water)	N	7.73×10^{8}
Hard Tank Diameter	m	37.19
Hard Tank Height above MWL	m	16.76
Hard Tank Height below MWL	m	63.09
Center Well Dimension	m	10.97×10.97
Main Truss Member Length	m	97.49
Heave Plate Dimension	m	37.19×37.19
Heave Plate Height	m	1.0
Number of Heave Plates	-	3
Soft Tank Dimension	m	37.19×37.19
Soft Tank Height	m	6.1
Vertical C.G. from Base KG	m	98.66
Vertical C.B. from Base KB	m	109.0
Pitch Radii of Gyration Rxx	m	77.12
Roll Radii of Gyration Ryy	m	77.27
Yaw Radii of Gyration Rzz	m	14.63

The Spar configuration and the mooring line properties are shown in Figure 5.2 and Table 5.5 respectively. Spar mooring line properties are shown in Table 5.4.

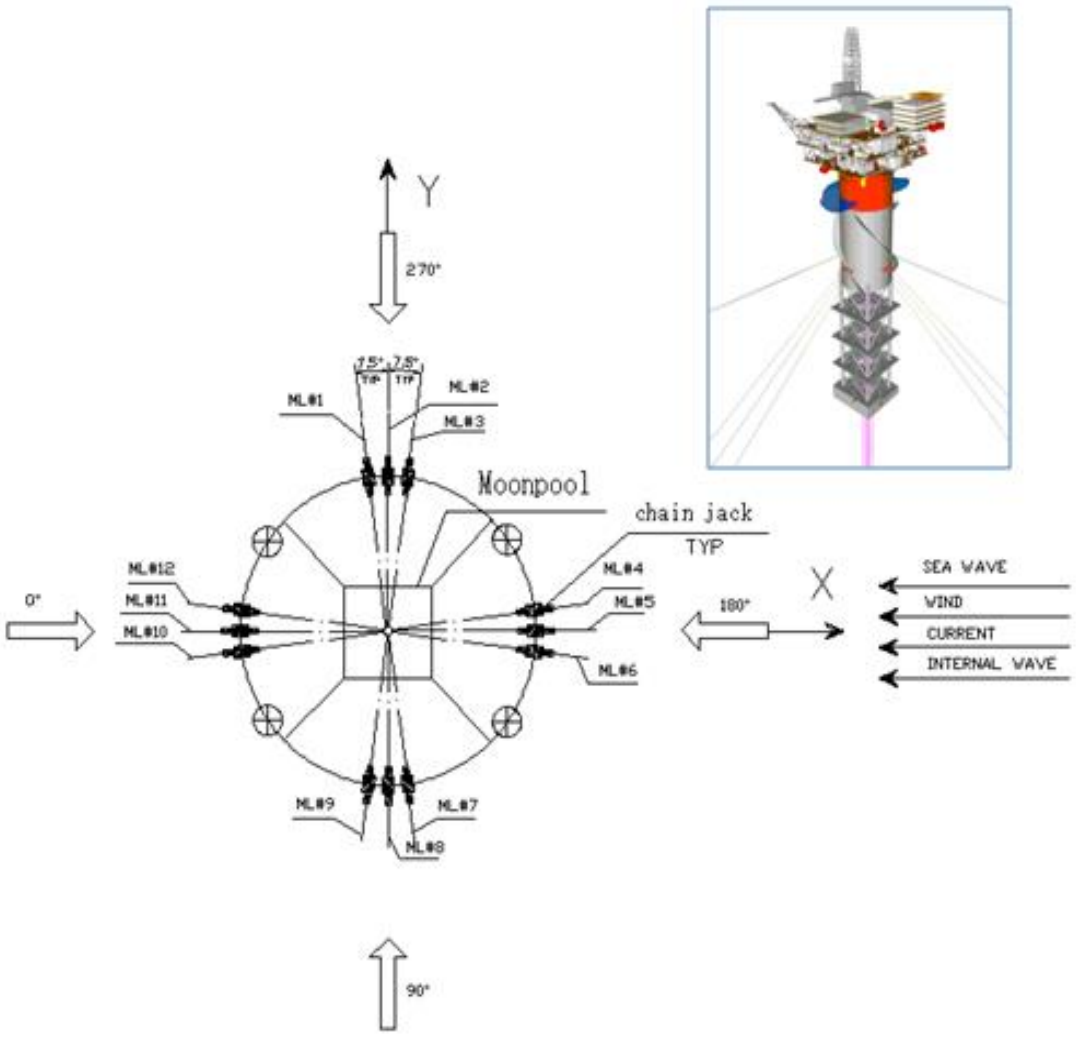

Figure 5.2 Spar configuration

Table 5.4 Spar Mooring Line Properties

Mooring Line Properties	Diameter (m)	EA (KN)	Breaking Strength (KN)	Wet Weight (kg/m)	Dry Weight (kg/m)	Length (m)
Chain	0.1334	2.06×10^6	15746	303.39	355.62	121.9
Polyester	0.22	4.10×10^5	14168	8.53	32.72	1388.4
Chain	0.1334	2.06×10^6	15746	309.39	355.62	304.8

The Spar coupled analysis model and the hydrodynamic panel model used by the wave diffraction and radiation program WAMIT are presented in Figure 5.3. The analysis model also includes 8 production TTRs (Top-Tensioned Risers), 1 drilling riser, 2 import SCRs (Steel Catenary Risers), and 2 export SCRs.

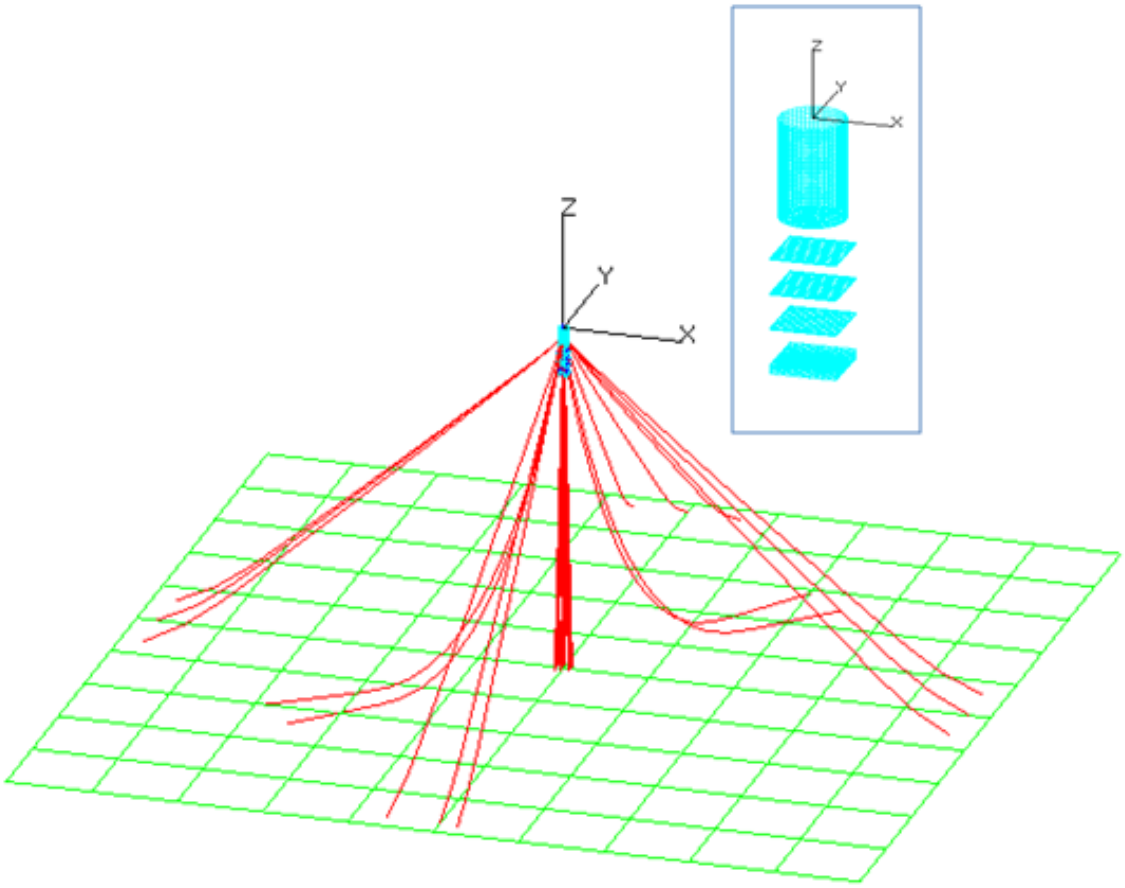

Figure 5.3 Spar Coupled Analysis Model with Program HARP

5.3.2. Spar Analysis and Results

Three-hour time domain dynamic analyses are performed for both internal wave heights of 90m and 170m. The operation and survival conditions are also analyzed

without the presence of internal waves for comparison. The Spar motions and the top tension time histories of the mooring line (#5) subject to the highest loads for the 170m height internal wave are shown in Figures 5.4 to 5.7. The motion statistics and the maximum mooring line tension with corresponding utilization ratios are summarized in Tables 5.6 and 5.7 respectively.

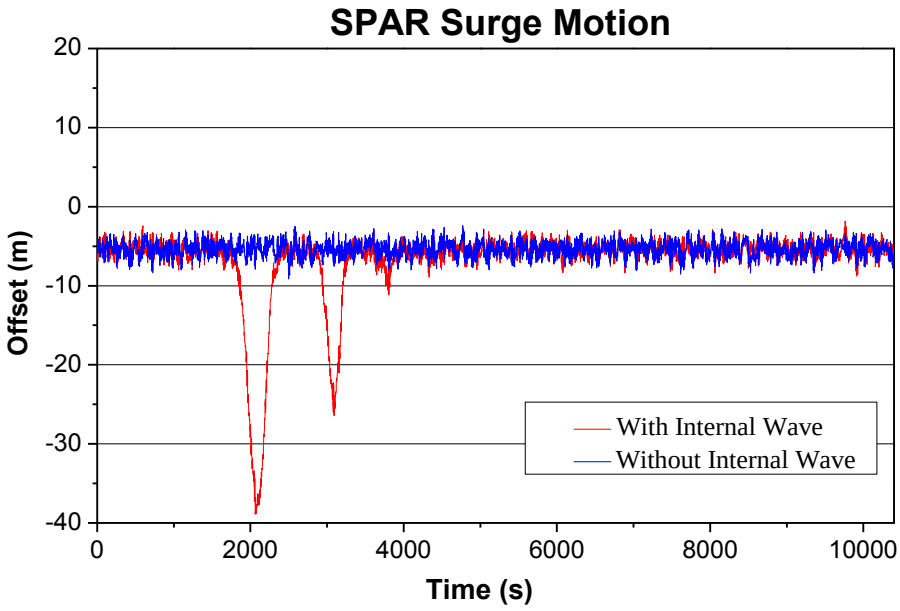

Figure 5.4 Spar Surge Motion Time History (η=170m)

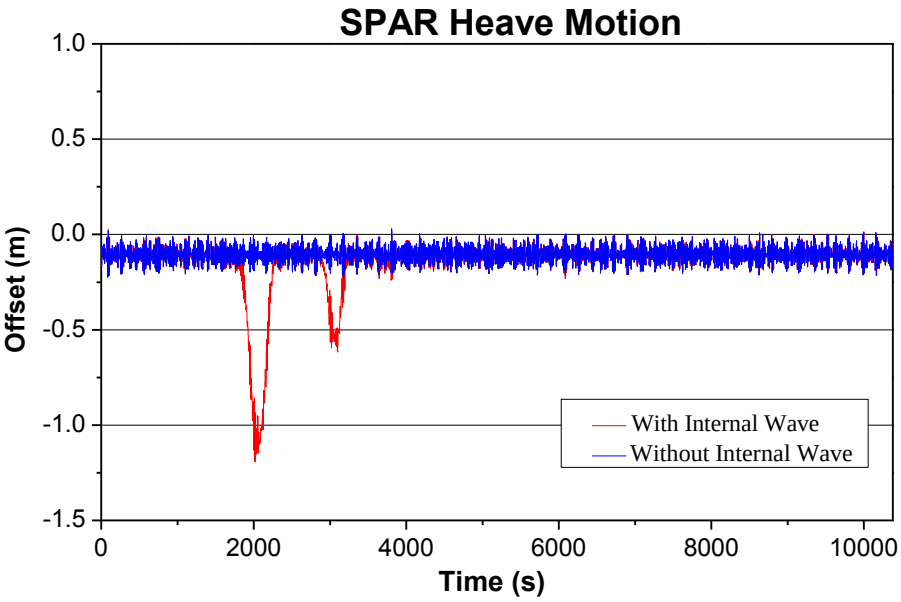

Figure 5.5 Spar Heave Motion Time History (η=170m)

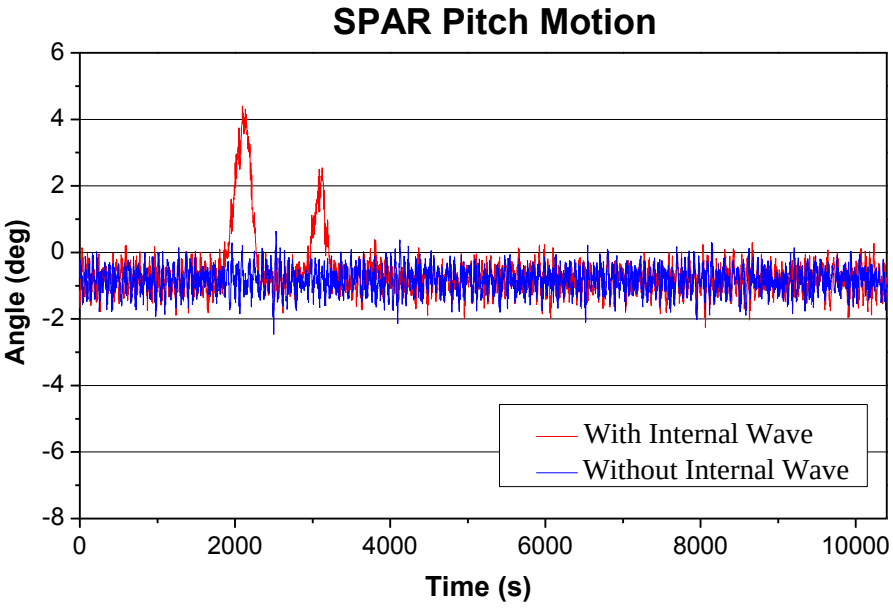

Figure 5.6 Spar Pitch Motion Time History (η=170m)

Table 5.5 Spar Motion Statistics

Condition			Operation			Survival	
						Wave Dominant	Wind Dominant
Internal Wave Height			N/A	90m	170m	N/A	N/A
Offset	MAX	m	-2.42	-2.48	-1.77	-5.59	-7.11
	MIN	m	-9.13	-21.29	-39.05	-29.32	-29.69
	MEAN	m	-5.38	-6.17	-6.56	-15.33	-16.36
Heave	MAX	m	0.03	0.03	0.01	1.88	1.46
	MIN	m	-0.23	-0.51	-1.18	-2.23	-1.90
	MEAN	m	-0.11	-0.12	-0.14	-0.21	-0.23
Pitch	MAX	deg	0.63	2.24	4.38	1.04	0.91
	MIN	deg	-2.46	-2.46	-2.20	-6.86	-6.92
	MEAN	deg	0.36	-0.73	-0.65	-2.48	-2.68

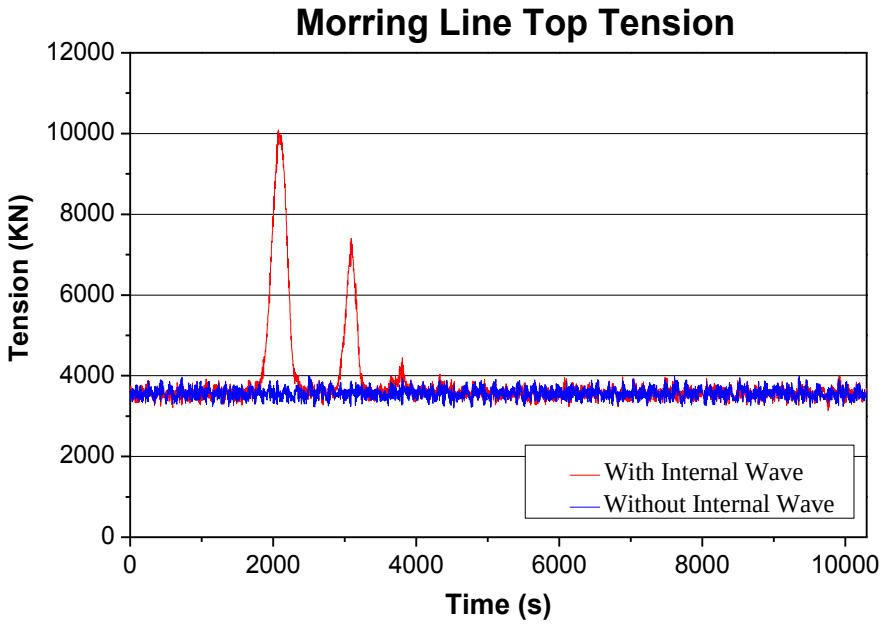

Figure 5.7 Spar Mooring Line #5 Top Tension Time History (η=170m)

Table 5.6 Spar Mooring Line #5 Max Tension and Utilization Ratio

Condition		Operation			Survival	
					Wave Dominant	Wind Dominant
Internal Wave Height		N/A	90m	170m	N/A	N/A
Line Max Tension	KN	4.00E+03	6.37E+03	1.01E+04	7.51E+03	7.52E+03
Utilization	-	0.28	0.45	0.71	0.53	0.53

5.4. Semi Production System

5.4.1. Semi Description

The production Semi key figures are summarized in Table 5.7 below:

Table 5.7 Semi Key Figures

Draft	m	28.96
Displacement	N	3.09×10^{8}
Hull Total	kg	2.70×10^{7}
Column Height	m	47.85
Column Side Length	m	12.5
Column c/c Span	m	56.39
Pontoon Width	m	10.67
Pontoon Height	m	6.71
Vertical C.G. from Base KG	m	23.87
Vertical C.B. from Base KB	m	9.92
Pitch Radii of Gyration Rxx	m	32.61
Raw Radii of Gyration Ryy	m	31.94
Yaw Radii of Gyration Rzz	m	29.32

The Semi configuration and the mooring line properties are shown in Figure 5.8 and Table 5.8 respectively.

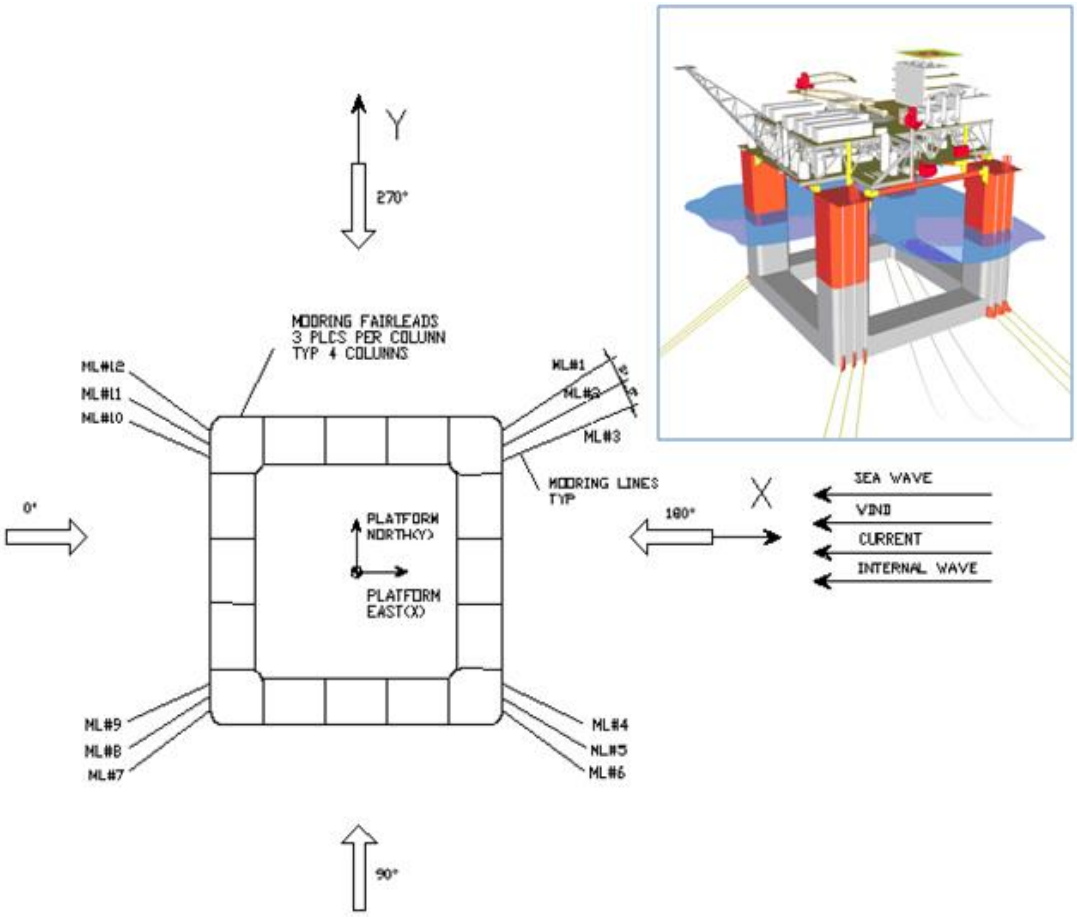

Figure 5.8 Semi Configuration and Mooring Layout

Table 5.8 Semi Mooring Line Properties

Mooring Line Properties	Diameter (m)	EA (KN)	Breaking Strength (KN)	Wet Weight (kg/m)	Dry Weight (kg/m)	Length (m)
Chain	0.1302	1.95×10^6	15118	292.87	336.77	106.7
Polyester	0.22	4.10×10^5	14168	8.53	32.72	1676
Chain	0.1302	1.96×10^6	15118	292.87	366.77	250

The Semi coupled analysis model and the hydrodynamic panel model are presented in Figure 5.9. The analysis model also includes 2 import SCRs, and 2 export SCRs.

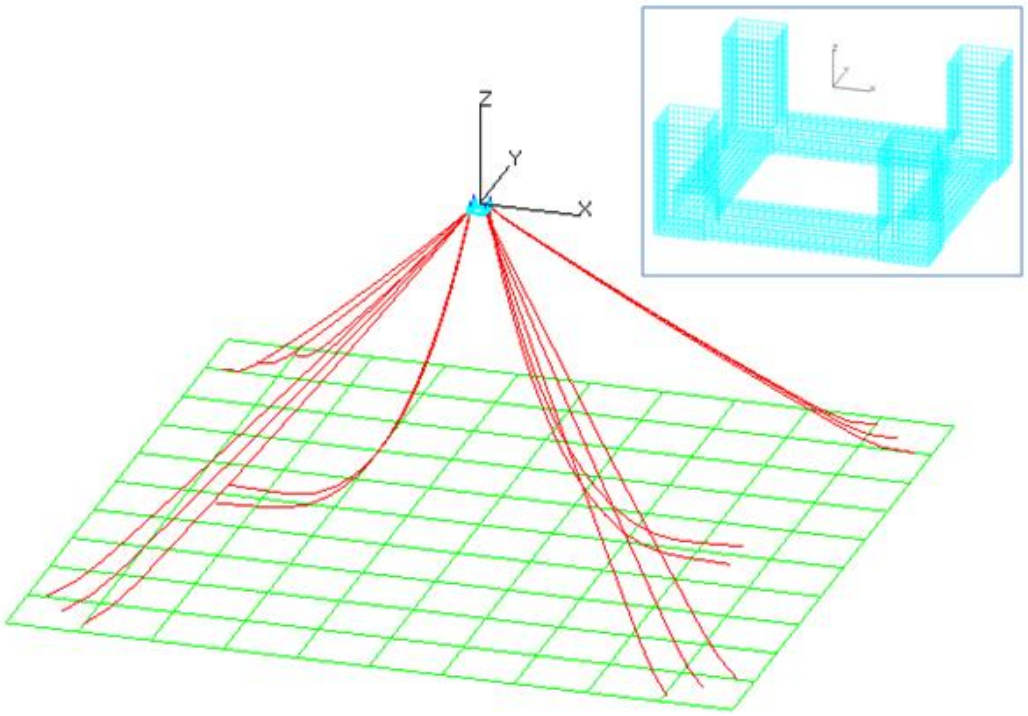

Figure 5.9 Semi Coupled Analysis Model with Program HARP

5.4.2. Semi Analysis and Results

Three-hour time domain dynamic analyses are performed for the same conditions of the Spar case. The Semi motions and the top tension time histories of the mooring line (#3) subject to the highest loads for the 170m height internal wave are shown in Figure 5.10 to Figure 5.13. The motion statistics and the maximum mooring line tension with corresponding utilization ratios are summarized in Table 5.9 and 5.10 respectively.

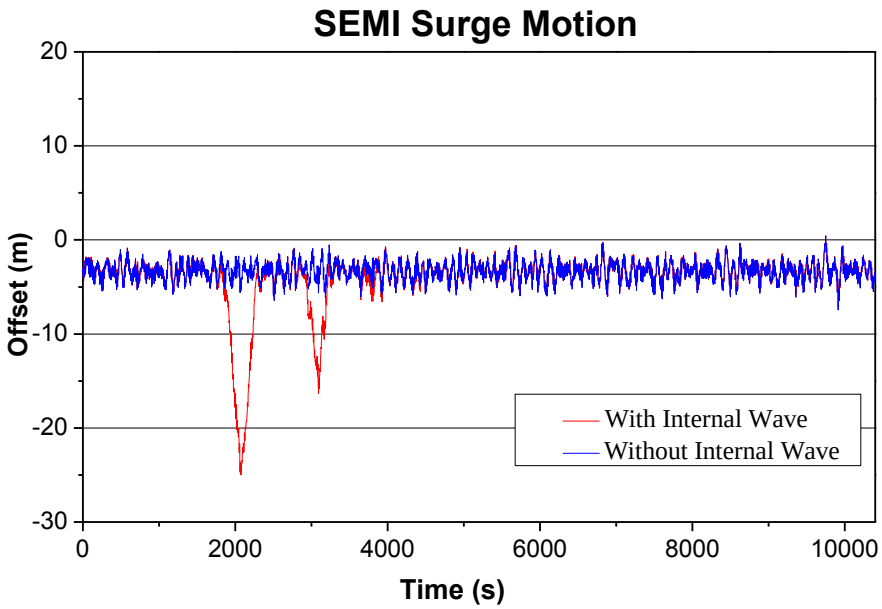

Figure 5.10 Semi Surge Motion Time History (η=170m)

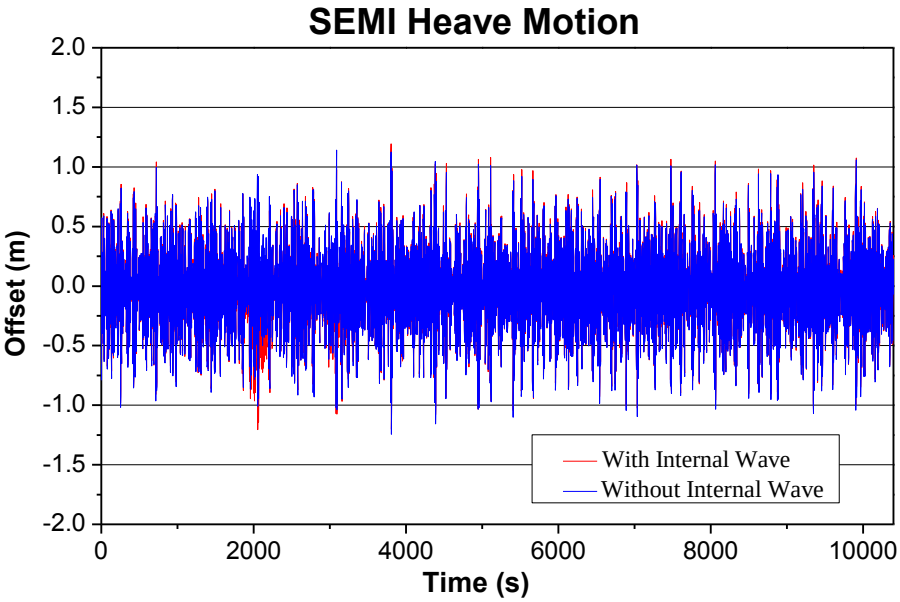

Figure 5.11 Semi Heave Motion Time History (η=170m)

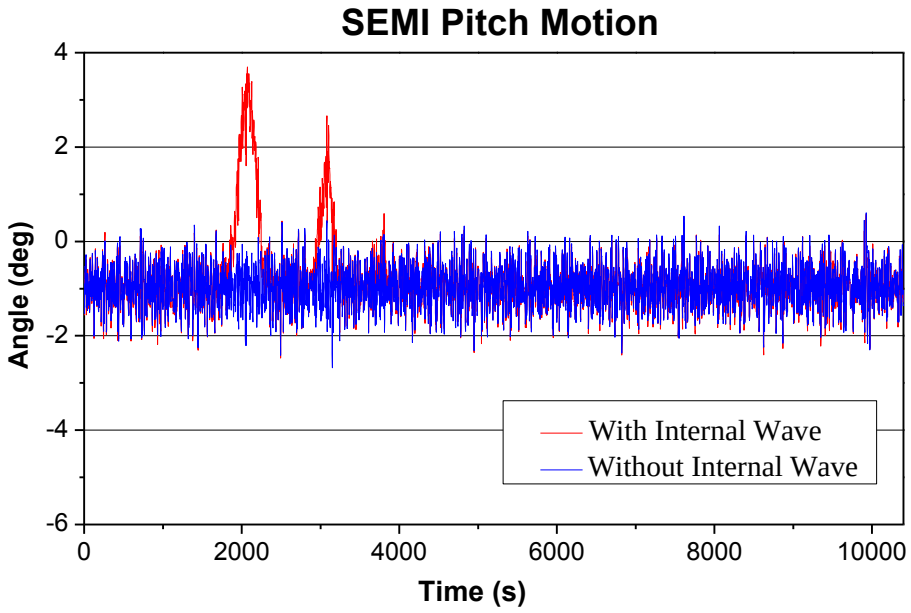

Figure 5.12 Semi Pitch Motion Time History (η=170m)

Table 5.9 Semi Motion Statistics

Condition			Operation			Survival	
						Wave Dominant	Wind Dominant
Internal Wave Height			N/A	90m	170m	N/A	N/A
Offset	MAX	m	0.45	0.39	0.28	-0.81	-0.80
	MIN	m	-7.43	-12.85	-25.16	-33.37	-32.25
	MEAN	m	-3.32	-3.65	-3.80	-18.34	-18.38
Heave	MAX	m	1.14	1.19	1.28	5.80	5.11
	MIN	m	-1.24	-1.19	-1.29	-6.09	-5.39
	MEAN	m	-0.03	-0.02	-0.03	-0.17	-0.18
Pitch	MAX	deg	0.60	2.02	3.72	5.93	5.58
	MIN	deg	-2.68	-2.73	-2.38	-1.32	-1.32
	MEAN	deg	-0.97	-0.88	-0.82	1.88	1.77

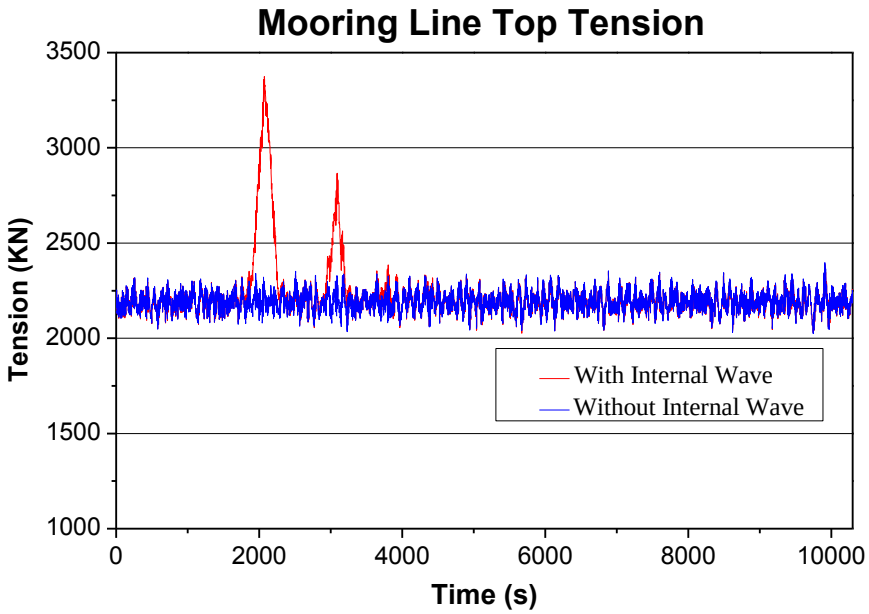

Figure 5.13 Semi Mooring Line #3 Top Tension Time History (η=170m)

Table 5.10 Semi Mooring Line #3 Max Tension and Utilization Ratio

Condition		Operation			Survival	
					Wave Dominant	Wind Dominant
Internal Wave Height		N/A	90m	170m	N/A	N/A
Line Max Tension	KN	2.40E+03	2.65E+03	3.39E+04	4.30E+03	4.18E+03
Utilization Ratio	-	0.17	0.19	0.24	0.30	0.29

5.5. TLP Production System

5.5.1. TLP Description

The production TLP key figures are summarized in Table 5.11 below:

Table 5.11 TLP Key Figures

Draft	m	31.09
Displacement	N	7.05×10^{8}
Total Weight	kg	2.70×10^{7}
Column Height	m	57.91
Column Diameter	m	22.86
Column c/c Span	m	67.06
Pontoon Width	m	11.43
Pontoon Height	m	9.00
Vertical C.G. from Base KG	m	45.11
Vertical C.B. from Base KB	m	12.53
Pitch Radii of Gyration Rxx	m	41.58
Roll Radii of Gyration Ryy	m	41.39
Yaw Radii of Gyration Rzz	m	42.09

The TLP configuration and its tendon properties are shown in Figure 5.14 and Table 5.12 respectively. Figure 5.15 presents the TLP tendon configuration.

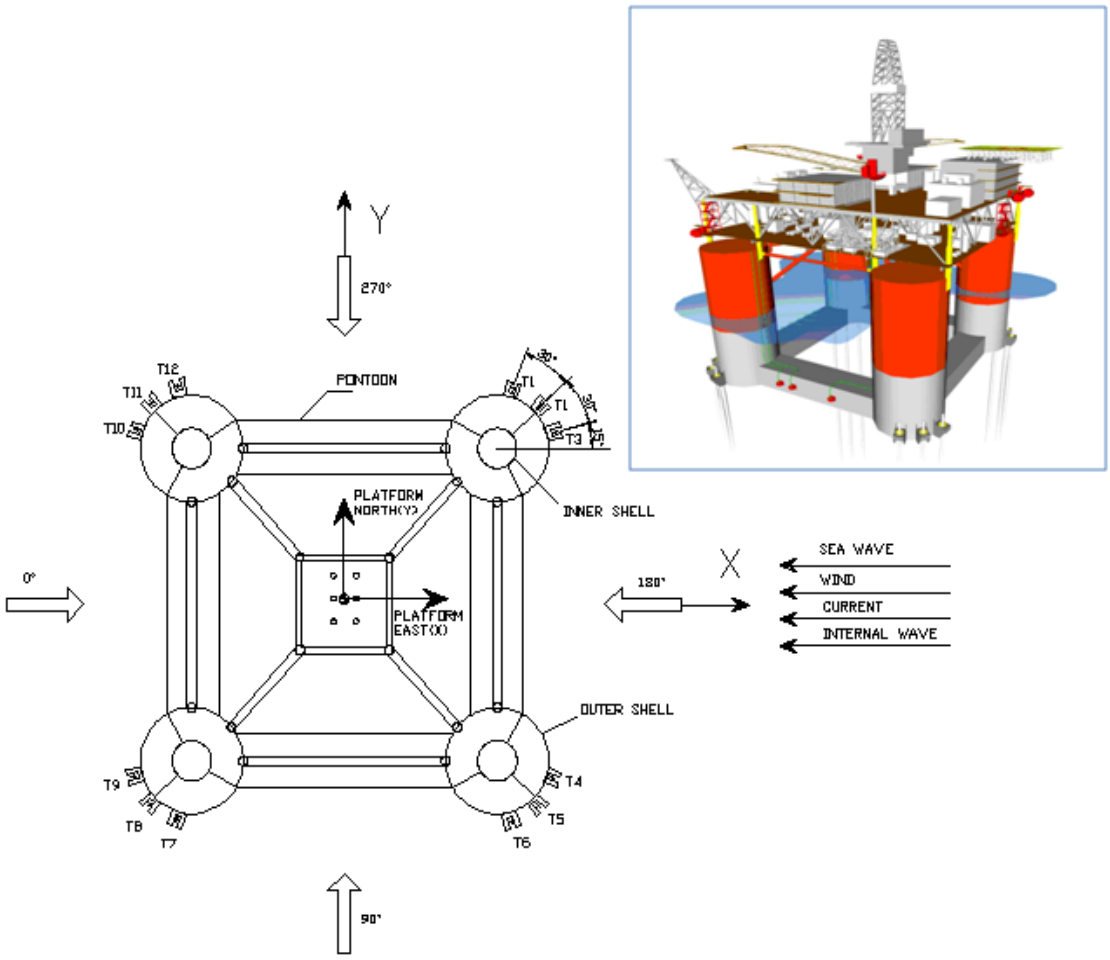

Figure 5.14 TLP Configuration and Mooring Layout

Table 5.12 TLP Tendon Properties

Tendon Properties	Diameter (m)	EA (KN)	EI ($KN \cdot m^{2)}$	Wet Weight (kg/m)	Dry Weight (kg/m)	Length (m)	Material
Segment 1	0.711	2.30×10^7	1.24×10^6	586.01	993.27	6.71	X75
Segment 2	1.07	2.26×10^7	3.02×10^6	61.17	977.51	294.44	X70
Segment 3	1.07	2.28×10^7	3.04×10^6	68.04	984.38	236.52	
Segment 4	0.914	2.10×10^7	2.02×10^6	232.37	905.6	371.86	X70
Segment 5	0.914	2.21×10^7	2.12×10^6	281.33	954.56	274.32	X70

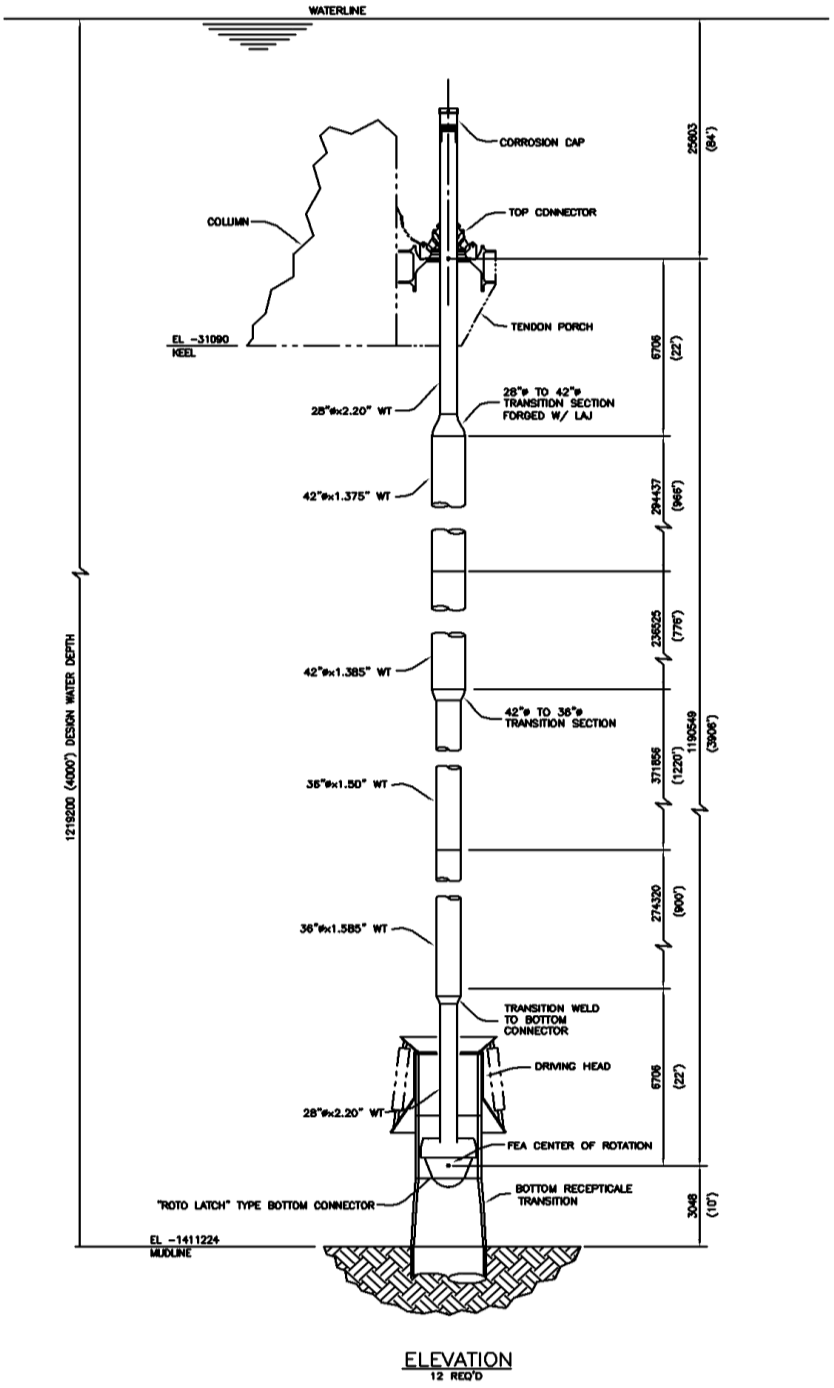

Figure 5.15 TLP Tendon Configuration

The TLP coupled analysis model and the hydrodynamic panel model are presented in Figure 5.16. The analysis model also includes 8 production TTRs, 1 drilling riser, 2 import SCRs, and 2 export SCRs.

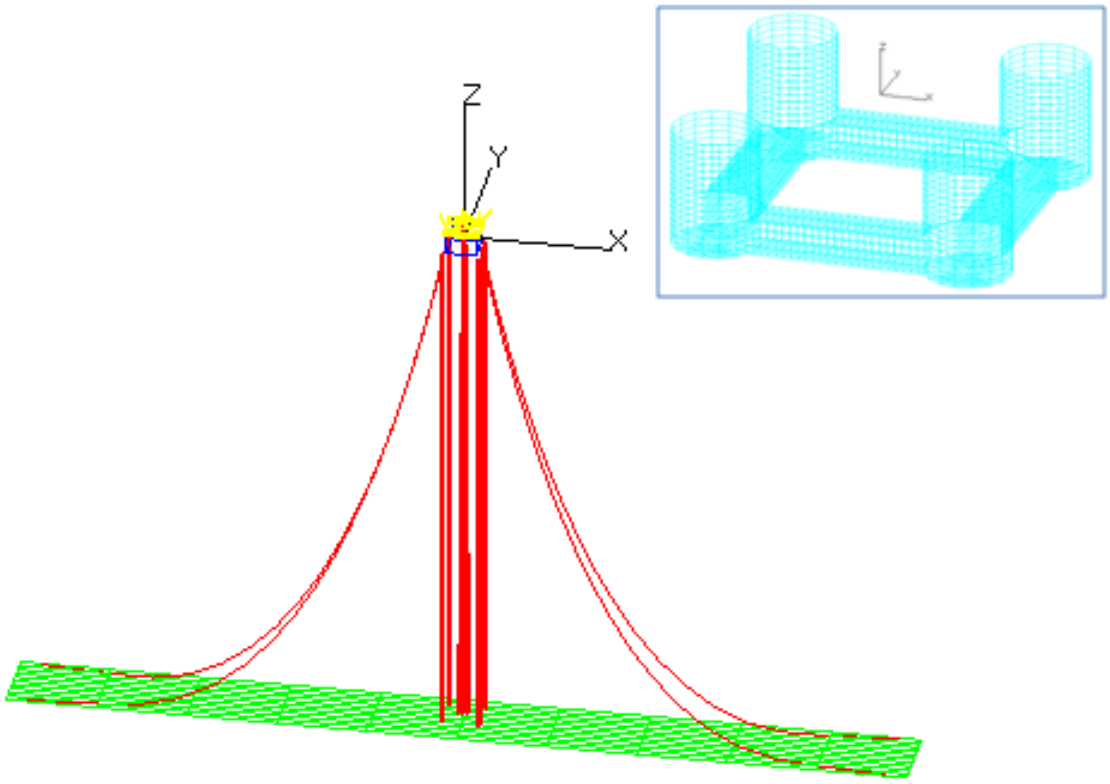

Figure 5.16 TLP Coupled Analysis Model with Program HARP

5.5.2. TLP Analysis and Results

Three-hour time domain dynamic analyses are performed for the same conditions of the Spar and Semi cases. The Semi motions and the top tension time histories of the mooring line (#10) subject to the highest loads for the 170m height internal wave are

shown in Figures 5.17 to 5.20. The motion statistics and the maximum tendon tension with corresponding utilization ratios are summarized in Table 5.13 and 5.14 respectively.

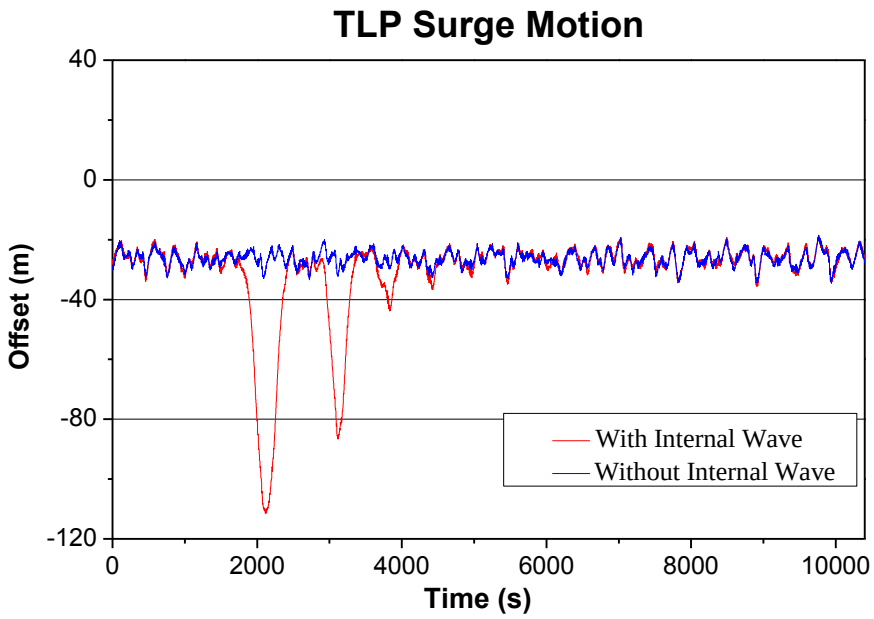

Figure 5.17 TLP Surge Motion Time History (η=170m)

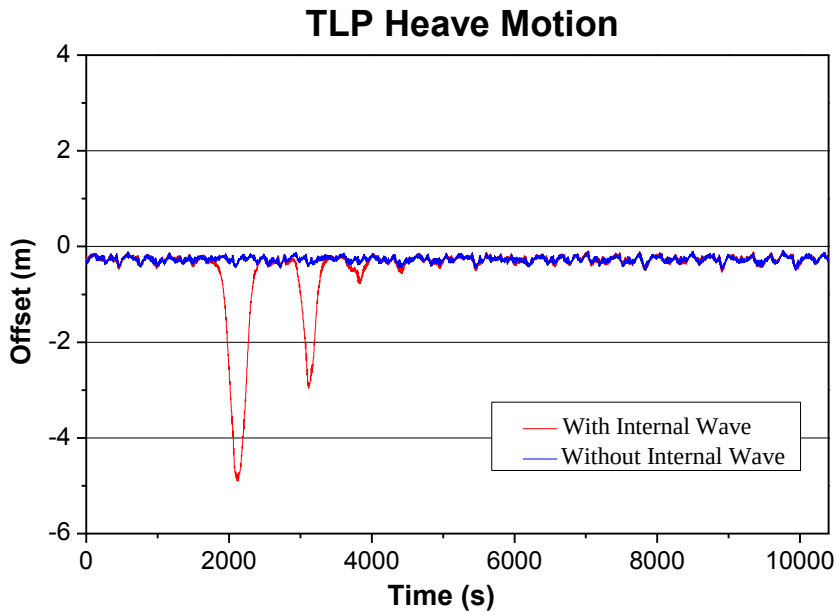

Figure 5.18 TLP Heave Motion Time History (η=170m)

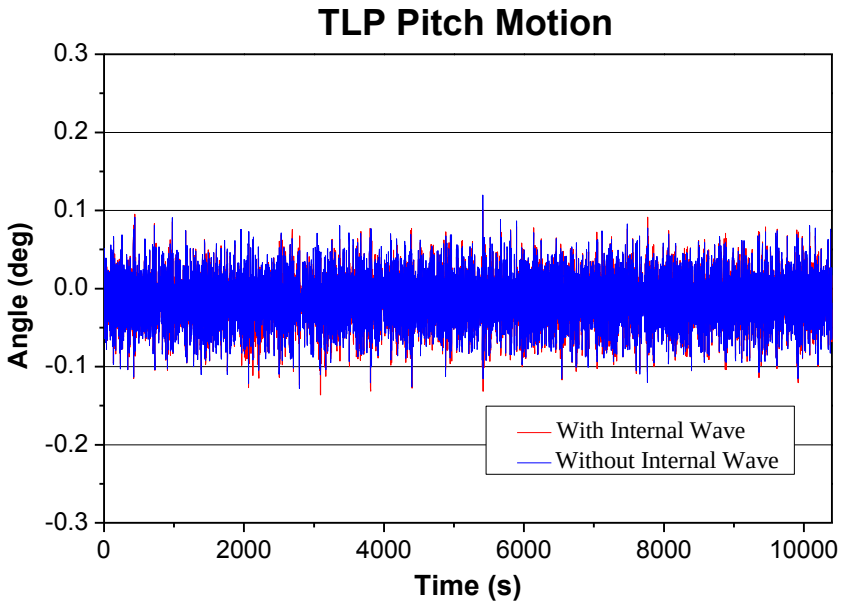

Figure 5.19 TLP Pitch Motion Time History (η=170m)

Table 5.13 TLP Motion Statistics

Condition			Operation			Survival	
						Wave Dominant	Wind Dominant
Internal Wave Height			N/A	90m	170m	N/A	N/A
Offset	MAX	m	-18.60	-18.81	-18.84	-48.04	-52.14
	MIN	m	-34.39	-78.27	-111.44	-82.00	-82.64
	MEAN	m	-26.36	-29.39	-30.31	-63.17	-65.66
Heave	MAX	m	-0.08	-0.09	-0.08	-0.53	0.79
	MIN	m	-0.50	-2.42	-4.90	-2.57	-2.62
	MEAN	m	-0.27	-0.37	-0.44	-1.51	-1.65
Pitch	MAX	deg	0.12	0.12	0.10	0.20	0.19
	MIN	deg	-0.13	-0.13	-0.14	-0.29	-0.28
	MEAN	deg	-0.01	-0.02	-0.02	-0.03	-0.03

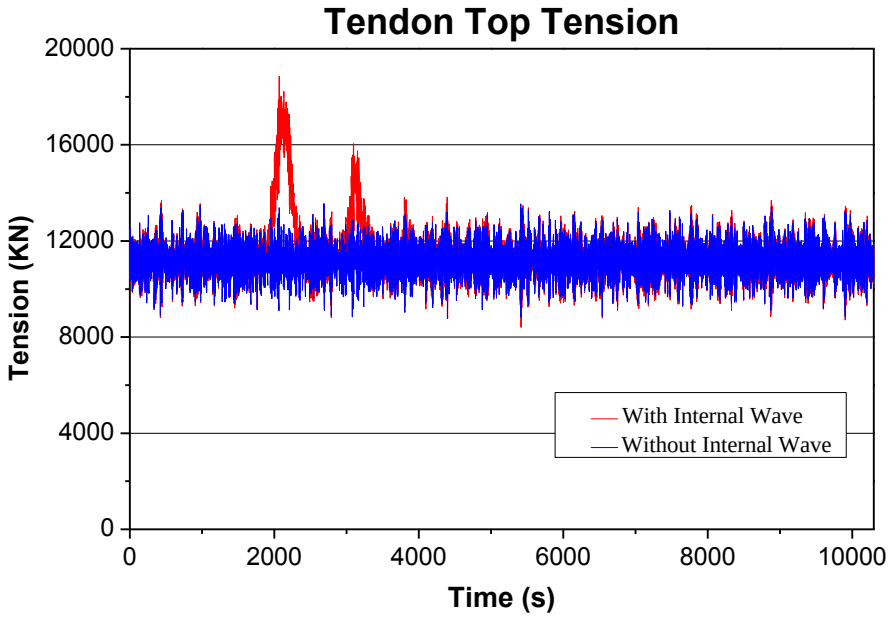

Figure 5.20 TLP Tendon #10 Top Tension Time History (η=170m)

Table 5.14 TLP Tendon #10 Max Tension and Utilization Ratio

Condition		Operation			Survival	
					Wave Dominant	Wind Dominant
Internal Wave Height		N/A	90m	170m	N/A	N/A
Line Max Tension	KN	1.35E+04	1.51E+04	1.89E+04	2.51E+04	2.35E+04
Utilization Ratio	-	0.49	0.55	0.68	0.91	0.85

5.6. Summary

The internal wave model presented in this study and the analysis method could provide relatively realistic representation of internal waves observed in South China Sea for offshore engineering project applications. It is also observed that the internal wave impact on platform motions and mooring/riser strength can be analyzed separately and superimposed to the wind and wave analysis results due to the long period nature of internal waves.

It is seen that internal waves have significant impact on Spar offset, heave, and pitch motions. The Spar offset for the 170m internal wave is larger than its design offset from survival condition, which also results in larger mooring loads and utilization ratios. Our results indicate that the Spar will pitch 2.24 degree and 4.38 degree in the internal wave incident direction for several minutes for the 90m and the 170m internal waves respectively. It is observed that the internal waves mainly impact the Semi offset and pitch motions. However the values are still below the maximum values from the survival case. Therefore, the Semi can be assumed to pass the internal wave design criteria if it is

designed for the 100 year survival condition. It is also seen that the TLP will have larger offset and heave motions under internal wave, even if its tendon is still safer than in the case of design survival condition. It is recommended that Top-tensioned risers on Spar and TLP platforms should be designed with the consideration of the large offset of the platform due to the presence of internal wave. Since Semi is for wet-tree production, TTRs are not present and thus is not affected by the internal wave.

6. APPLICATION III: NONLINEAR INTERNAL WAVES INFLUENCE ON OTEC SYSTEM

6.1. Introduction

Ocean Thermal Energy Conversion (OTEC) systems utilize the temperature difference between the surface water and deep ocean water to generate electrical energy. In addition to ocean surface waves, wind and current, in certain locations like the Andaman Sea, Sulu Sea and the South China Sea the presence of strong internal waves may become a concern in floating OTEC system design. The current paper focuses on studying the dependence of the CWP hydrodynamic drag on relative velocity of the flow around the pipe, the effect of drag amplification due to vortex induced vibrations and the influence of internal waves on the floating semi and the cold water pipe integrated OTEC system. Two CWP sizes are modeled; the 4m diameter pipe represents a small scale prototype and the 10m diameter pipe represents a full commercial size CWP. are considered in the study.

Design of floating ocean thermal energy conversion (OTEC) platforms require a comprehensive analysis of the host platform motions in addition to the stress and strain of the attached cold water pipe (CWP). The offshore structural response of such systems along with the commercial feasibility of such projects has been extensively studied and is available in literature (Barr and Johnson ; Chou et al. ; Claude 1930; Paulling ; Shi et al. 2012; Vega 1992; Vega and Nihous).

The analysis of the OTEC system is usually performed by a coupled analysis approach due to the feedback of the CWP response on the platform. The approach involves analysis of the OTEC platform, mooring lines and the CWP as an integrated structure. Design environmental conditions such as waves, wind and current are then applied and the platform global motions as well as the CWP response are then obtained. However it is observed that even small discrepancies in the modeling could cause significant errors in the response of the system and could result in a faulty design.

The current paper focuses on the influence of the enhanced drag due to the vortex induced vibrations (VIV) of the CWP. The vortex induced vibration occurs due to vortex shedding arising from the current and internal wave applied to the CWP. The study focuses on both a 10 MW small prototype platform with a 4m pipe as well as a 100 MW full size platform with a 10 m diameter pipe.

The study provides a benchmark on the effects of VIV induced drag on the OTEC system and assesses if the phenomenon of internal waves, which commonly occurs in several parts of the globe where OTEC systems are proposed to be installed, has any impact on the design of such systems.

6.2. Description of OTEC System

6.2.1. 100 MW OTEC System

The OTEC platform used in this study is the 100 MW OTEC system shown by Lockheed Martin Corporation at the 2011 Pacific Coast Electrical Association (PCEA) Hawaii Biennial Conference (Varley et al.). A four column semisubmersible with eight

(8) power generation modules attached to the four (4) sides the semi hull is used as the platform. The profile and plan view of the system are presented in Figure 6.1 below.

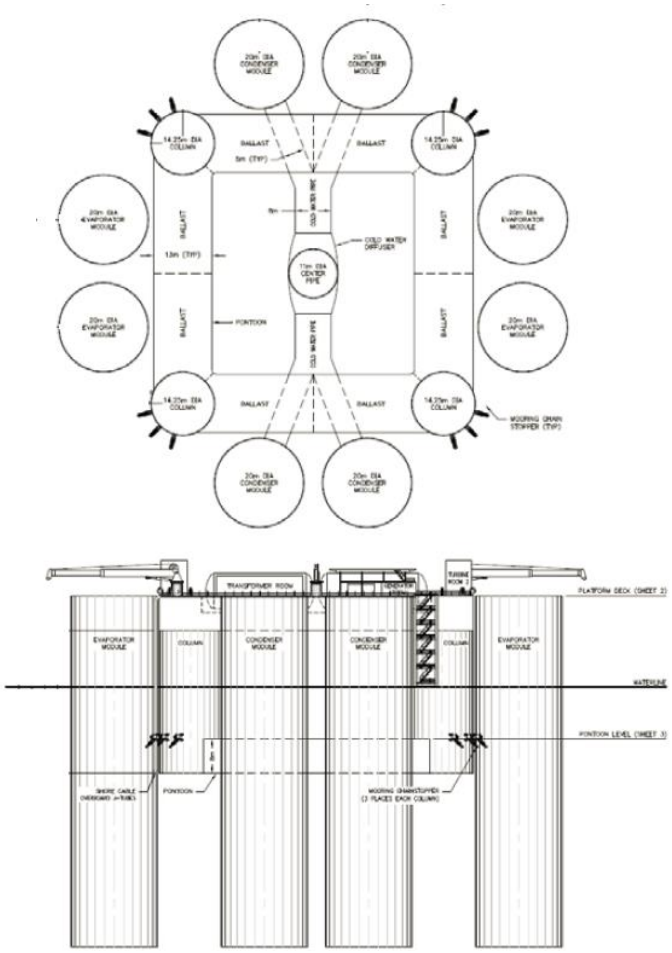

Figure 6.1 100 MW OTEC Platform Elevation View (L) and Plan View (R)

The OTEC platform is assumed to be moored in 1100 m water depth. A twelve line taut CPC (chain-polyester-chain) mooring system is used for station keeping. The polyester line has a diameter of 240 mm and is 2400 m long with a unit wet weight of 10 kg/m. The mooring chain has a diameter of 145 mm with unit wet weight of 380 kg/m.

The key parameters of the platform are summarized in Table 6.1 below:

Table 6.1 Particulars for 100MW Pilot Plant

Particulars	Value
Topsides Weight, t	9,091
Hull Weight, t	5,864
Hull Draft, m	20
Column Spacing, m	56
Column Diameter, m	14.25
No. of Mooring Lines	12
Power Generation Module Draft, m	60
Power Generation Module Dia, m	20
Total Displacement, t	192,381
Displacement Semi Only, t	37,513

The 1000 m long cold water pipe is suspended from the center/keel of the platform. The outer and inner diameter of the CWP is 10.5 m and 10 m respectively. The pipe is a one piece continuous structure and is made of composite material. It is fabricated on site of the platform and is attached to the platform via a gripper system. However it is assumed for the purposes of analysis that the CWP is rigidly connected to the platform via equivalent rotational springs of high spring stiffness.

6.2.2. 10 MW OTEC System

A 10 MW OTEC system representing a small scale prototype is also analyzed in this study for comparison purposes. It is a smaller version of the 100 MW plant with 4 remoras instead of 8.

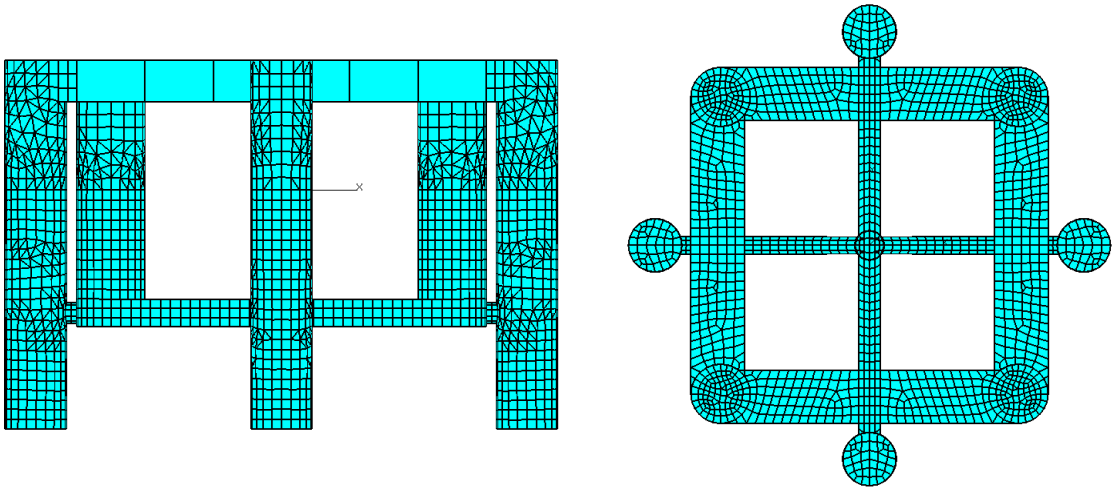

Figure 6.2 10 MW OTEC Platform Elevation View (L) and Plan View (R)

The topside weight and hull weight are about 900 tonnes and 3600 tonnes respectively. The hull draft is 20 m with a column spacing of 50 m and a column diameter of 10 m. The remora draft is reduced to 38 m. In addition the hull is moored in place by 8 mooring lines instead of 12. The profile and plan view of the OTEC system are shown on the left and right side respectively in Figure 6.2 above.

The cold water pipe is made of composite material with a total length of 1000m. It is attached to the 10 MW OTEC platform with an outer diameter of 4.2 m and an inner diameter of 4.0 m.

6.3. Hydrodynamic Drag

The inline force on a cylindrical body in oscillating flow is given by Morisons equation below.

$$F = \frac{\pi}{4}\rho C_m D^2 \dot{u} + \frac{1}{2} C_d \rho D u|u| \qquad (6.1)$$

where ρ is the density, D is the diameter, u is the relative velocity and Cd and Cm are the drag and inertial coefficients respectively. The first term is the inertial term while the second term computes the drag force. The drag coefficient Cd is used to quantify the drag or resistance to the body in fluid. It is found to depend on many parameters such as Reynolds number, Keulegen Carpenter number and surface roughness (White 1991).

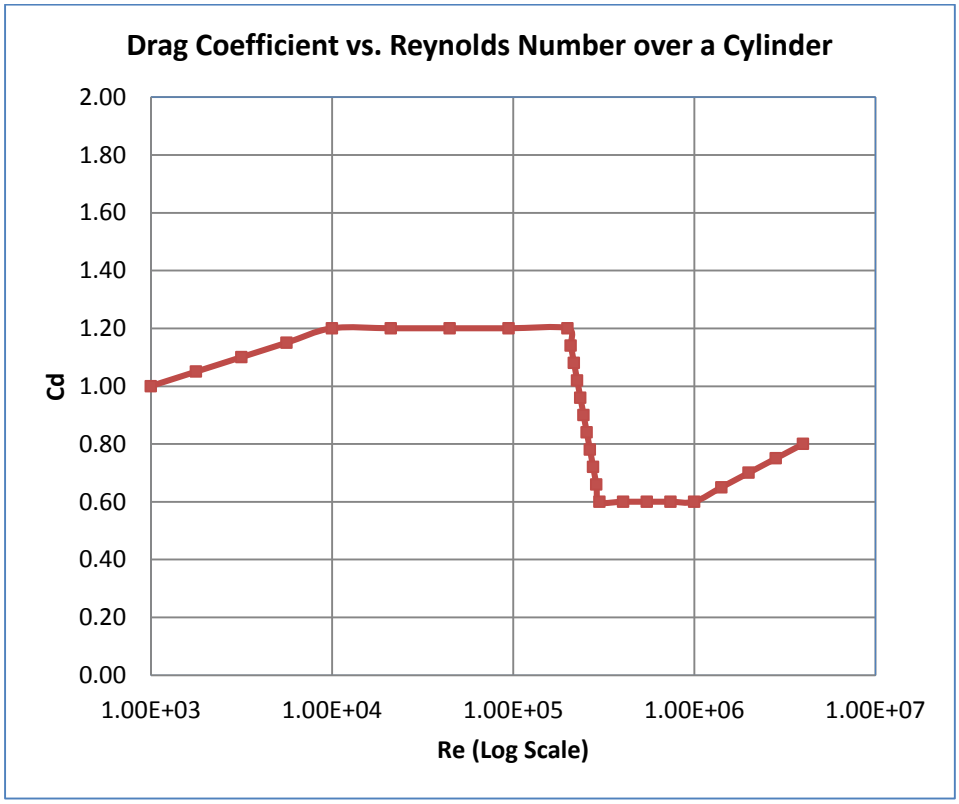

Figure 6.3 Drag Coefficient dependence on Reynolds Number

The current paper focuses on the drag coefficient dependence on Reynolds number. Figure 6.3 above shows the dependence of drag coefficient on the Reynolds number. It is seen that the drag coefficient drops in a certain range of Reynolds number

called the critical flow regime. If the Reynolds number is below the critical flow regime it is called the subcritical flow regime and is characterized by the formation of laminar boundary layer. When the Reynolds number is above the critical regime (supercritical or transcritical flow) the boundary layer is turbulent beyond the separation point.

6.4. Vortex Induced Vibration

It is seen that elastic structures like the CWP develop flow induced oscillations due to energy transfer from the flow around the body near the linear resonance area. This oscillation causes further nonlinearity by modifying the flow pattern around the body. These fluid structure interactions can lead to phenomenon like vortex induced vibrations (VIV), flutter, galloping and buffeting. The current work focuses on the vortex induced vibrations induced by the flow around the cold water pipe. There is a rich and varying source of literature on the effects of VIV on elastic structures and for a comprehensive review the reader is referred to Williamson (2004) and Sarpkaya (2004) and references therein.

The general requirement for VIV to occur in a structure is that the vortex shedding frequency is close to the structural eigen frequency. VIV is normally a self-limiting response as opposed to galloping where large amplitude oscillations might be seen. Vortex induced vibrations are critical to design of offshore structure due to the high fatigue damage caused by the induced stresses. Vortex induced vibration are also found to increases the drag force by amplifying the drag coefficient in Morisons

equation. The following empirical equation (Vandiver 1983) can be used to model the drag coefficient amplification

$$C_{D,Amp} = 1.0 + 1.043\left(2\frac{y_{rms}}{D}\right)^{0.65} \quad (6.2)$$

where yrms is the rms value of structural displacement and D is the diameter.

Computational analysis of VIV involves either solving the full Navier Stokes equations and the corresponding structural response within a CFD framework or using empirical models for evaluating the hydrodynamic forces which is coupled with a structural solver to evaluate the response. While the first method is more comprehensive it is computationally quite expensive and thus the second method is usually favoured for engineering design applications. There are various empirical model based programs available to perform VIV analysis of structures. The current work uses the frequency domain modal superposition program SHEAR7 to study the influence of VIV on the cold water pipe.

SHEAR7 was developed at MIT for predicting the VIV responses of beams in non-uniform flow. The program has been calibrated against data from sub critical flows and has found to be conservative in comparison test with other programs (Vandiver and Li 2005). SHEAR7 was integrated with the coupled analysis program HARP for performing the analysis on OTEC platforms.

SHEAR7 uses modal superposition to evaluate the VIV response for uniform or sheared flows (Vandiver et al. 2005). It performs this by balancing the input power due to lift force and the output power due to damping. The natural frequencies and mode shapes of the CWP are input from a modal program like Flexcom7 modal module. The

potentially excited modes are then determined by comparing the natural frequencies with the maximum and minimum excitation frequencies obtained via the Strouhal relationship. The excitation frequency range is dependent on user defined data for the reduced velocity bandwidth. The modes above a user defined cut-off (principally excited modes) are then found based on which the excitation length of the cold water pipe is determined. The excitation length is the length of the cold water pipe which is excited due to the power input from the surrounding fluid to the structure. If several modes are found to participate in the excitation and there are overlaps within the excitation regions, mode overlap elimination is performed. The initial lift and drag coefficients are then computed. The modal input power due to the lift force and the modal output power due to damping are then determined. The A/D (Amplitude /Diameter) ratio is computed based on the modal force and modal damping. Conservation of energy requires the input power to be equal to the output power. An iterative calculation is performed where the lift coefficient and damping coefficients are updated until the A/D ratio converges. The RMS response of the pipe is then determined from which the drag coefficient amplification can be ascertained from Equation 6.2.

SHEAR7 version 4.4 is used for the computation. The user defined single and multi- mode reduced velocity bandwidth is 0.4 and 0.2 respectively. The cut-off level that determines the number of modal power in regions was set to 0.7 which is considered to be conservative.

6.5. Environmental Parameters

Design operative conditions and internal waves observed in South China Sea are the basis of the environment conditions used in this study. A generic South China Sea field with an assumed water depth of 1100 m is selected for this study. The pycnocline is assumed to be at 200 m below the ocean surface.

6.5.1. Surface Wind, Wave and Current

The maximum operative design environmental conditions listed in Table 6.2 below are applied in the analysis. These correspond to a 1 year return period criteria.

Table 6.2 Metocean Data for Analysis

Items	Units	South China Sea Water Depth = 1100m	
		1 Year Return Period Criteria Operating Condition	
Wave		Jonswap	
Gamma		1	
Wave Direction	deg	180	
Significant Wave Height (Hs)	m	6	
Spectral Peak Period (T_p)	s	11.2	
Wind		API	
1 Hour Average Wind	m/s	21.97	
Wind Direction	deg	180	
		-200	0.17
		-300	0.14
		-500	0.13
		-700	0.13
		-1100	0.13
Current Direction	deg	150	

6.6. Coupled Analysis and Modeling

The global performance analysis of the OTEC floating platform was performed with the coupled analysis program HARP to take into account the contribution of CWP to hull motions.

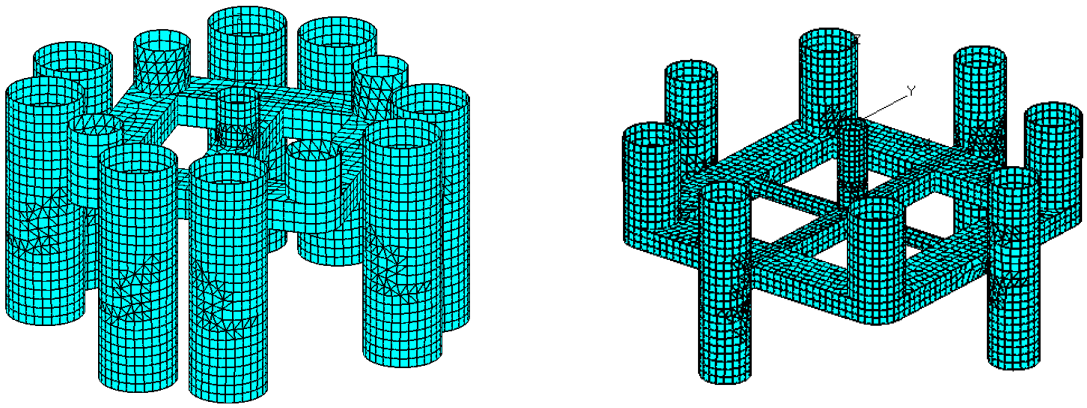

Figure 6.4 100 MW (L) and 10 MW (R) OTEC Hydrodynamic Analysis Panel Models

The hydrodynamic panel model used by the wave diffraction and radiation program WAMIT for both the 100 MW and 10 MW OTEC platforms are presented in 6.4 above.

3D nonlinear beam elements are used to model the mooring lines and the CWP pipe. The platform hull is an integral part of the finite element system of solutions. The program performs dynamic finite element analysis to evaluate the offshore floating platform motions and the response of the cold water pipe. For the purposes of this study, the program was modified by integrating SHEAR7 into the code to account for the contribution of the enhanced drag amplification from the VIV in global analysis.

6.7. Analysis and Results

Three- hour time domain simulations are performed for both the 100 MW and 10 MW OTEC platforms. Table 6.3 below enumerates the cases analyzed.

Table 6.3 Load Case Matrix

OTEC Platform	Case #	Internal Wave	CWP Cd	VIV Enhanced Drag
100 MW	1	N/A	Cd = 1	N/A
	2	Wave height= 90 m, Direction = 180 degrees	Cd = 1	N/A
	3	Wave height= 90 m, Direction = 180 degrees	Cd = f(Re)	N/A
	4	Wave height= 90 m, Direction = 180 degrees	Cd = f(Re)	Applied
	5	N/A	Cd = f(Re)	N/A
	6	Wave height= 90 m, Direction = 0 degrees	Cd = f(Re)	Applied
	7	N/A	Cd = f(Re)	Applied
10 MW	8	N/A	Cd = 1	N/A
	9	Wave height= 90 m, Direction = 180 degrees	Cd = 1	N/A
	10	Wave height= 90 m, Direction = 180 degrees	Cd = f(Re)	N/A
	11	Wave height= 90 m, Direction = 180 degrees	Cd = f(Re)	Applied
	12	N/A	Cd = f(Re)	N/A
	13	Wave height= 90 m, Direction = 0 degrees	Cd = f(Re)	Applied
	14	N/A	Cd = f(Re)	Applied

A total of fourteen cases are analyzed for the 100 MW full scale platform (Cases 1-7) and the 10 MW prototypes (Cases 8-14). The variance of drag coefficient, influence of VIV enhanced drag and the influence of internal wave along with the direction are studied based on the results from these 12 cases.

Cases 1 and 8 represent the base cases with drag coefficient Cd = 1 applied. VIV and Internal waves are not applied in those cases. The influence of the internal wave in the current direction is investigated in Cases 2 and 9. In cases 3 and 10 the influence due to dependence of drag coefficient on Reynolds number is analyzed. Cases 4 and 11 have

the VIV enhanced drag additionally applied to the cold water pipes. Cases 5 and 12 are analyzed to compare the influence of Reynolds number dependent drag with the base cases. The influence of internal wave phenomenon and direction relative to applied current are analyzed by comparing cases 7 and 6 with case 4 for the 100 MW OTEC Platform. The corresponding cases for the 10 MW platform are 14 and 13 respectively.

The results of the analysis are presented in Figures 6.5 to 6.10 below. The OTEC translational vessel motion statistics for all the cases are shown in Table 6.4 while the influence of the internal wave and direction on platform surge motion is examined in Figures 6.9 and 6.10.

Figure 6.7 and Figure 6.8 present the CWP bending moment envelope for the 100 MW and 10 MW cases respectively for all seven cases. The plot shown in the upper section of each figure is split into 3 separate zoomed plots in the lower section to enable easier comprehension of the data. The lower left plot shows the influence of the internal wave and direction with the drag enhanced VIV applied to the CWP. The lower center plot examines the influence of Reynolds number on the drag coefficient and drag enhancement due to VIV in the absence of internal waves while the lower right plot presents the same data in the presence of internal waves. The influence of internal waves on the Reynolds number dependent drag coefficient is presented in Figure 6.9 for both the 10 MW and 100 MW OTEC platforms. Figure 6.10 examines the effect of internal waves on the VIV enhanced drag coefficient for both the 10 m and 4 m diameter CWP.

Table 6.4 OTEC Vessel Motion Statistics

OTEC Vessel Motions									
	Surge (m)			Heave (m)			Pitch (deg)		
100MW	MAX	MIN	MEAN	MAX	MIN	MEAN	MAX	MIN	MEAN
Case 1	0.04	-16.30	-9.92	1.43	-1.21	0.02	1.67	-1.46	0.08
Case 2	0.04	-50.17	-12.34	1.43	-1.20	0.01	1.67	-1.46	0.11
Case 3	0.04	-49.02	-11.92	1.43	-1.21	0.01	1.75	-1.55	0.07
Case 4	0.04	-50.34	-12.49	1.43	-1.20	0.01	1.64	-1.42	0.12
Case 5	0.04	-16.17	-9.57	1.43	-1.20	0.02	1.75	-1.55	0.05
Case 6	13.06	-15.86	-8.77	1.43	-1.20	0.02	1.65	-1.42	0.09
Case 7	0.04	-16.37	-10.11	1.43	-1.21	0.02	1.65	-1.42	0.10
10 MW									
Case 8	0.02	-15.66	-9.41	1.51	-1.43	-0.01	1.80	-1.62	0.21
Case 9	0.02	-42.36	-11.42	1.52	-1.44	-0.02	2.84	-1.61	0.30
Case 10	0.02	-40.83	-10.93	1.52	-1.43	-0.02	-2.70	-1.79	0.21
Case 11	0.02	-43.01	-11.47	1.52	-1.45	-0.02	3.10	-1.66	0.31
Case 12	0.02	-15.38	-8.99	1.52	-1.43	-0.01	1.90	-1.79	0.14
Case 13	8.32	-15.18	-8.39	1.53	-1.43	-0.01	1.80	-1.62	0.19
Case 14	0.02	-15.67	-9.43	1.51	-1.43	-0.01	1.80	-1.62	0.22

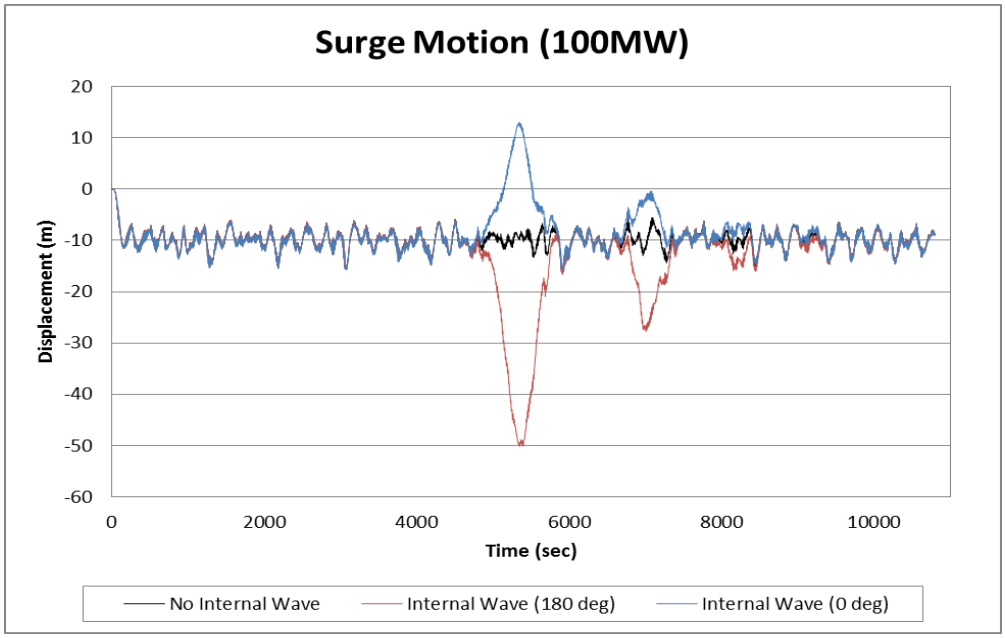

Figure 6.5 Influence of Internal Wave and Direction w.r.t Current on Surge Motion for the 100MW OTEC Platform

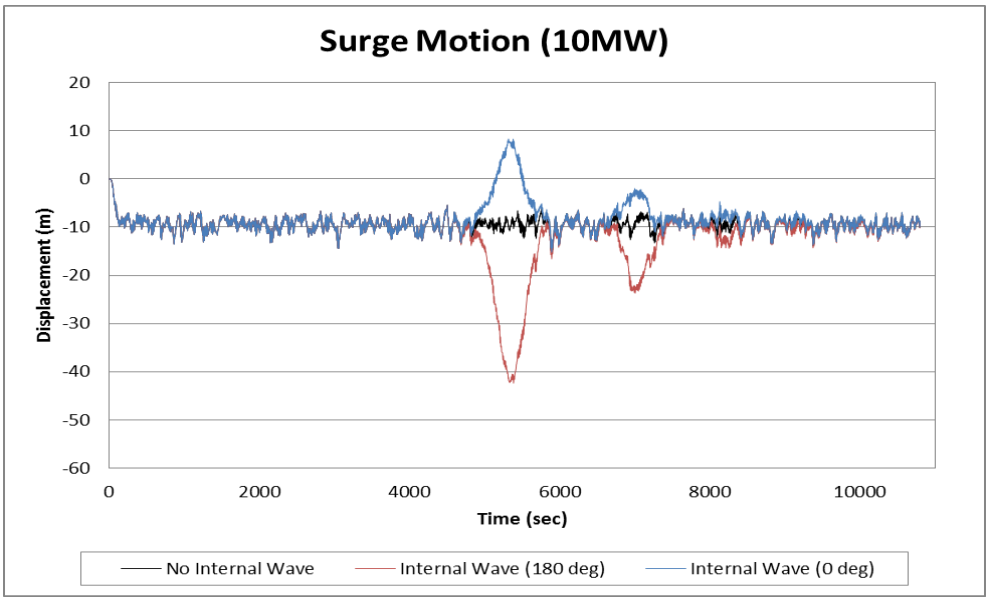

Figure 6.6 Influence of Internal Wave and Direction w.r.t Current on Surge Motion for the 10 MW OTEC Platforms

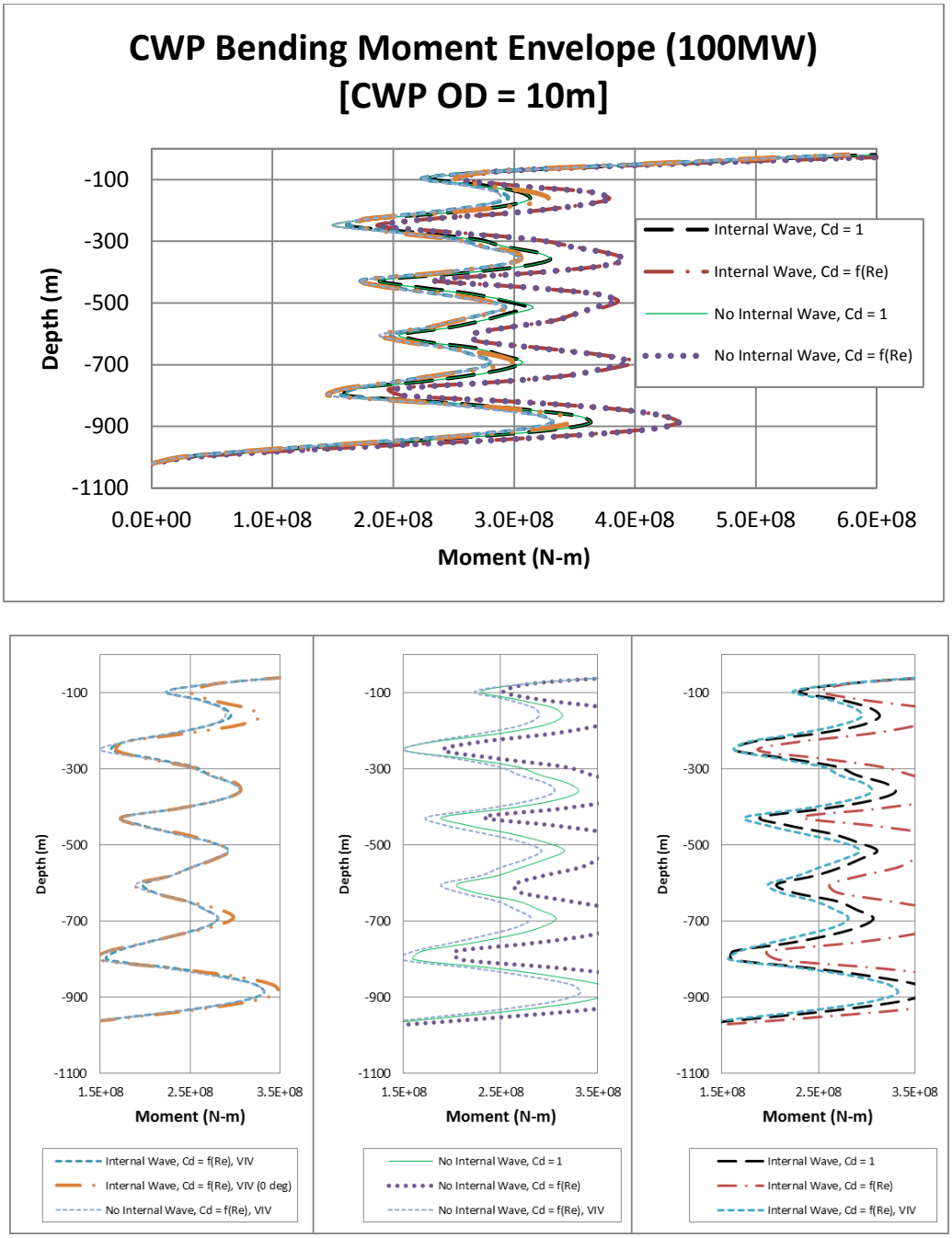

Figure 6.7 CWP Bending Moment Envelope for the 100 MW OTEC Platform

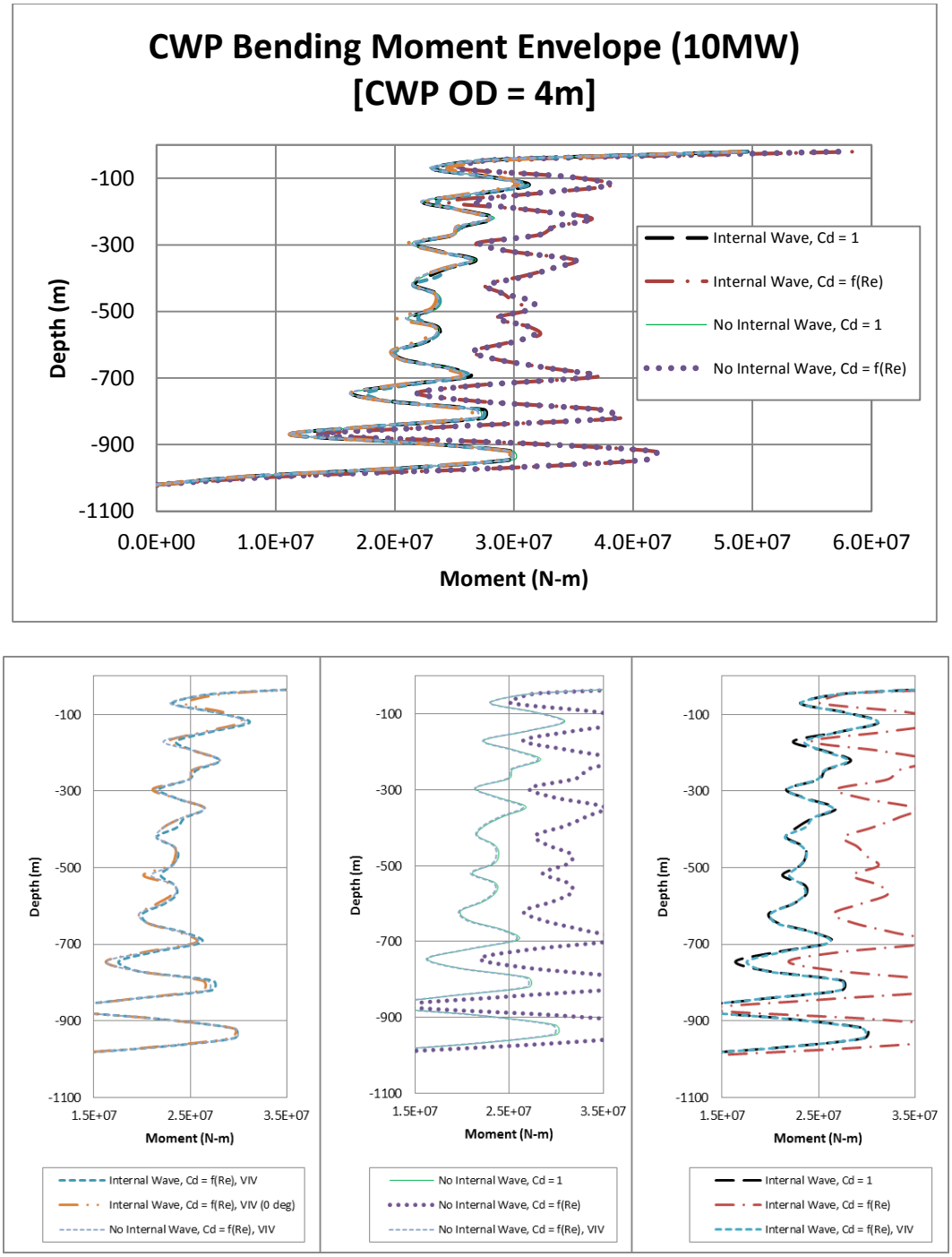

Figure 6.8 CWP Bending Moment Envelope for the 10 MW OTEC Platform

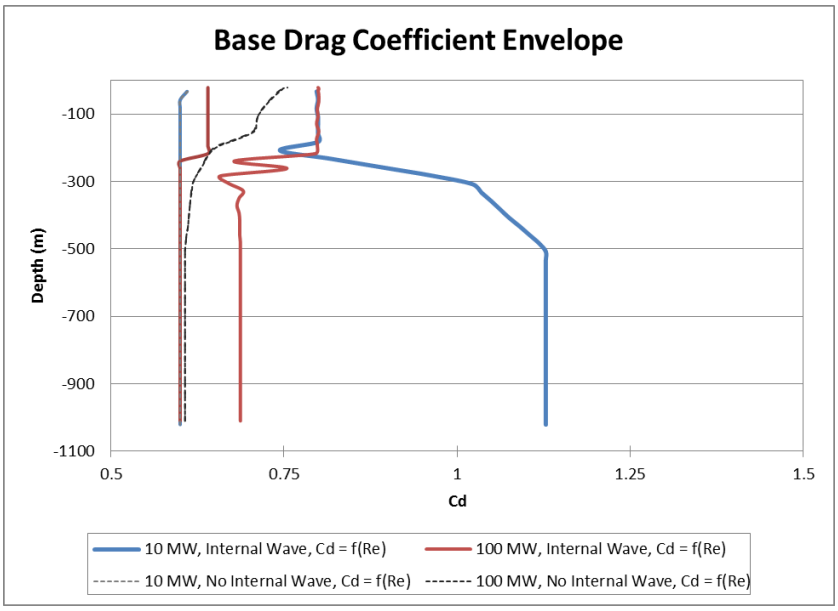

Figure 6.9 Comparison of Internal Wave Influence on Base Drag Coefficient Envelope for the 10 MW and 100 MW Platforms

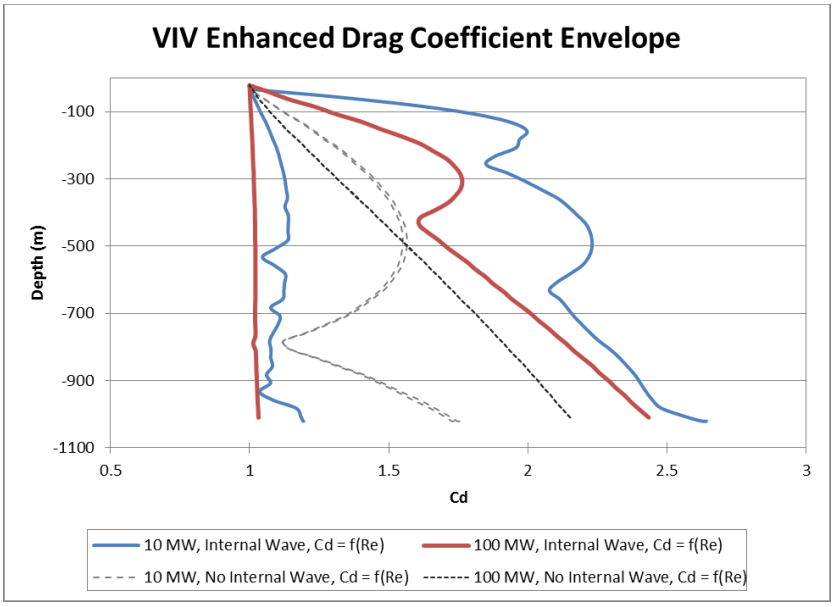

Figure 6.10 Comparison of Internal Wave Influence on VIV Enhanced Drag Coefficient Envelope for the 10 MW and 100 MW Platforms

6.8. Summary

Based on the analysis results shown in the previous section, the following conclusions and findings are drawn:

Modeling the CWP with the combination of the base Re number dependent drag coefficient and the VIV enhanced drag coefficient is a reasonable and effective approach to obtain the hydrodynamic drag coefficient of a larger diameter pipe in dynamic analysis.

Internal wave has significant impact of OTEC platform motions and mooring line load, but there is a minimum influence on CWP dynamic bending moment for design consideration. This is because the CWP is free hanging and the internal wave period is much longer than the platform surge period due to surface wave.

The larger 10 m diameter CWP will have relatively small VIV behavior than the 4 m CWP. CWP VIV under current and internal wave loads will add hydrodynamic damping and eventually could reduce the maximum CWP bending moment. But, VIV induced fatigue need to be considered for both CWP sizes.

Adding strakes can be a good option for CWP to increase hydrodynamic damping and reduce VIV induced fatigue damage.

For the current and internal wave applied in this study, using a combined drag coefficient of Cd equal to 1 could provide an reasonable estimation of hydrodynamic drag for the analysis.

Further validation of the results should include verification of the base drag coefficients as a function of Reynolds number for large diameter pipes. Model test data

for large CWP pipes are necessary for the update. It is also useful if CFD analysis is available for the purpose of verification.

In conclusion the results obtained from this study provide valuable information for the design and analysis of future OTEC systems. The methodology of using coupled analysis with deepwater internal wave model plus the base Re number dependent drag coefficient and the VIV enhanced drag coefficient calculated by SHEAR7 program is a valid and effective approach for design and evaluation internal wave influence on OTEC systems.

7. CONCLUSIONS

The internal wave model presented in this study could provide relatively realistic representation of shallow internal waves observed in South China Sea. The analysis method is feasible for modeling internal wave in offshore engineering project applications. The methodology can be extended to finite depth and deep water formulations with varying pycnocline (Barr and Johnson ; Chou et al. ; Paulling ; Paulling 1980; Sarpkaya 2004) for a more accurate assessment of the effects of internal waves on offshore platforms and a future paper will address these concerns.

Analysis results are similar to offshore observations. The internal wave impact on platform motions and mooring/riser strength can be analyzed separately and superimposed to the wind wave analysis results. This is clearly due to the long period nature of internal waves.

It is seen that internal waves have a considerable impact on deep water drilling risers where overstress or even failure may result at the bottom connection to BOP due to the large bending caused by the platform offset.

It is recommended that the drilling riser mooring system designed for survival environmental conditions should have compatible strength for internal waves.

The internal wave model presented in this study and the analysis method could provide relatively realistic representation of internal waves observed in South China Sea for offshore engineering project applications. It is also observed that the internal wave impact on platform motions and mooring/riser strength can be analyzed separately and

superimposed to the wind and wave analysis results due to the long period nature of internal waves.

It is seen that internal waves have significant impact on Spar offset, heave, and pitch motions. The Spar offset for the 170m internal wave is larger than its design offset from survival condition, which also results in larger mooring loads and utilization ratios. Our results indicate that the Spar will pitch 2.24 degree and 4.38 degree in the internal wave incident direction for several minutes for the 90m and the 170m internal waves respectively. It is observed that the internal waves mainly impact the Semi offset and pitch motions. However the values are still below the maximum values from the survival case. Therefore, the Semi can be assumed to pass the internal wave design criteria if it is designed for the 100 year survival condition. It is also seen that the TLP will have larger offset and heave motions under internal wave, even if its tendon is still safer than in the case of design survival condition. It is recommended that Top-tensioned risers on Spar and TLP platforms should be designed with the consideration of the large offset of the platform due to the presence of internal wave. Since Semi is for wet-tree production, TTRs are not present and thus is not affected by the internal wave.

Modeling the CWP with the combination of the base Re number dependent drag coefficient and the VIV enhanced drag coefficient is a reasonable and effective approach to obtain the hydrodynamic drag coefficient of a larger diameter pipe in dynamic analysis.

Internal wave has significant impact of OTEC platform motions and mooring line load, but there is a minimum influence on CWP dynamic bending moment for design

consideration. This is because the CWP is free hanging and the internal wave period is much longer than the platform surge period due to surface wave.

The larger 10 m diameter CWP will have relatively small VIV behavior than the 4 m CWP. CWP VIV under current and internal wave loads will add hydrodynamic damping and eventually could reduce the maximum CWP bending moment. But, VIV induced fatigue need to be considered for both CWP sizes.

Adding strakes can be a good option for CWP to increase hydrodynamic damping and reduce VIV induced fatigue damage.

For the current and internal wave applied in this study, using a combined drag coefficient of Cd equal to 1 could provide an reasonable estimation of hydrodynamic drag for the analysis.

Further validation of the results should include verification of the base drag coefficients as a function of Reynolds number for large diameter pipes. Model test data for large CWP pipes are necessary for the update. It is also useful if CFD analysis is available for the purpose of verification.

In conclusion the results obtained from this study provide valuable information for the design and analysis of future OTEC systems. The methodology of using coupled analysis with deepwater internal wave model plus the base Re number dependent drag coefficient and the VIV enhanced drag coefficient calculated by SHEAR7 program is a valid and effective approach for design and evaluation internal wave influence on OTEC systems.

REFERENCES

Ablowitz, M. J., and Segur, J. (1981). *Solitons and the Inverse Scattering Transform*, SIAM, Philadelphia, PA.

Apel, J. R. (2003). "A new analytical model for internal solitons in oceans." *J. Phys. Oceanography*, 33, 2247-2269.

Apel, J. R., and Gonzalez, F. I. (1983). "Nonlinear features of internal waves off Baja Californiaas observed from the SEASAT Imaging Radar." *J. Geophys. Res.*, 88, 4459-4466.

Armi, l., and Farmer, D. M. (1988). "The flow of Mediterranean water through the Strait of Gibralter." *Progress in Oceanography*, 21, 1-105.

Bains, P. G. (1995). *Topographic Effects in Stratified Flows*, Cambridge Univ. Press, New York, NY.

Barr, R. A., and Johnson, V. E. "Evaluation of analytical and experimental methods for determining OTEC plant dynamics and CWP loads." Paper presented at the 6th Ocean Thermal Energy Conversion Conference, Washington, DC, June 19-22, 1979.

Chou, D. Y., Minner, W. F., Ragusa, L., and Ho, R. T. "Dynamic Analysis of Coupled OTEC Platform Cold Water Pipe System." Paper presented at the Offshore Technology Conference Houston, TX, May 8-11, 1978.

Claude, G. (1930). "Power from the Tropical Seas." *Mechanical Engineering*, 52(12), 1039-1044.

Duda, T., and Farmer, D. E. (1999). "The WHOI/IOS/ONR Internal Solitary Wave Workshop: Contributed Papers."

Farmer, D. M., and Armi, L. (1999). "The generation and trapping of solitary waves over topography." *Science*, 283, 188-190.

Goff, M., Jeans, G., Harrington-Missin, L., and Baschenis, C. "Soliton Early Warning System for Offshore Applications." Paper presented at the Oceanology International Conference 2010 London, UK, March 9-11, 2010.

Gurevich, A. V., and Pitaevskii, L. P. (1973). "Decay of initial discontinuity in the Korteweg- De Vries equation.".*JETP Lett.* V, 17(193-195).

Gurevich, A. V., and Pitaevskii, L. P. (1973). "Nonstationary structure of a collisionless shockwave." *Sov. Phys. JETP*, 38, 291-297.

Halpern, D. (1971). "Semidiurnal tides in Massachusetts Bay." *J. Geophys. Res.*, 76, 6573-6584.

Hibiya, T. (1988). "The generation of internal waves by tidal flow over Stellwagen bank." *J. Geophys. Res.*, 93, 533-542.

Ko, D. S., Martin, P. J., Chao, S. Y., Shaw, P. T., and Lien, R. C. (2008). "Large Amplitude Internal Waves in the South China Sea." *Ocean Science and Technology, 2008 NRL Review*, 197-200.

Korteweg, D. J., and de Vries, G. (1895). "On the change of form of long waves advancing in a rectangular canal, and on a new type of long stationary wave." *Philosophical Magazine*, 39, 422-443.

Liu, A. K., and Benny, D. J. (1981). "The evolution of nonlinear wave trains in stratified shear flows." *Stud. Appl. Math.*, 64, 247-269.

Newsome, R., and Banta, R. (2003). "Shear flow instability in the stable nocturnal boundary layer as observed by Doppler lidar during CASES-99." *J. Atmos. Sci*., 60, 16-33.

Osborne, A. R. (1995). "Solitons in the periodic Korteweg-de Vries equation, the θ-function representation, and the analysis of nonlinear stochastic wave trains." *Phys. Rev. E*, 52, 1105-1122.

Osbourne, A. R., Brown, J. R., Burch, T. L., and Scarlet, R. I. "The Influence of Internal Waves on Deepwater Drilling Operations." Paper presented at the Offshore Technology Conference, Houston, TX, May 2-5, 1977.

Ostrovsky, L. A., and Stepanyants, Y. A. (1989). "Do internal solitons exist in the ocean?" *Rev. Geophys.*, 27, 293-310.

Paulling, J. R. "Frequency Domain Analysis of OTEC CW Pipe and Platform Dynamics." Paper presented at the Offshore Technology Conference, Houston, TX; , Apr.30 - May 7, 1979.

Paulling, J. R. "An equivalent linear representation of the forces exerted on the OTEC CW pipe by combined effects of waves and current." Proc., Energy-Sources Technology Conference and Exhibition, Ocean Engineering for OTEC, 21-28.

Sarpkaya, T. (2004). "A critical review of the intrinsic nature of vortex-induced vibrations." *J. Fluids and Struc*, 19, 389-447.

Shi, S., Halkyard, J., Kurup, N., and Jiang, L. "Coupled Analysis Approach in OTEC System Design." Proc., ASME 2012 31st International Conference on Ocean, Offshore and Arctic Engineering.

Vandiver, J., and Li, L. 2005. *SHEAR7 Program Theory Manual MIT*, Boston, MA.

Vandiver, J., Li, L., Leverette, S., and Marcollo, H. (2005). "User Guide for SHEAR7 Version 4.4 Manual." MIT, Boston, MA.

Vandiver, J. K. "Drag coefficients of long-flexible cylinders." Paper presented at the Offshore Technology Conference, Houston, TX, May 2-5, 1983.

Varley, R., Meyer, L., and Cooper, D. "Ocean Thermal Energy Conversion (OTEC)." Paper presented at the Pacific Coast Electrical Association (PCEA)Hawaii Biennial Conference, Presentation, Aug. 31-Sep. 2, 2011.

Vega, L. A. (1992). "Economics of Ocean Thermal Energy Conversion (OTEC)." *Ocean Energy Recovery: The State of the Art, R. J. Seymour, ed*., American Society of Civil Engineers, New York, NY.

Vega, L. A., and Nihous, G. C. "At-Sea Test of the Structural Response of a Large Diameter Pipe Attached to a Surface Vessel." Paper presented at the Offshore Technology Conference, Houston, May 1988.

White, F. M. (1991). *Viscous Fluid Flow*, McGraw-Hill Inc, New York.

Williamson, C. H. K., and Govardhan, R. (2004). "Vortex-Induced Vibrations." *Annu. Rev. Fluid Mech*, 36, 413-455.